Neural Activity Mapping Using Electromagnetic Fields: An *In Vivo* Preliminary Functional Magnetic Resonance Electrical Impedance Tomography (fMREIT) Study

by

Neeta Ashok Kumar

A Dissertation Presented in Partial Fulfillment
of the Requirements for the Degree
Doctor of Philosophy

Approved July 2020 by the
Graduate Supervisory Committee:

Rosalind J. Sadleir, Chair
Bradley Greger
Jitendran Muthuswamy
Stephen Helms Tillery
SungMin Sohn

ARIZONA STATE UNIVERSITY

August 2020

ABSTRACT

Electromagnetic fields (EMFs) generated by biologically active neural tissue are critical in the diagnosis and treatment of neurological diseases. Biological EMFs are characterized by electromagnetic properties such as electrical conductivity, permittivity and magnetic susceptibility. The electrical conductivity of active tissue has been shown to serve as a biomarker for the direct detection of neural activity, and the diagnosis, staging and prognosis of disease states such as cancer. Magnetic resonance electrical impedance tomography (MREIT) was developed to map the cross-sectional conductivity distribution of electrically conductive objects using externally applied electrical currents. Simulation and *in vitro* studies of invertebrate neural tissue complexes demonstrated the correlation of membrane conductivity variations with neural activation levels using the MREIT technique, therefore laying the foundation for functional MREIT (fMREIT) to detect neural activity, and future *in vivo* fMREIT studies.

The development of fMREIT for the direct detection of neural activity using conductivity contrast in *in vivo* settings has been the focus of the research work presented here. An *in vivo* animal model was developed to detect neural activity initiated changes in neuronal membrane conductivities under external electrical current stimulation. Neural activity was induced in somatosensory areas I (SAI) and II (SAII) by applying electrical currents between the second and fourth digits of the rodent forepaw. The *in vivo* animal model involved the use of forepaw stimulation to evoke somatosensory neural activations along with hippocampal fMREIT imaging currents contemporaneously applied under magnetic

field strengths of 7 Tesla. Three distinct types of fMREIT current waveforms were applied as imaging currents under two inhalants – air and carbogen. Active regions in the somatosensory cortex showed significant apparent conductivity changes as variations in fMREIT phase (φ_d and $\nabla^2\varphi_d$) signals represented by fMREIT activation maps (F-tests, p <0.05). Consistent changes in the standard deviation of φ_d and $\nabla^2\varphi_d$ in cortical voxels contralateral to forepaw stimulation were observed across imaging sessions. These preliminary findings show that fMREIT may have the potential to detect conductivity changes correlated with neural activity.

DEDICATION

To my mother – *Sangeetha Ashok Kumar*

and

To the memory of my father – *V.P. Ashok Kumar*

ACKNOWLEDGEMENTS

The success of the interdisciplinary research presented here is a direct outcome of collaborative initiatives across distinct research entities – Neuro-electricity Lab (Arizona State University), DACT Veterinary team (Arizona State University) and BNI-ASU Center for Preclinical Imaging (Barrow Neurological Institute). The Neuro-electricity Lab spearheaded by Dr. Rosalind Sadleir has been foundational in providing a diverse array of resources and skills needed to design and develop novel technologies, animal procedures and functional imaging techniques. I appreciate Dr. Sadleir for her scientific thinking, subject-knowledge expertise, mentoring and guidance; Dr. Chauhan, for his extensive MR imaging experience, mentoring and unrelenting support through various phases of the project; Jacquelyn Kilbourne, for her surgical expertise and animal care; Kenneth Lowe and Juliane Daggett, for their veterinary support services; Larisa Gilley, for her assistance in sterilizing carbon electrodes for animal use; Dr. Kodibagkar and Dr. Turner, for their MRI expertise, assistance and guidance with operation of the BNI-ASU 7 Tesla MRI scanner.

I would like to thank the members of my dissertation committee – Dr. Jitendran Muthuswamy, for his neurostimulation and electrochemistry expertise; Dr. Bradley Greger, for his knowledge and experience with the clinical translation of functional stimulation in animal models and neurostimulation; Dr. Stephen Helms Tillery, for his

guidance on functional electrical stimulation; and Dr. SungMin Sohn, for his expertise on MRI principles and MRI hardware.

The research work presented here was funded predominantly by the *National Institutes of Health* grant R01077004 awarded to Dr. Sadleir. Funds from the *Graduate and Professional Student Association* partially aided the procurement of surgical and imaging supplies through a merit-based research grant from *the Graduate Research Support Program*. Scholarships from the *School of Biological and Health Systems Engineering*, and travel grants from *Graduate and Professional Student Association* and *Alpha Eta Mu Beta* (*National Biomedical Honor Society*) funded travel and knowledge sharing at professional and academic conferences.

A special mention to my peers – Dr. Aprinda Indahlastari, Dr. Fanrui Fu, Dr. Shubhangi Agrawal, Dr. Rohini Shankar, Dr. Sajib, Sulagna Sahu, Nutan Jayadev, Babak Moghadas, Enock Boakye, Maame Afrifa, Gordon Fuller, Dzifa Kwaku and the student community at Arizona State University for an internationally diverse and immersive graduate school experience.

TABLE OF CONTENTS

Page

APPENDIX Page

LIST OF TABLES

LIST OF FIGURES

Figure Page

Figure Page

Figure Page

Figure Page

Figure Page

1. INTRODUCTION

Functional brain mapping research seeks to understand normal brain function, neurological disorders and disease states. Brain mapping techniques should ideally map neural activity at high spatial resolution – single neuron level – and high temporal resolution – sub-millisecond [1]. Functional brain mapping techniques can be categorized as – direct or indirect. Inverse electroencephalography (EEG) and magnetoencephalography (MEG) are well-known examples of direct neural activity mapping. Each has high temporal (i.e. ~ 1 ms) and low spatial resolution (i.e. ~ 1 cm) [1]. Magnetic resonance imaging (MRI)-based functional imaging methods such as functional MRI (fMRI) allow for better spatial localization of neuronal sources. However, hemodynamic mechanisms secondary to neural activity form the basis of the fMRI blood oxygenation level-dependent (BOLD) imaging contrast, and BOLD fMRI is therefore indirect in nature [1, 2]. A relatively new MRI-based direct neural mapping method, functional magnetic resonance electrical impedance tomography (fMREIT), is being developed to detect activity-related active membrane conductivity changes to directly map neural activity at spatial resolutions comparable with fMRI studies [3-6].

1.1 Background

Contemporary neural activity mapping methods ranging from electrophysiological recordings to noninvasive imaging techniques have an inherent tradeoff between spatial and temporal resolution, and degree of directness underlying measured neural and hemodynamic signals.

Electrophysiological recordings provide high spatial and temporal resolution on the scale of individual neurons with spatial extent limited to 2-3 neurons [7], however electrode placement may require invasive procedures. Optical imaging has been useful in studying neuronal populations that form neural circuits using intrinsic optical signals, voltage-sensitive dyes or optical stimulation [8, 9]. Light scattering has been a major challenge in optical imaging, which limits penetration depth and achievable imaging resolution [10]. Inverse EEG and MEG measure scalp electric and magnetic fields originating from active neuronal sources over larger regions of the cerebral cortex with high temporal resolution, low spatial resolution and localization of active neurons [11-13]. Fast neural electrical impedance tomography (EIT) has mapped neural activity related conductance changes at high spatial and temporal resolutions *in vivo* using invasive electrodes [14], however, accurate noninvasive mapping of active brain regions has not been possible in humans [15, 16]. BOLD fMRI serves as a workhorse for whole brain functional imaging in humans, having moderate spatial resolution and low temporal resolution [2]. BOLD fMRI signals are indirect measures of neural activity since BOLD signals originate from complex neurovascular coupling mechanisms [17, 18]. Molecular fMRI is being developed for cellular imaging using fMRI to facilitate whole brain coverage at high spatial resolution, however imaging agents with greater sensitivity and effective probe delivery are needed to conduct human studies [19].

Direct detection of neural activity using MRI involves the mapping of magnetic field perturbations generated by neuronal currents in active neural tissue [20]. The detection of intrinsic magnetic field changes is challenging because the size of expected signals is very low compared to typical MRI system noise levels. To date, *in vitro* [21] and *in vivo* [22] neuronal current(nc)-MRI studies have not demonstrated the feasibility to detect neural activity. MR phase signals in *in vitro* studies of devascularized cell culture preparations demonstrated the feasibility to detect spontaneous neural activity [23]. Direct detection of neuronal magnetic fields using alternate methods such as magnetic source MRI (msMRI) [24], Lorentz force imaging [25] and ultra-low field MRI [26] have not been found to be feasible using existing MR systems. Although the *in vivo* detection of transient and subtle magnetic fields associated with neural activity is difficult, *in vivo* detection of magnetic field perturbations caused by externally applied electrical currents has been possible in humans [27, 28]. During tissue electrical conductivity changes, the passage of externally applied electrical currents is altered, and the changes in electrical current pathways are reflected as magnetic field perturbations in the phase portion of complex MR images. While the intrinsic magnetic fields created by neural activity are very small, administration of external current during conductivity changes could result in changes in measured magnetic fields larger than MRI system noise levels. During action potential events, the membrane conductance of active neural tissue increases (~ 30 fold), thereby altering the pathway of externally applied imaging currents and

altering magnetic field perturbations measured in MR phase [3]. Functional studies of changes in MR phase images during neural activity use methods developed in the area of magnetic resonance electrical impedance tomography (MREIT) [29], and are referred to as functional MREIT (fMREIT).

Preliminary work comprising of simulation and *in vitro* fMREIT studies demonstrated the feasibility to detect changes in neural activity levels in the spontaneously firing *Aplysia* abdominal ganglion (AAG) [3-5]. Finite element modeling (FEM) studies of AAG neural complexes in artificial sea water (ASW) as neuronal current sources were conducted with moderate imaging resolutions to conduct feasibility studies for neural activity detection [3, 5]. Activity-related membrane conductance changes showed MR phase signal changes that scaled with MREIT imaging current amplitudes [5]. MR phase signal differences were found to depend solely on membrane conductance changes rather than neuronal current source strength [5]. Owing to the complex interaction between imaging currents and neuronal current sources, fMREIT is suited to study neuromodulatory mechanisms underlying electrical stimulation therapies such as Deep Brain Stimulation (DBS) [5].

In vitro tests of fMREIT using AAG tissue samples in background ASW solution at high field strengths of 11.8 T and 18.8 T demonstrated the *in vitro* proof-of-concept for fMREIT to detect neural activity in bloodless preparations [4, 6]. In

both experiments, neural activity was modulated through the administration of potassium chloride (KCl) into a background medium [4]. Significant increases in MR phase magnitudes were noted after (POST) KCl administration compared to prior (PRE) KCl conditions, within active regions [4]. Similar MR phase increases were not observed when ASW was added instead of KCl [4]. Significant differences were noted in Laplacian phase images within active tissue compartments due to membrane conductance changes associated with neural activity [6]. These *in vitro* studies provided evidence for the direct detection of spontaneous and modulated neural activity in bloodless preparations of active neural tissue [4, 6].

1.2 Rationale

This work is focused on the development of fMREIT for the *in vivo* detection of neural activity at 7 T field strength. Physiological variables such as blood flow, respiration rate, cardiac cycles and anesthetic depth could interact with and impact fMREIT phase signals generated by active neural tissue. As the first *in vivo* fMREIT study, the potentially confounding effects of non-neuronal physiological variables have not been encountered in previous FEM or *in vitro* AAG studies. In particular, the movement of conductive blood (conductivity, $\sigma = 0.67$ S/m) [30] around active neurons, the heterogeneous distribution of blood vessels and dynamically changing blood volumes in active regions could obscure fMREIT phase signals. Larger MR noise levels associated with the use of 7 T MR field

strength, compared to previous high field *in vitro* fMREIT studies, could also challenge the detection of subtle fMREIT phase changes associated with neural activity [31]. To compensate for the inherent increase in MR system noise at lower MR field strengths, fMREIT imaging currents were directly delivered into the hippocampus, thus avoiding electrical current attenuation through low-conducting skull tissue. In addition, MR-compatible carbon electrodes were developed for delivering hippocampal imaging currents to reduce MR signal losses around conventional platinum-iridium (Pt-Ir) neural stimulation electrodes.

Contemporaneous fMRI and fMREIT experiments were then designed to detect neural activity changes in anesthetized rodents. Evoked neural activity in the somatosensory cortex was achieved through electrical current stimulation of the forepaw [32, 33]. These cortical activations were induced using forepaw stimulation during fast MR pulse sequences, namely spin echo – echo planar imaging (SE-EPI), to record fMRI and fMREIT signals under *air* and *carbogen* inhalants.

1.3 Research Strategy

Experiments to determine the feasibility of *in vivo* detection of neural activity using fMREIT was conducted under two specific aims, as detailed below:

A. To develop and deploy MR-compatible current delivery electrodes into rodent hippocampi for *in vivo* fMREIT studies at preclinical MR field strengths.

Conventional neural stimulation electrodes, such as Pt-Ir electrodes used in DBS, could be useful for internal hippocampal imaging current delivery in *in vivo* fMREIT studies. However, susceptibility differences between implanted metal objects and surrounding tissues cause local magnetic field inhomogeneities and artifacts such as geometric distortion, fat suppression failure, signal loss and pile-up artifacts in MR images. Moreover, safety issues caused by the heating of metal objects, due to RF or gradient field switching, is a major limitation. Magnetic field strengths higher than 1.5 T, coupled with higher gradients, accelerated imaging sequences and gradient slew rates could potentially worsen the susceptibility artifacts and tissue heating associated with Pt-Ir electrodes, necessitating the development of MR-compatible alternatives to metals such as carbon electrodes for neuromodulation. Newly developed carbon electrodes were implanted within sub-cortical structures such as hippocampus to detect active somatosensory cortical regions in the rodent brain using fMREIT. Implanted carbon electrodes were maintained as parallel to the main magnetic field as possible to minimize contributions from magnetic fields surrounding current flowing through carbon electrodes.

B. To assess the feasibility of *in vivo* neural activity detection using fMREIT through the design and analysis of contemporaneous fMRI and fMREIT imaging experiments.

Functional imaging experiments (fMRI and fMREIT) were performed using a 7 T MRI system in anesthetized rodents implanted with carbon electrodes. Electrical currents were delivered between the second and fourth digits of the forepaw to evoke contralateral somatosensory cortical activations using a block design with 'On' and 'Off' periods of forepaw stimulation. Imaging currents were applied directly into the hippocampus using carbon electrodes to accrue fMREIT phase signals. fMRI and fMREIT imaging experiments were conducted using fast SE-EPI MR pulse sequences under two inhalants – *air* and *carbogen* – and three current injection waveforms – *continuous*, *interleaved with rest* and *interleaved with positive*. Complex MR data collected during fMRI and fMREIT experiments were analyzed to produce functional activation maps for each imaging modality. Activation maps showing statistically significant regions of differential neural activity corresponding to forepaw stimulation periods were assessed under each inhalant and current injection waveform.

1.4 Structural organization

Chapter 2 provides an anatomical overview of the nervous system from gross level brain structures to cellular level of neurons. Complex biophysical mechanisms underlying the establishment of neuronal membrane voltage and membrane conductance changes in response to neural activity are mathematically described using Hodgkin-Huxley equations. The conductivity contrast arising from single neurons to bulk electrical conductivity of tissues are described along with general imaging methods to map conductivity distributions using EIT and MREIT.

Chapter 3 extends the literature review of EIT and MREIT to use conductivity contrasts for functional brain mapping. EEG and MEG are reviewed as alternative modalities for the direct mapping of brain function. fMRI is described as it is the most commonly used neuroimaging tool based on indirect and secondary hemodynamic mechanisms related to neural activity.

Chapter 4 details the fabrication of novel MR-compatible carbon electrodes to deliver hippocampal imaging currents in fMREIT settings. Preliminary phantom and *ex vivo* studies were conducted at MRI field strengths of 7 T to assess magnitude artifacts, current density and magnetic flux density patterns, and heating in carbon electrodes compared to standard Pt-Ir metal electrodes.

Chapter 5 explains the experimental procedures developed to conduct preclinical functional imaging studies – fMRI and fMREIT. In particular, the development of an asceptic surgical procedure for the bilateral implantation of carbon electrodes into rodent hippocampi for imaging current delivery in fMREIT experiments is described. Preparing anesthetized rodents implanted with hippocampal carbon electrodes and forepaw stimulation electrodes are described as preparatory steps for functional imaging studies.

Chapter 6 describes the imaging paradigm consisting of anatomical and functional imaging sequences (fMRI and fMREIT) under two inhalants and three current injection waveforms during forepaw electrical stimulation in anesthetized rodents. Analysis of a single functional imaging dataset (fMRI and fMREIT) is described from assessing baseline noise levels to the computation of fMRI and fMREIT activation maps.

Chapter 7 uses the analysis described in Chapter 6 on multiple datasets to address research questions central to the verification of somatosensory activations caused by forepaw electrical stimulation, comparison of fMRI and fMREIT activation maps for similarities among activated brain regions, and assess the influence of changing inhalants and hippocampal imaging current waveforms on activation maps from both imaging modalities.

Chapter 8 summarizes the main findings on the feasibility of fMREIT to detect neural activity *in vivo* in whole organisms. Specifically, the influence of imaging current waveforms and inhalants on fMREIT phase signals, and therefore the conductivity contrast is discussed with recommendations for future *in vivo* fMREIT studies.

2. BIOPHYSICAL BASIS FOR CONDUCTIVITY CONTRAST IN ACTIVE NEURAL TISSUE

Neuronal signaling and information transfer in the nervous system occurs through the generation, propagation and conduction of electrical impulses along neurons. Neurons are interconnected by synapses to form neural circuits. Complex cellular and molecular mechanisms regulate the ease of electrical impulse conduction along neurons by modulating the membrane conductance of each neuron in a neural circuit. In neural tissue samples, the membrane conductance of a population of neurons is averaged over the entire tissue volume, and may affect the apparent electrical conductivity of neural tissue aggregates. The chapter focuses on the biological and physical mechanisms responsible for membrane conductance of neurons, and the anatomical and functional fundamentals of neurons in the nervous system.

2.1 Overview of the Nervous System

The central and peripheral divisions of the nervous system are comprised of neurons and supporting glial cells. These are responsible for signaling and communication between the nervous system and muscles and gland cells [34]. Neurons are the fundamental information processing units, and derive nutritive, protective and functional support from surrounding glial cells [35]. Structural and functional adaptations of neurons have been found to perform sensory, integrative and motor functions of the nervous system, as well as to interface with muscles,

tendons, and gland cells. The nervous system is described below, from gross anatomical to cellular levels to aid in the understanding of neuronal signaling and communication in the nervous system.

2.1.1 Central and Peripheral Nervous Systems

The central nervous system, comprised of the brain and spinal cord, controls the rest of the body through the peripheral nervous system that interfaces with muscles, organs and tissues. The brain is housed in the cranium and the spinal cord in the vertebral column surrounded by fluid-filled membranes known as meninges [36]. The three major divisions of the brain (forebrain, midbrain and hindbrain) and eight regions of the spinal cord (cervical, thoracic, lumbar and sacral) are as shown in **Figure 2.1**.

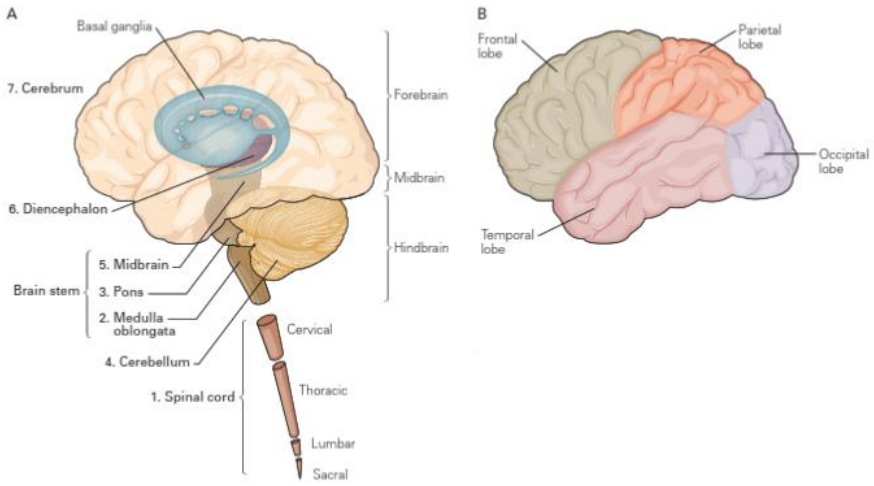

Figure 2.1: Central nervous system. (A) Major divisions of the brain and spinal cord. Three main regions of the brain – forebrain, midbrain and hindbrain. Four main segments of the spinal cord – cervical, thoracic, lumbar and sacral segments. (B) Four lobes of the cerebral cortex – frontal, parietal, temporal and occipital lobes [37].

A. Central Nervous System

The forebrain, midbrain and hindbrain are composed of brain structures tasked with highly specific functions. Forebrain comprises of the cerebrum, diencephalon and deep brain structures. The cerebrum consists of two cerebral hemispheres with a wrinkled outer surface known as the cerebral cortex. The cerebral cortex is further sub-divided into four distinct lobes - frontal, parietal, occipital and temporal lobes [35]. Deep brain structures are comprised of basal ganglia, hippocampus and amygdaloid nuclei. The basal ganglia are involved in motor performance, hippocampus in memory storage and amygdaloid nuclei coordinate the autonomic and endocrine responses of emotional states [35]. The midbrain controls sensory and motor functions, including eye movement and the coordination of visual and auditory reflexes [35]. The diencephalon regulates autonomic, endocrine and visceral functions [35]. The brain stem receives sensory information from the skin and muscles of the head, provides motor control for the head and conveys bidirectional information between the brain and spinal cord [35]. The medulla oblongata is responsible for critical autonomic processes such as digestion, breathing and heart rate regulation [35]. The pons convey motor information from cerebral hemispheres to the cerebellum [35]. The cerebellum modulates the

force and range of movement and is involved in the learning of motor skills [35]. The spinal cord is further subdivided into four regions of eight segments each, namely - cervical, thoracic, lumbar and sacral regions. Sensory information from the skin, joints and muscles of the limbs and trunk as well as movement of the limbs and trunk is controlled by the spinal cord [35].

B. Peripheral Nervous System

The peripheral nervous system is divided into somatic and visceral divisions, and is protected by the skin, muscles, fascia and organs. Afferent divisions of the peripheral nervous system relay sensory information to the central nervous system [36]. In general, peripheral nerves originate from the spinal cord or brain and innervate skin, muscles, organs and glands. The somatic division interfaces with the skin and skeletal muscles, whereas, the visceral or autonomic division innervates cardiac muscles, smooth muscles and receptors of organ systems in the body [36].

C. Information Transfer between Central and Peripheral Nervous Systems

An example of sensory information transfer from the peripheral to the central nervous system is sensory information relayed from peripheral nerves in the foot to the sensorimotor cortex of the brain [36]. Nerves

are bundles of long cellular extensions from neurons, as detailed in **section 2.1.2**. Sensory and motor cortices with respect to the four lobes of the brain are shown in **Figure 2.2**.

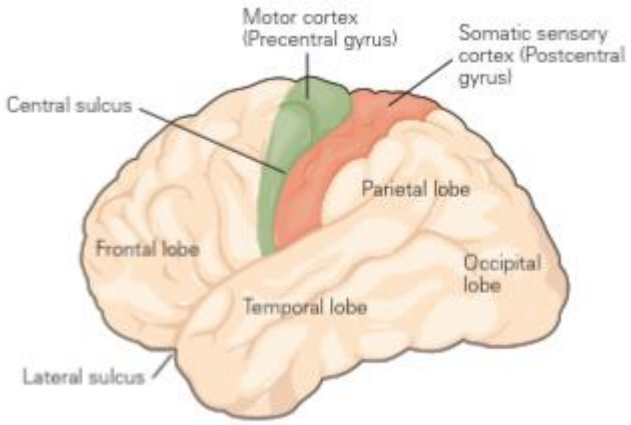

Figure 2.2: Four lobes of the cerebral cortex shown with the motor and sensory cortices separated by the central sulcus [35].

The transmission of sensory information involves three neuronal groupings, namely - primary, secondary and tertiary neurons. Information from stretch receptors in muscles, tendons and joints are encoded as electrical impulses, and delivered to the dendrites of primary neurons [36]. These impulses are carried along axons that ascend in the ipsilateral posterior column, to the lumbar and sacral segments of the spinal cord. Within the *medullospinal junction*, axon terminals of primary neurons terminate in the *gracile nucleus* [36]. Dendrites of secondary neurons transmit the electrical impulses along the axons, which cross the midline and extend into a major contralateral white matter pathway - *medial lemniscus* [36]. Secondary

neurons terminate at the ventral posterior lateral nucleus in the diencephalon. Tertiary neurons extend from the *ventral posterior lateral nucleus* onto the ipsilateral foot regions of the sensorimotor cortex [36].

2.1.2 Cells of the Nervous System

Neurons and glial cells are the two basic types of cells in the nervous system. Glial cells are the most prevalent cell type in the nervous system, amounting to ~90% of cellular population [38]. These cells provide protection and functional support to neurons that are actively involved in the generation, conduction and propagation of electrical signals for the purposes of neuronal signaling [35]. Both these cell types are described below, however, the precise function of glial cells has been an active area of research and still remains unknown [39].

A. Neuron

A neuron, also known as 'nerve cell', is the basic functional unit of the nervous system primarily responsible for information transfer between neurons. Electrical signals are the basis of information transfer, and neurons have the capacity to passively and actively conduct electrical signals owing to the highly specialized structure of a neuron.

A typical neuron has four morphologically defined regions - cell body, dendrites, axon and presynaptic terminals [36], as shown in **Figure 2.3**. The cell body or soma is the metabolic center of the cell containing organelles necessary to preserve cell structure and function, including the nucleus, endoplasmic reticulum and nucleolus [36]. Two kinds of processes arise from the cell body: several short dendrites and one long, tubular axon [36]. Dendrites are tree-like extensions from the cell body, and contain receptors for receiving signals from other nerve cells [36]. Dendrites receive input from other neurons or from sensory receptors, and generate electrical currents in response to these inputs [36]. These electrical currents undergo a summation at the axon hillock within the cell body. The electrical signals, called action potentials, are initiated at a specialized trigger region near the origin of the axon, called the initial segment from which they propagate down the axon [36]. The axon conveys electrical signals from the cell body over distances within the range of 0.1 mm to 2 m at speeds of 1 to 100 m/s without distortions [35]. The amplitude of an action potential traveling down the axon remains constant at 100 mV because the action potential is an all-or-none impulse that is regenerated at regular intervals along the axon [36].

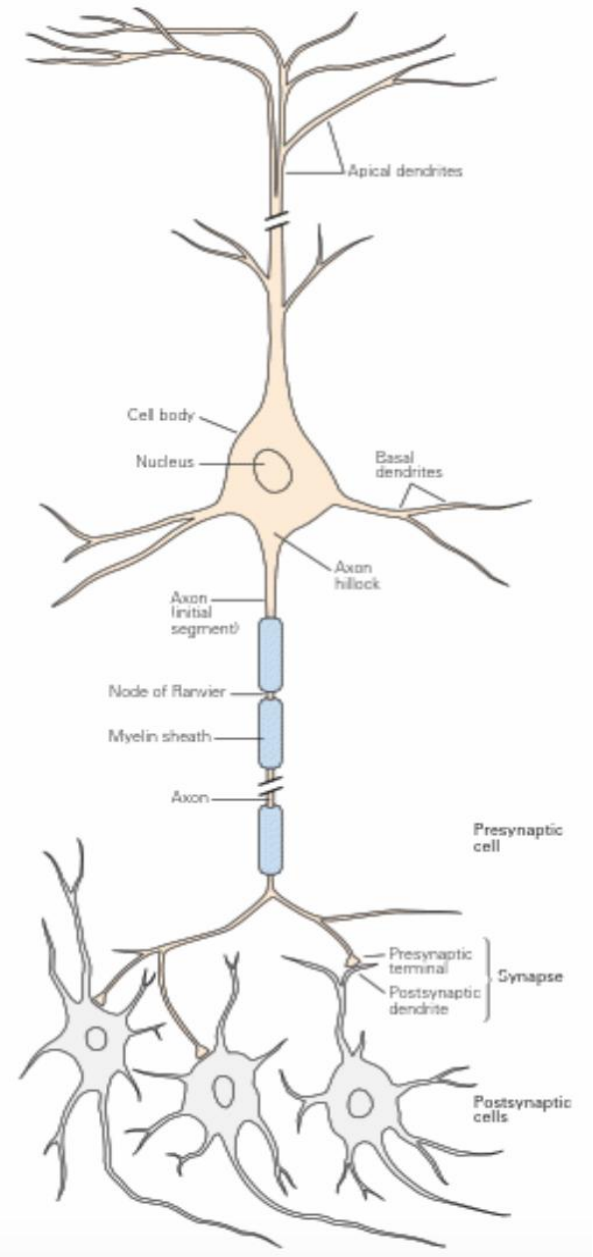

Figure 2.3: Structure of a typical neuron comprised of dendrites, cell body, axon and presynaptic terminals forming synapses with three postsynaptic neurons [35].

The myelin sheath insulates axons from fluids in the extracellular space of the central nervous system, thereby increasing the speed of conduction of action potentials along the axon [36]. The sheath is

interrupted at regular intervals by the Nodes of Ranvier, where the action potential is regenerated [35]. The axon divides into fine branches at the end to form axon terminals. Action potentials are transmitted to other neurons or muscles from presynaptic terminals through specialized zones of communication known as synapses [35]. The neuron transmitting the signal is called presynaptic cell, and the cell receiving the signal is called the postsynaptic cell. The presynaptic and postsynaptic cells are separated by a very narrow space known as the synaptic cleft [35]. Vesicles containing neurotransmitters such as glutamate are released into the synaptic cleft for uptake by dendritic receptors of postsynaptic cells [36].

B. Glial Cells

Glial cells are the most prevalent cell type in the nervous system, amounting to ~90% of the cellular population [38]. The two major classes of glial cells – microglia and macroglia – provide nutritive, protective and functional support to neurons, that constitute 10% of the cellular population in the nervous system [38]. Microglia protect neural tissue from injury, infection and degenerative diseases [36]. Macroglia can further be subdivided into oligodendrocytes, Schwann cells and astrocytes [36]. Oligodendrocytes and Schwann cells wrap around axons in the central and peripheral nervous systems

respectively, to form a lipoproteinaceous membrane called myelin [36]. Additionally, the peripheral nervous system is supported by satellite cells, fibroblasts and blood vessels [39].

2.1.3 Functional Classification of Neurons

Neurons are functionally categorized as sensory neurons, motor neurons and interneurons as shown in **Figure 2.4**. Sensory neurons are involved in sensory perception and motor coordination. These neurons transfer information from peripheral sensors and receptors to the nervous system [35]. Motor neurons carry information from the brain or spinal cord to muscles and glands [35]. Interneurons are divided into two sub-types, namely relay and local. Relay or projection interneurons have long axons to transfer information between brain regions. Local interneurons have short axons and form connections with nearby neurons in local circuits [35].

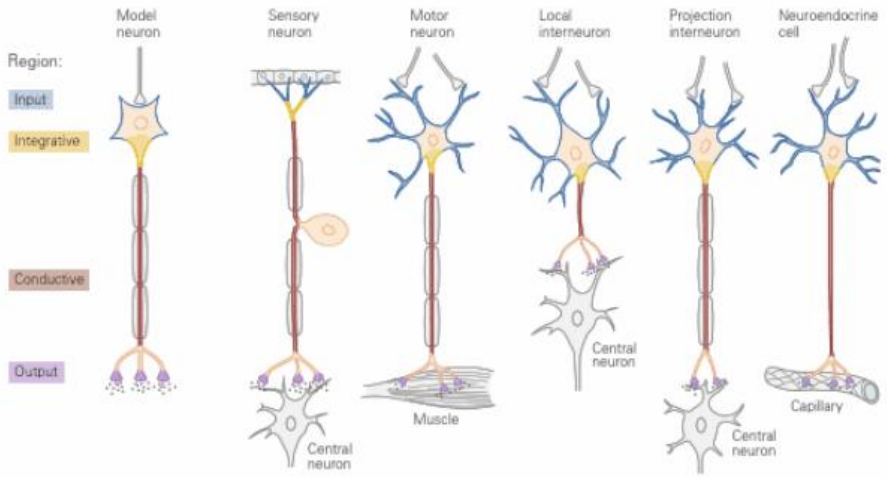

Figure 2.4: Functional classification of neurons. Three major types of neurons – Sensory neuron, Motor neuron and Interneuron. Common functional components of neuron types represented by a 'model' neuron [35].

Almost all neurons, regardless of cell size or morphology, has four functional components that generate four types of signals, namely – a receptive component, an integrative component, a conductive component and a secretory component [35]. These components may be represented by a generic 'model' neuron as shown in **Figure 2.4**. The receptive component refers to signal induction through dendrites [35]. Electrical currents induced at synaptic dendrites flow down the cell body to the axon hillock for summation or integration [35]. If an integrated electrical current surpasses the threshold, then an action potential is generated and conducted along the length of the axon, until the action potential arrives at the postsynaptic terminals of the neuron [35]. At these terminals, the electrical currents trigger the release of neurotransmitters into the synaptic

cleft, and is referred to as the secretory component as a means of neuronal signaling and communication through the nervous system [35].

2.2 Origins of membrane conductance as a biomarker for neural activity

Neuronal signaling uses electrical signals as the basis for information transfer in the nervous system [40]. Neural activity may manifest as transient electrical signals, including local field potentials, receptor potentials, synaptic potentials, as well as action potentials to carry time-sensitive information to target cells [35]. Neurons conduct electrical signals along the length of an axon through the passage of ions between intracellular and extracellular spaces. Voltage-gated ion channels acting in tandem with electrical and chemical gradients, and membrane conductance regulate the flow of ions across neuronal membranes [35]. Changes in neuronal membrane conductance directly impacts the passage of charged ions, and therefore ionic current flow across neuronal membranes [35]. The biophysical and electrochemical phenomena responsible for neuronal membrane conductance, passive and active behaviors of neural tissue are discussed below.

2.2.1 Electric Potential and Electric Field

Quasistatic approximations apply to electrophysiological problems, and therefore the electric field is defined as [41]:

$$\boldsymbol{E} = -\nabla\phi, \qquad [2.1]$$

where ϕ denotes the electric potential (V).

According to Ohm's law, current density $\boldsymbol{J}$ and electric field $\boldsymbol{E}$ are related by [41]:

$$\boldsymbol{J} = \sigma \boldsymbol{E} = -\sigma \nabla \phi, \quad [2.2]$$

where σ = conductivity of the medium.

Ions present in extracellular or intracellular spaces are subjected to electric field forces. The flux of a specific ion through a surface (i.e. flow per unit area per unit time) in the presence of an electric field depends on the ionic mobility and the electric field strength. Ionic flux is given as [41]

$$\boldsymbol{j_{ke}} = -u_k \frac{z_k}{|z_k|} c_k \nabla \phi, \quad [2.3]$$

where $\boldsymbol{j_{ke}}$ = ionic flux (due to electric field) (mol/cm^2.s),

u_k = ionic mobility (cm^2/(V.s)) is the velocity of the kth ion in a unit electric field,

z_k = valence of the ion,

c_k = ionic concentration (mol/cm^3),

$\frac{z_k}{|z_k|}$ = sign of force (positive for cations and negative for anions),

$-u_k \frac{z_k}{|z_k|}$ = mean velocity achieved by these ions in a unit electric field.

Ionic mobility is proportional to the conductivity of the k^{th} ion in the electrolyte. Furthermore, ionic mobility depends on the viscosity of the solvent and the size and charge of the ion. From the units, multiplying concentration by velocity gives the ionic flux [41].

2.2.2 Diffusion

The flow of ions from regions of high density to low density to redistribute charge that results in a uniform distribution is called Diffusion, and ionic flux due to diffusion is described by Fick's law [41]:

$$\boldsymbol{j_{kD}} = -D_k \nabla c_k, \quad [2.4]$$

where $\boldsymbol{j_{kD}}$ = ionic flux (due to diffusion) (mol/cm^2.s), D_k = Fick's constant (cm^2/s), c_k = ion concentration (mol/cm^3).

The negative sign describes flux in the direction of decreasing concentration. Fick's constant relates the force due to diffusion ($-\nabla c_k$) to the flux of the kth substance. Similarly, mobility couples the electric field force ($-\nabla \phi$) to the resulting ionic flux [41].

The diffusion constant is related to mobility as:

$$D_k = \frac{u_k RT}{|z_k|F}, \quad [2.5]$$

where R = gas constant (8.314 J/(mol.K)) and T = absolute temperature (K).

2.2.3 Nernst Planck Equation

The total ionic flux for the kth ion ($\boldsymbol{j_k}$) describes the flux of the kth ion under the influence of both a concentration gradient and an electric field and is known as the Nernst-Planck equation as [41]:

$$\boldsymbol{j_k} = \boldsymbol{j_{kD}} + \boldsymbol{j}_{ke} = -D_k\left(\nabla c_k + \frac{c_k z_k F}{RT}\nabla\Phi\right) \quad [2.6]$$

The total ionic flux ($\boldsymbol{j_k}$) can be converted into an electrical current density ($\boldsymbol{J_k}$) by multiplying with $z_k F$ (units = Coulombs) as [41]:

$$\boldsymbol{J_k} = \boldsymbol{j_k} z_k F,$$

$$\boldsymbol{J_k} = -D_k z_k F(\nabla c_k + \frac{c_k z_k F}{RT}\nabla\Phi). \quad [2.7]$$

2.2.4 Membrane Potential

In the absence of action potentials, neurons are considered to be in a state of *rest*. At rest, the membrane is relatively impermeable to ions, thereby creating a separation of positive (Na^+, K^+) and negative charges (Cl^-) at the cell membrane of the neuron, as shown in **Figure 2.5**. Sodium-Potassium (Na^+-K^+) pumps present in the cell membrane actively maintain the charge separation by moving ions against their electrochemical gradients, as described in **Section 2.2.6**. The extracellular surface of the membrane has an excess of positive charges, whereas the cytoplasmic surface has an excess of negative charges. Such charge separation is maintained at the lipid bilayer as a barrier to the diffusion of ions, and therefore establishes a constant voltage at the neuronal membrane [35].

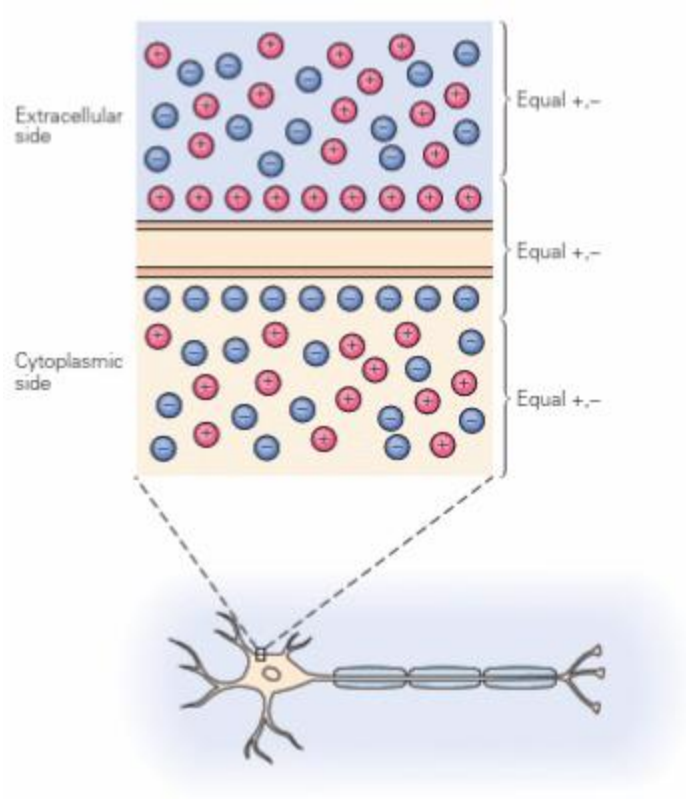

Figure 2.5: Charge separation across the cell membrane establishes an electrical potential, also known as the membrane potential [35].

The charge separation leads to an electrical potential difference, or voltage, known as the membrane potential (V_m) defined as [35],

$$V_m = V_{in} - V_{out}, \quad [2.8]$$

where V_{in} is the potential inside of the cell and V_{out} is the potential outside of the cell. The membrane potential of a cell at rest is known as the resting membrane potential, and typically is in the range of -60 mV to -70 mV [35]. During electrical signaling, the net flow of ions into or out of the cell leads to electrical currents across the cell membrane. These currents change the charge separation across the cell membrane, and therefore lead

to slight deviations from the resting membrane voltage. Small changes in membrane potentials that do not lead to the opening of gated ion channels are passive responses of the membrane, and are known as electrotonic potentials [35]. The membrane potential (V_m) changes in response to incoming electrical signals are therefore critical in neuronal signaling.

2.2.5 Ion Channels

Ion channels are dispersed across the cell membrane and primarily regulate the movement of ions across neuronal membranes. The two main types of ion channels are resting and gated ion channels [35]. Resting channels aid in the maintenance of the resting membrane potential in the absence of signaling. Resting channels are typically open, however, some types are gated by changes in membrane voltage. These channels open at the negative resting potential of neurons. The other type of ion channels, for example voltage-gated ion channels, need membrane depolarization to open and allow ions to pass through the channel [35].

Considering membrane permeability to specific ion species, the higher relative concentrations of K^+ ions inside the cell create a chemical concentration gradient such that K^+ ions diffuse out of the cell [35]. The resulting excess of K^+ ions outside the cell produces a net positive charge outside the cell. Therefore, K^+ ions are subjected to two driving forces: a chemical driving force (i.e. diffusion force) because of the concentration

gradient and, an electrical driving force – due to the electrical potential difference across the membrane, as shown in **Figure 2.6**. The potential at which both forces are balanced, i.e. K^+ efflux driven by the chemical concentration gradient is balanced by K^+ influx driven by the electrical potential difference, is known as the K^+ equilibrium potential (E_K). In general, the transmembrane potential achieved at equilibrium is known as the equilibrium potential. When a cell membrane is permeable only to K^+ ions, the resting membrane potential is the same as E_K, measured as -75 mV [35].

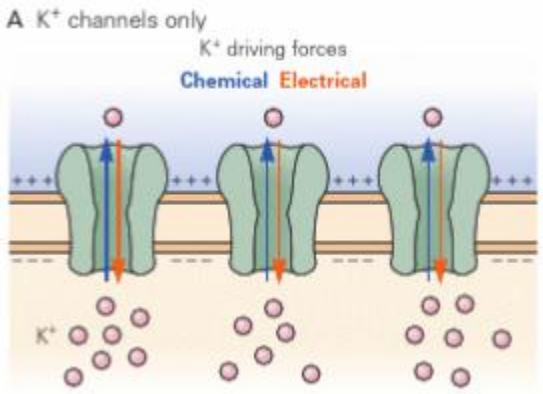

Figure 2.6: Movement of K^+ ions across a cell membrane driven by an outward chemical concentration gradient and inward electrical potential difference [35].

At equilibrium, the membrane must satisfy a zero current condition with K^+ ion as the k^{th} ion in the Nernst Plank equation as:

$$\boldsymbol{J_k} = 0 = -D_k z_k F(\nabla c_k + \frac{c_k z_k F}{RT}\nabla\Phi) \qquad [2.9]$$

Solving the above equation for equilibrium voltage across the membrane for the kth ion is, $E_k = \Phi_i - \Phi_o$, and therefore:

$$E_k = -\frac{RT}{z_k F} ln \frac{c_{i,k}}{c_{o,k}} \quad [2.10]$$

where E_k = equilibrium voltage for kth ion across the membrane i.e. Nernst voltage (V), R = gas constant (8.314 J/(mol.K), T = absolute temperature, z_k = valence of kth ion, F = Faraday's constant (9.65 x 10^4 C/mol), $c_{o,k}$ = extracellular concentration of kth ion, $c_{i,k}$ = intracellular concentration of kth ion. Substituting T as 37^{o}C, z_k as +1 and converting logarithm base e to logarithm base 10, **equation 2.10** may be simplified as [41],

$$E_k = -61\ log_{10} \frac{c_i}{c_o} \text{ [mV]} \quad [2.11]$$

Using **equation 2.11**, the equilibrium potential or Nernst potential of K^+ ions may be calculated using z = +1, $[X]_o$ = 20 and $[X]_i$ = 400 as -75 mV [35]. If $V_m = V_K$, the diffusion and electric field forces are balanced. Therefore, no net flow of K^+ ions exists through the membrane [41]. If $|V_m| < |V_K|$, then the potential inside the membrane becomes less negative, known as depolarization of the membrane. The electric field is insufficient to equilibrate diffusional forces. This imbalance is $\Delta V = V_m - V_K$ and an outflow of K^+ ions results [41]. If $|V_m| > |V_K|$, then the potential inside the membrane becomes more negative than the resting state, and is said to be hyperpolarized causing an inflow of K^+ ions [41].

A single K^+ ion channel may be represented as a conductor with conductance (γ_K) [35], and the electrochemical driving force ($V_m - E_K$) generating K^+ ion flow as shown in **Figure 2.7**. The flow of current through a single K^+ ion channel in the presence of a K^+ electrochemical gradient is [35],

$$i_K = \gamma_K \, (V_m - E_K) \qquad [2.12]$$

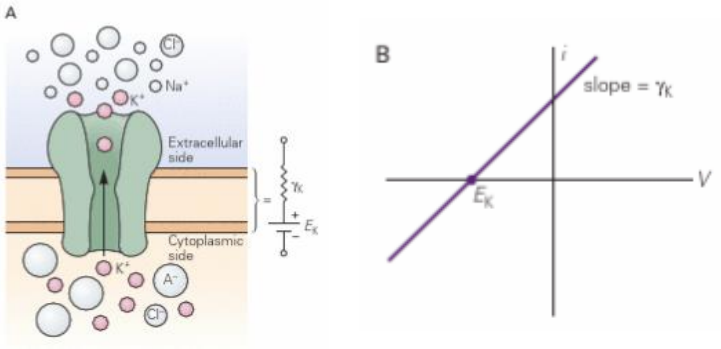

Figure 2.7: Electrochemical driving force acting on K^+ ions through a single K^+ ion channel [35].

For a cell membrane with N_K number of K^+ ion channels, the total conductance of all K^+ ion channels can be combined into a single equivalent conductor of conductance (g_K) as shown in **Figure 2.8**. Similar total conductance expressions for Na^+ and Cl^- ion channels may be formulated [35]. The mathematical formulation of g_K is,

$$g_K = N_K \, \gamma_K. \qquad [2.13]$$

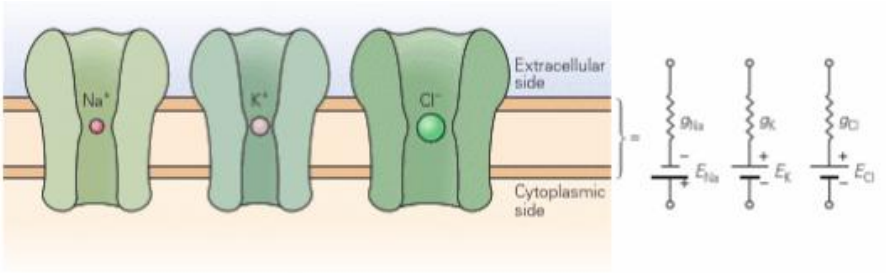

Figure 2.8: Electrical circuit representations of Na^+, K^+ and Cl^- ions under electrochemical driving forces represented as a resistor in series with a battery. The resistor models the ease of ion movement and the battery depicts the electrochemical driving force arising from concentration gradients per ion species [35].

At rest, nerve cell membranes are permeable to three ion species – Na^+, K^+ and Cl^- ions. Na^+ and Cl^- ions are concentrated outside the cell, whereas K^+ and other organic anions are concentrated inside the cell. The permeability of the cell membrane to a specific ion species depends on the proportion of ion channels that are open [35]. Conductance values of Na^+, K^+ and Cl^- ion channels across the cell membrane contribute to the overall membrane conductance.

2.2.6 Ion pumps

Sodium-potassium (Na^+-K^+) pumps actively transport Na^+ and K^+ ions against the electrochemical gradients of each ion species i.e. Na^+ efflux and K^+ influx [35]. The pump hydrolyzes ATP for energy to continually maintain the ionic gradients for Na^+ and K^+ ions, as shown in **Figure 2.9**. Therefore, the resting membrane potential is in steady state rather than

equilibrium. The continuous passive influx of Na^+ and efflux of K^+ is counterbalanced by the Na^+-K^+ pump [35].

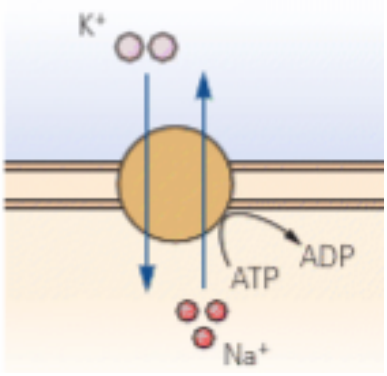

Figure 2.9: Energy conversion (ATP → ADP) in Sodium-Potassium (Na^+-K^+) pump powers the movement of Na^+ and K^+ ions against the electrochemical gradient across a cell membrane [35].

In the absence of Na^+-K^+ pump, the imbalance between Na^+ and K^+ ions will not be maintained, and Na^+ and K^+ ions will reach equilibrium. Large ion movements cause changes in ionic concentrations of Na^+, K^+ and Cl^- ions. At equilibrium, every ion is at its Nernst potential, also known as the common transmembrane potential. When all ions are in equilibrium, the phenomenon is referred to as the Donnan equilibrium and is represented as [41]:

$$\frac{c_{o,K}}{c_{i,K}} = \frac{c_{o,Na}}{c_{i,Na}} = \frac{c_{i,Cl}}{c_{o,Cl}}. \qquad [2.14]$$

2.2.7 Goldman-Hodgkin-Katz Equation

In general, the resting membrane potential is influenced by Na^+, K^+ and Cl^- ions in terms of the concentration of each ion species and the

permeability of the cell membrane to the ion type [35]. The permeability (P) is a measure of the ease with which an ion crosses the cell membrane in cm/s. The Goldman equation is an extension of the Nernst equation, which is suitable to single ion types, and explains the membrane potential as a function of ionic permeability and concentration of Na^+, K^+ and Cl^- ions as [35]:

$$V_m = \frac{RT}{F} ln \frac{P_K[K^+]_o + P_{Na}[Na^+]_o + P_{Cl}[Cl^-]_i}{P_K[K^+]_i + P_{Na}[Na^+]_i + P_{Cl}[Cl^-]_o}. \quad [2.15]$$

where $[K^+]_o$, $[Na^+]_o$ and $[Cl^-]_o$ demonstrate extracellular concentrations of K^+, Na^+ and Cl^- ions, and $[K^+]_i$, $[Na^+]_i$ and $[Cl^-]_i$ demonstrate intracellular concentrations of K^+, Na^+ and Cl^- ions.

At rest, the permeability ratios were reported as $P_K : P_{Na} : P_{Cl} = 1.0 : 0.04 : 0.45$, whereas these ratios at the peak of an action potential reach $P_K : P_{Na} : P_{Cl} = 1.0 : 20.0 : 0.45$ [35]. Therefore, at the peak of the action potential the membrane voltage almost reaches E_{Na} (i.e. +55 mV) [35].

2.2.8 Cable Equation of the Axon

As a neuron receives input at a dendritic terminal, an electrical signal is produced at the synaptic input of the dendrite. The signal is integrated with other inputs to the neuron at the initial segment of the axon [35]. The passive electrical properties of a neuron critical to the generation of an

action potential are the membrane conductance ($g_r = 1/R_r$), the membrane capacitance (C_m) and intracellular axial resistance (r_a) [35]. Signal conduction within the cell body is not prone to signal decay because the small-sized cell body may be approximated as a tiny sphere of constant membrane voltage [35]. However, subthreshold voltages traveling along longer structures such as axons decay with distance from the site of current injection. Under subthreshold conditions, the cell membrane can be modeled as a uniformly distributed cylinder as shown in **Figure 2.10**. The excitatory electric impulse (I_S) flows axially inside the axon as the total stimulus current (I_i), which diminishes with distance small currents cross the membrane and flow outside the axon.

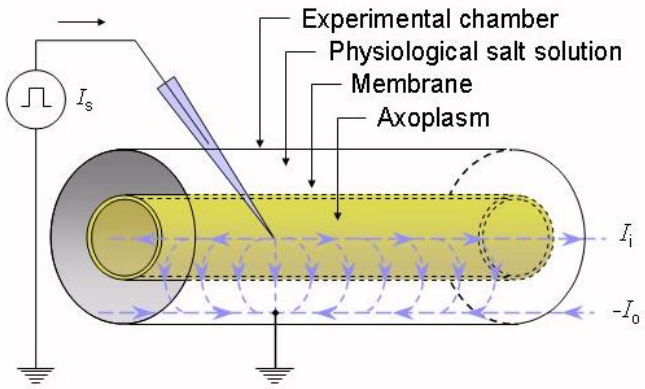

Figure 2.10: Cable model of an axon. An excitatory electric impulse (I_S) applied to an axon divides into total stimulus current (I_i) flowing inside the axon and current outside (I_o) the axon [41].

The equivalent circuit of the cable model of an axon is shown in **Figure 2.11**. The long, slender shape of the axon limits most of the current to flow

in the axial direction. Therefore, an axial resistance (r_o) was used to represent interstitial fluid. The subthreshold membrane is modeled as a distributed resistance (r_m) and capacitance (c_m) in parallel. The resistance (r_m) accounts for the ionic membrane current (i_{mi}). The capacitance (c_m) demonstrates the poor conductive yet better dielectric properties of the membrane, thereby showing a membrane capacitive current (i_{mc}). The axial intracellular and extracellular paths are entirely resistive [41].

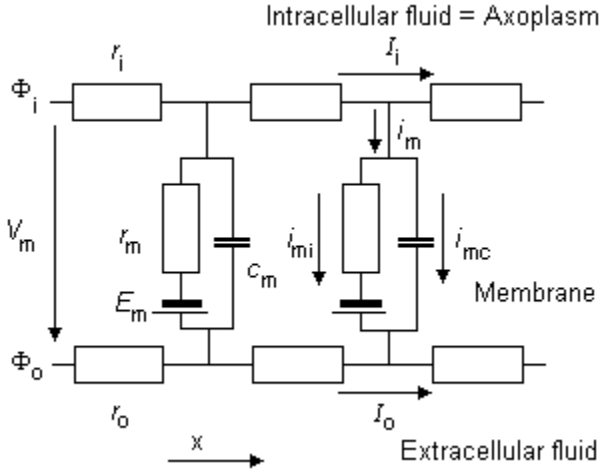

Figure 2.11: Equivalent circuit model of an axon [41].

In the absence of stimulating currents (i.e. $I_i = I_o = I_m = 0$), then $V_m = V_r$ and $V' = 0$. However, once activity has been initiated, V_r is constant, and therefore,

$$\frac{\partial V'}{\partial x} = \frac{\partial V_m}{\partial x},$$

$$\frac{\partial V'}{\partial t} = \frac{\partial V_m}{\partial t}, \qquad [2.16]$$

where $V' = V_m - V_r$ = deviation of membrane voltage from resting state (mV), $V_m = \phi_i - \phi_o$ = membrane voltage (mV).

A. Steady state response

The steady state condition is the stationary case achieved by the application of a current step. The resulting general cable equation is:

$$\frac{\partial^2 V'}{\partial x^2} = (r_i + r_o) i_m, \quad [2.17]$$

where r_i = intracellular axial resistance of the axoplasm per unit length of axon, r_o = extracellular axial resistance of the (bounding) extracellular medium per unit length of axon, i_m = total transmembrane current per unit length of axon.

Under stationary and subthreshold conditions, the deviation in membrane voltage is:

$$V' = V'(0) e^{-x/\lambda}, \quad [2.18]$$

where λ = characteristic length or length constant of an axon or space constant. **Figure 2.12** shows the solution to V', where V' decreases exponentially along the axon until the amplitude diminishes to 36.8% of the value at the point of stimulation at $x = \lambda$.

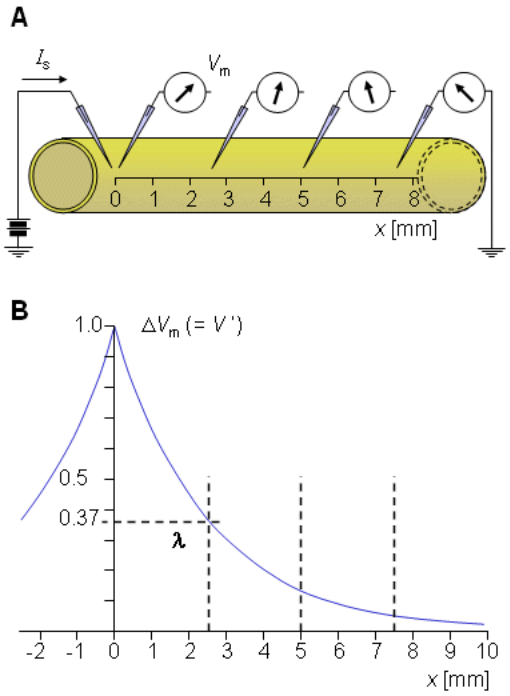

Figure 2.12: Cable model of axon under current step. (A) Stimulation of a nerve with current step. (B) Variation of the membrane voltage as a function of distance [41].

B. Stimulation with Step-Current Impulse

The transient response (rather than steady state response) of the axon to a subthreshold current-step input is shown in **Figure 2.13**. The deviation in membrane voltage may be formulated as [41]:

$$-\lambda^2 \frac{\partial^2 V'}{\partial x^2} + \tau \frac{\partial V'}{\partial t} + V' = 0, \qquad [2.19]$$

where $\tau = r_m c_m$ is the time constant of the membrane, λ = space constant.

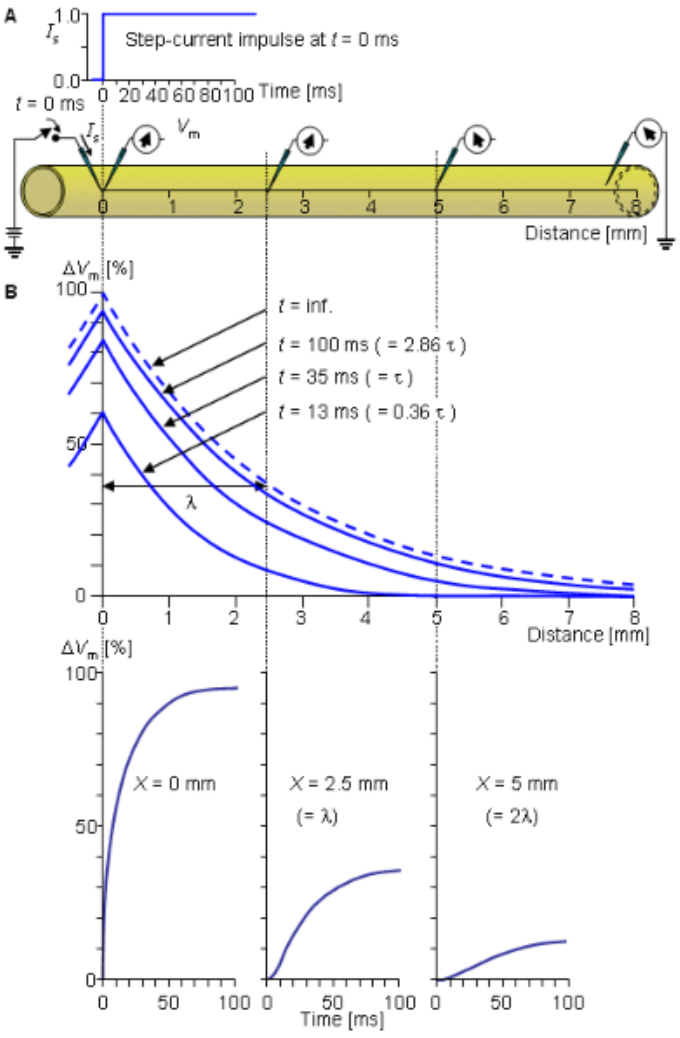

Figure 2.13: Response of axon to step current impulse. (A) Axonal model with current waveform, and stimulating and recording electrodes. (B) Spatial response at t = 13 ms, 35 ms, 100 ms, ∞ (i.e. steady-state response). (C) Temporal response at three axial sites, x = 0, 2.5, 5 mm [41].

The cumulative capacitance and resistance properties of the membrane influence the change in membrane potential as,

$$\Delta V_m(t) = I_m R_m(1 - e^{-t/\tau}), \qquad [2.20]$$

where τ is the membrane time constant ($\tau = R_m C_m$) [35]. For a step current as input, the change in membrane voltage is shown in **Figure 2.14**.

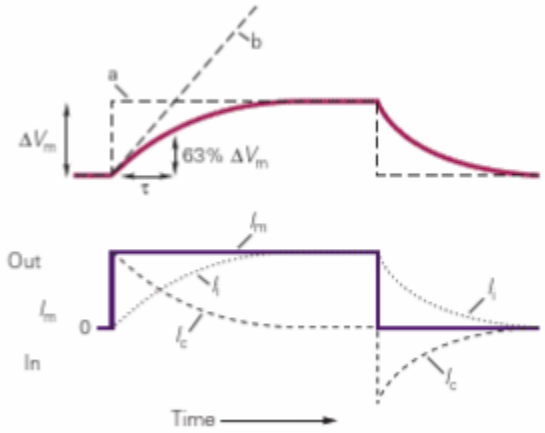

Figure 2.14: Rate of change of membrane potential (ΔV_m) with membrane resistance (R_m) and capacitance (C_m) for a current input (I_m) [35].

2.2.9 Equivalent Electrical Circuit Model of a Neuron

Ionic flow through voltage-gated ion channels may be represented by an equivalent electrical circuit, as shown in **Figure 2.15**. Changes in V_m caused by sub-threshold currents, influence the opening of Na^+ and K^+ ion channels. When V_m increases, there is an increase in $g_{Na}$and g_K as the opening of Na^+ and K^+ ions is voltage-dependent [35]. Ion channel conductance for Na^+, K^+ and Cl^- ions are modeled as resistors in series with batteries that represent the electrochemical driving force for each ion species. The Na^+-K^+ pump engaged in the active transport of Na^+ and K^+ ions against corresponding concentration gradients is also shown [35].

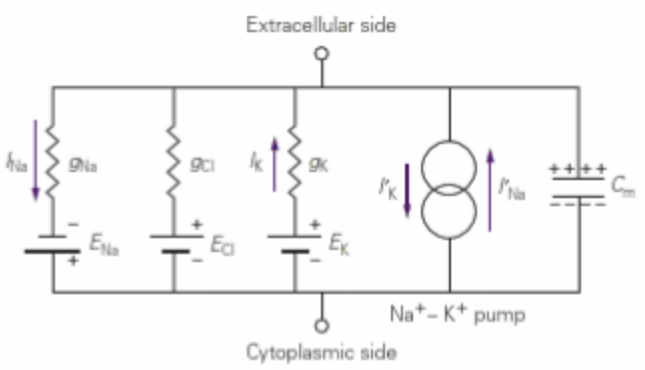

Figure 2.15: An equivalent circuit of passive and active currents in a neuron. Passive Na^+ and K^+ ionic currents (I_{Na}, I_K) are balanced by active currents (I'_{Na}, I'_K) generated by a Na^+-K^+ pump in the steady-state. Under depolarization, the passive and active Na^+ currents are 50% larger than K^+ as the pump transports 3 Na^+ ions out of the cell for every 2 K^+ ions into the cell [35].

The size of Na^+ and K^+ currents depend on the ionic conductance g_{Na} and g_K, which is a function of the number of open Na^+ and K^+ channels, as well as the electrochemical driving force for Na^+ ions as $(V_m - E_{Na})$ and K^+ ions as $(V_m - E_K)$ as [35]:

$$I_{Na} = g_{Na}\,(V_m - E_{Na}), \qquad [2.21]$$

$$I_K = g_K\,(V_m - E_K). \qquad [2.22]$$

Voltage clamp experiments in neurons, wherein the membrane voltage was held constant and varied in a graded fashion while measuring the resulting current through Na^+ and K^+ channels, were used to experimentally determine the conductance of Na^+ and K^+ ions [35].

2.2.10 Conduction of the Nerve Impulse in an Axon

The velocity of nerve impulse propagation in an unmyelinated axon [41]:

$$v = \sqrt{\frac{i_{Na\,max}}{r_i c_m^2 V_{th}}} \qquad [2.23]$$

where v = velocity of nerve impulse (m/s), $i_{Na\,max}$ = maximum sodium current per unit length (A/m), V_{th} = threshold voltage (V), r_i = axial resistance per unit length (Ω/m), c_m = membrane capacitance per unit length (F/m).

2.2.11 Generation and Propagation of an Action Potential

Voltage-gated ion channels are critical for the generation and propagation of action potentials, also known as spikes or impulses [35]. As axons can be long with poor electrical conducting properties, neurons evolved a "booster system" to conduct electrical signals over large distances using spikes [40]. An action potential is generated when the membrane voltage reaches the threshold voltage. In the case shown in **Figure 2.16**, this is at approximately -55 mV [35]. The generation of an action potential is an all-or-nothing event. Therefore, a larger depolarizing current will generate an action potential of the same size and shape as does a current that only meets the threshold [35]. As the action potential is conducted along the length of an axon, it is continuously regenerated and therefore does not attenuate over long distances [35]. Immediately after conducting an action

potential, a neuron is unresponsive to further depolarizing currents for a period of time known as refractory period. The refractory period therefore limits the frequency information-carrying capacity of a neuron [35].

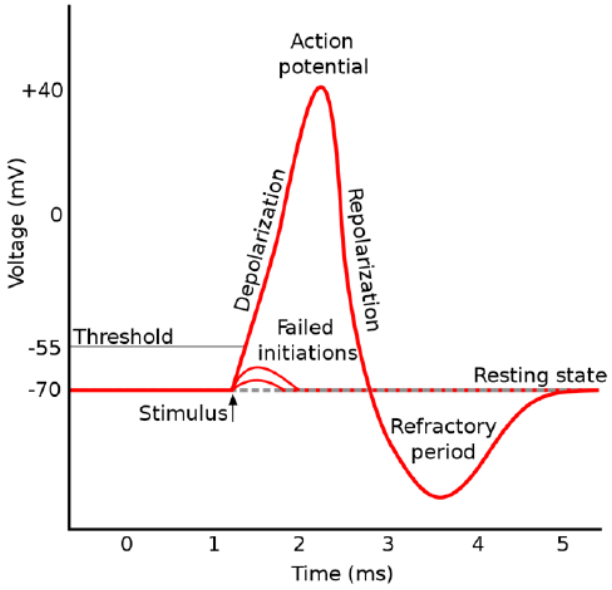

Figure 2.16: Schematic of an action potential. If the membrane voltage (V_m) crosses the threshold, then an action potential – comprising of depolarization and repolarization phases – is generated to conduct electrical impulses along a neuron [35].

2.2.12 Hodgkin-Huxley Membrane Model

Action potentials result from an increase in ionic conductance of the axon membrane, as shown in **Figure 2.17**. The sequence of events during an action potential are described by the Hodgkin-Huxley model [35], wherein membrane depolarization causes voltage-gated Na^+ channels to open rapidly, thereby causing an increase in g_{Na} resulting in an inward Na^+ current [35]. As the membrane capacitance is discharged, further depolarization is caused by opening more Na^+ channels, resulting in a

further increase in inward current [35]. The increase in g_{Na} and further depolarization of the membrane is a regenerative process that increases the membrane voltage to E_{Na}. The increase in g_{Na} leads to the rising phase (i.e. depolarization) of the action potential [35] as shown in **Figure 2.16** and **Figure 2.17**.

As V_m approaches E_{Na}, g_{Na} decreases leading to a reduction in I_{Na}, and after a small delay, g_K increases thereby increasing I_K. Overall, the reversal of Na^+ and K^+ currents leads to the falling edge (i.e. repolarization) of the action potential [35], as shown in **Figure 2.16** and **Figure 2.17**. Usually, the action potential is followed by a transient decrease of V_m to values more negative than the resting potential. The negative overshoot occurs because the K^+ channels that open during repolarization remain open for a few milliseconds after the membrane voltage returns to the closed state [35].

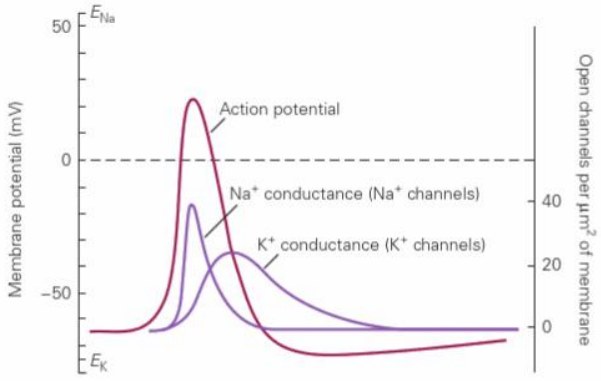

Figure 2.17: Sequential opening of voltage-gated Na^+ and K^+ channels generates the action potential [35].

The cell membrane may be modeled as a parallel conductance model as shown in **Figure 2.18**. The electric current flowing across the cell membrane during activation is a sum of the current carried by sodium ions, potassium ions, leakage current and capacitive (displacement) current. Sodium, potassium and leakage conductance per unit area based on Ohm's law are:

$$G_{Na} = \frac{I_{Na}}{V_m - V_{Na}},$$

$$G_K = \frac{I_K}{V_m - V_K},$$

$$G_L = \frac{I_L}{V_m - V_L}, \qquad [2.24]$$

where G_{Na}, G_K, G_L = membrane conductance per unit area for sodium, potassium and other ions – leakage conductance (S/cm^2), I_{Na}, I_K, I_L= electric current carried by sodium, potassium, and other ions (leakage current) per unit area (mA/cm^2), V_{Na}, V_K, V_L= Nernst voltage for sodium, potassium and other ions (leakage voltage) (mV), V_m = membrane voltage (mV).

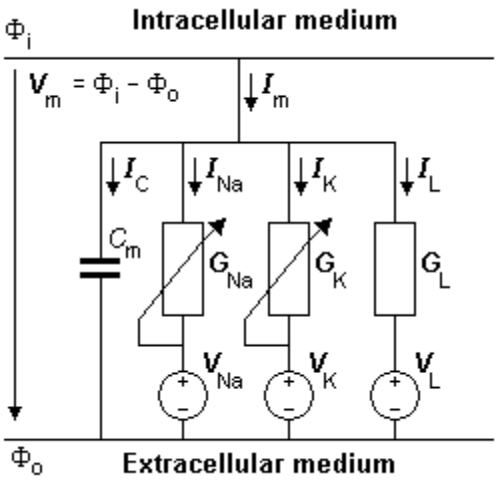

Figure 2.18: Equivalent circuit of the Hodgkin-Huxley model. Voltage sources are designated by Nernst voltage per ion species [41].

Membrane conductance for sodium and potassium are functions of transmembrane voltage and time. The leakage current, however, is constant. The total transmembrane current density is the sum of capacitive and ionic components, and is given as [41]

$$I_m = C_m \frac{dV_m}{dt} + (V_m - V_{Na})G_{Na} + (V_m - V_K)G_K + (V_m - V_L)G_L, \qquad [2.25]$$

where I_m = membrane current per unit area (mA/cm^2), C_m = membrane capacitance per unit area (F/cm^2), V_m = membrane voltage (mV), V_{Na}, V_K, V_L= Nernst voltage for sodium, potassium and leakage ions (mV), G_{Na}, G_K, G_L = Sodium, potassium and leakage conductance per unit area (S/cm^2).

The opening and closing of K^+ ion channels for the passage of K^+ ions across the cell membrane are controlled by electrically charged particles

called *n*-particles. These particles may stay in the open or closed position, and move between these states with first-order kinetics [41]. Transfer rate coefficients such as α_n and β_n describe the transfer rates for *n*-particles from closed to open state, and from open to closed state respectively. K^+ channel will be open only if four *n*-particles exist in the open state. Therefore, the probability of the channel being open is proportional to the joint probability of four *n*-particles being in the open state i.e. n^4. The rate of increase in the fraction of n-particles in the open state is given by [41]

$$\frac{dn}{dt} = \alpha_n(1-n) - \beta_n n, \qquad [2.26]$$

where n = fraction of *n*-particles in the open state, $(1-n)$ = fraction of *n*-particles in the closed state.

The potassium conductance is given by,

$$G_K = G_{K\,max}\, n^4 \qquad [2.27]$$

where $G_{K\,max}$ = maximum value of potassium conductance.

Similarly, for sodium channels *m*-particles are given by,

$$\frac{dm}{dt} = \alpha_m(1-m) - \beta_m m. \qquad [2.28]$$

For sodium channels, the fall in G_{Na} is due to inactivating particles such as *h*-particles given as,

$$\frac{dh}{dt} = \alpha_h(1-h) - \beta_h h. \qquad [2.29]$$

Therefore, sodium conductance governed by 3 *m*-particles and 1 *h*-particle is given by

$$G_{Na} = G_{Na\,max}\, m^3 h. \qquad [2.30]$$

2.2.13 Membrane conductance to electrical conductivity of neural tissue

The overall membrane conductance of neurons is determined by conductance of Na^+, K^+ and Cl^- ion channels as well as the passive parts of the membrane structure. At rest, neurons have relatively fewer ion channels in the open state leading to lower membrane conductance values. During neuronal depolarization, the membrane conductance of active neurons increases due to the opening of Na^+ and K^+ ion channels, as described by the Hodgkin-Huxley Model in **Section 2.2.12**. If low-frequency electrical currents are externally applied to neural tissue at rest, these currents would largely circulate in the extracellular space as shown in **Figure 2.19** [42, 43].

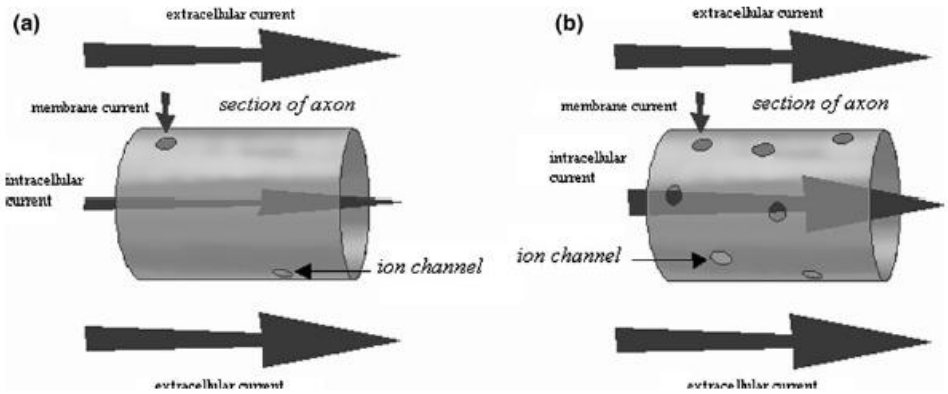

Figure 2.19: Flow of externally applied electrical currents through ion channels when a neuron is (a) at rest and (b) active [42].

During neural activity, the extracellular currents circulating around passive neurons now enter intracellular spaces of active neurons through the larger number of open ion channels [42]. These changes in current flow pathways lead to local apparent conductivity changes, thereby indicating the occurrence of neural activity [43]. Functional MREIT (fMREIT) measures small changes of apparent conductivity in voxels coincident with active neurons as MR phase changes [4], described in further detail in **Chapter 3**.

2.3 Electrical Conductivity of Biological Tissues

In the presence of electromagnetic fields, the degree and type of field interaction with biological materials depends on the electric and magnetic properties of the material. Dielectric, or electrical properties such as relative permittivity, and conductivity influence the interaction of native material with electric fields whereas magnetic permeability influences magnetic field interactions. However, most mammalian biological materials have magnetic permeabilities almost equal to free space ($\mu_o = 1.26 \times 10^{-6}\ H/m$) [44].

Dielectric properties such as relative permittivity and conductivity of biological tissues have been well-characterized in various *ex vivo* and *in vivo* tissue types over a range of frequencies [45-47]. Materials can be considered as either mostly insulating, and described in terms of permittivity, or mostly conducting and

described using conductivity parameters. Regardless of the description, the electrical conductivity or permittivity ($\boldsymbol{\sigma}$ or $\boldsymbol{\varepsilon}$) of a material are complex quantities. Complex conductivity ($\boldsymbol{\sigma}$) and complex permittivity ($\boldsymbol{\varepsilon}$) are expressed as

$\boldsymbol{\sigma} = \sigma' + i\sigma''$ and

$\boldsymbol{\varepsilon} = \varepsilon' - i\varepsilon''$, [2.31]

respectively, where $\varepsilon' = \varepsilon'_r\varepsilon_0$, $\varepsilon'' = \varepsilon''_r\varepsilon_0$, ε_0 is the permittivity of free space ($8.85\text{x}10^{-12}$ F/m), ε'_r and ε''_r are dimensionless relative parameters characteristic of the material. The real part of complex conductivity (S/m) is given as:

$\sigma' = \varepsilon''\omega$, [2.32]

where ω is the angular frequency (radians/second) of the field.

The dielectric properties of polar biological molecules depend on the frequency of the applied alternating electromagnetic field. As the frequency of the incident electromagnetic field increases, the relative permittivity of biological molecules decreases whereas the electrical conductivity increases as shown in **Figure 2.20**.

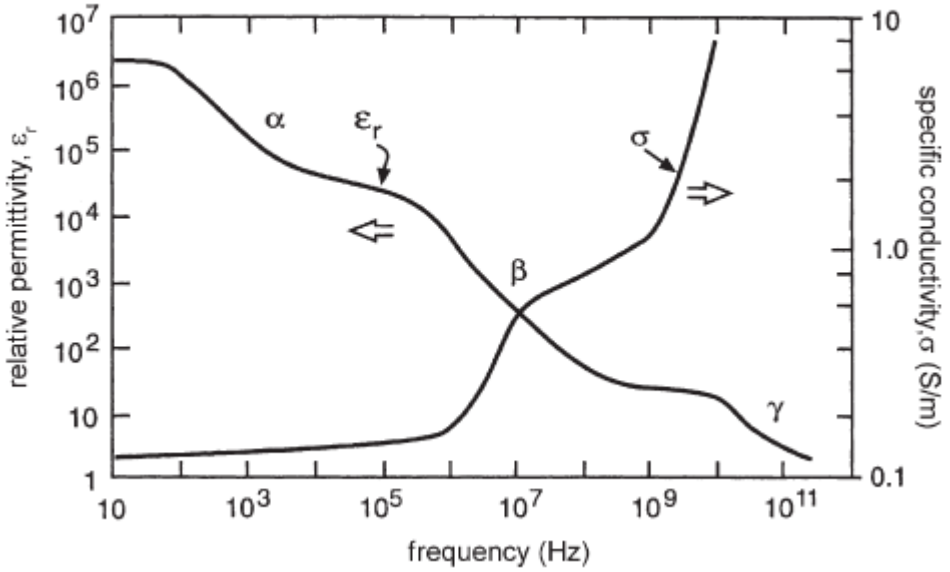

Figure 2.20: Frequency dependence of dielectric parameters (relative permittivity and conductivity) in biological tissues [48].

Relative permittivity has three distinct dispersion characteristics, namely α, β and γ. Low frequency α dispersion (1 Hz – 100 Hz) is due to ion transport across cell membranes. β and γ dispersions are related to the polarization of cell membranes and water molecules respectively. The electrical conductivity is highly dependent on the molecular composition, structure, concentration and mobility of ions, temperature, extra- and intra- cellular fluids and other factors associated with native biological materials. Conductivity is representative of the physiological and pathological state of tissue and hence, provides useful diagnostic information [49]. Tissues have finite ionic conductivities based on the nature and extent of their ionic content and ionic mobility. Tissues such as muscle and white matter exhibit anisotropic conductivity values at low frequency, as shown in **Table 2.1**.

However, conductivity imaging techniques such as Electrical Impedance Tomography (EIT) and Magnetic Resonance Electrical Impedance Tomography (MREIT) assume isotropic or equivalent isotropic conductivity distributions, as explained in **section 2.4** [49].

Tissue	**Electrical conductivity (S/m)**
Brain (gray matter)	$1x10^{-1}$
Brain (white matter, long.)	1.2
Brain (white matter, trans.)	$1.2x10^{-1}$
Bone (cortical)	$5.5x10^{-3}$
Bone (cancellous)	$21.4x10^{-3}$
Blood	$6.7x10^{-1}$
Skin (wet)	$4.3x10^{-1}$

Table 2.1: Electrical conductivity values measured at low frequency (< 1 kHz) [50].

2.4 Imaging Techniques for Conductivity Contrast Mapping

Conductivity contrast serves as a biomarker to provide critical information on disease states of passive tissues, and activity level of active tissues. Cross-sectional conductivity distributions of electrically conductive objects may be reconstructed by injecting electrical currents, and measuring the resulting boundary voltage, internal magnetic flux or current density values. Two widely used conductivity reconstruction techniques, namely electrical impedance tomography and magnetic resonance electrical impedance tomography, are described in detail in **section 2.4** and **Chapter 3**.

A. Electrical Impedance Tomography (EIT)

Electrical impedance tomography (EIT) reconstructs tomographic images of transfer impedance using surface electrical currents of 1 Hz – 1 MHz frequency injected through a pair of diametrically opposite electrodes for contemporaneous boundary voltage measurements at other electrodes [14]. Tomographic images of the electrical impedance is reconstructed using a sensitivity matrix, anisotropic finite element model of the subject and inverse mathematical methods [14]. The electrical impedance comprises of resistance and capacitance fluctuations during external current injections. The resistance changes due to ionic conduction in extracellular spaces whereas capacitance changes reflect current passage through interfaces that store charge, such as cell membranes. Theoretically, capacitance changes may provide useful information, however, stray capacitances in the electronics of the EIT system hinders the accurate measurement of tissue capacitances [51]. And therefore, capacitance measurements are discarded in EIT image reconstructions.

The objective of impedance imaging is to map cross-sectional conductivity distributions within an electrically conducting subject [43]. Internal current flow pathways establish internal current density, internal magnetic flux density and voltage distributions. Internal current flow depends on electrode configuration, conductivity distribution (σ) and geometry of the subject [49]. Under the assumption of fixed boundary geometry and electrode

configuration, the internal current density is determined by the conductivity distribution to be imaged [49]. A local change in the conductivity alters the internal current pathway, which is manifested as a change in boundary voltage and internal magnetic flux density[43]. Multi-frequency EIT (MFEIT) allows the measurement of impedance changes over a range of frequencies (1 kHz – 1 MHz), to allow for tissue characterization in single images [43].

Electrical Impedance Tomography (EIT) reconstructs conductivity images from measured boundary current-voltage data [43]. However, spatial resolution and accuracy of the reconstructed conductivity distribution in EIT is poor due to insufficient boundary voltage measurements. The relationship between internal conductivity distribution and boundary current-voltage data is highly non-linear. Owing to the non-linearity and insensitivity of boundary voltage measurements to the underlying conductivity distribution, the reconstruction of conductivity images is ill-posed [43]. Inaccurate modeling of boundary geometry and electrode positioning further complicates the inverse problem of conductivity reconstruction [43]. The use of a finite number of electrodes (usually 8 – 32) poses limitations on measured current – voltage, and contaminates the measured voltage data through measurement artifacts and noise [43].

Nevertheless, EIT is desirable in clinical applications because of its high temporal resolution, portability, fast, noninvasive and inexpensive bedside monitoring [51]. As of today, EIT is useful to track changes in conductivity

over time or frequency [49]. To transform the inverse problem in EIT into a well-posed one, the magnetic and electric fields induced in an electrically conducting subject following surface current injections were integrated, thereby generating interest in measuring internal magnetic fields as explained in **section 2.4(B)** [43].

B. Magnetic Resonance Electrical Impedance Tomography (MREIT)

Magnetic Resonance Electrical Impedance Tomography (MREIT) reconstructs cross-sectional conductivity distributions using external electrical currents synchronized with magnetic fields [52-54]. When an external electrical current *I* is injected into an electrically conducting object, an internal magnetic flux density $\boldsymbol{B} = (B_x, B_y, B_z)$, current density $\boldsymbol{J} = (J_x, J_y, J_z)$, and voltage distribution is established [27]. Using a magnetic resonance imaging (MRI) scanner with the main magnetic field ($\mathbf{B_0}$) in the *z*-direction, the *z*-component of the current-induced **B** is measured as B_z. The *x*- and *y*-components of **B** are measured by aligning the *x*- and *y*-axes of the object with $\mathbf{B_0}$ through object rotations [43]. The experimentally measured **B** would then be used in the Ampere's law to compute the established internal current density **J** as shown,

$$J = \nabla \times B / \mu_0, \qquad [2.33]$$

where μ_0 is the magnetic permeability of free space [43]. Conductivity distributions are further deduced from the reconstructed **B** and/or **J** images to understand the internal current pathways [43].

Challenges associated with the measurement of all three components of **B** in *in vitro* and *in vivo* biological samples as mentioned in **equation 2.33** hindered the progression of MREIT studies in preclinical and clinical contexts. Standard MRI scanners can only measure a single component of **B**, which is parallel to the main magnetic field ($\mathbf{B_0}$). The imaging object needed rotation about three orthogonal axes to measure all three components of **B**. Object rotations are not recommended in clinical settings because of pixel misalignment and inherent complications in rotating living subjects, and therefore posed a practical challenge for *in vivo* studies [43].

Recent conductivity reconstruction algorithms have focused on investigating the relationship between a single measured component of **B** and the established current density or underlying conductivity distribution. The Harmonic-B_z algorithm was proposed as a new method to reconstruct conductivity distributions using B_z in MREIT, without the need to measure B_x and B_y [55].

MREIT imaging currents are low frequency, and therefore the electrical conductivity of biological tissues at low frequency, such as 10 Hz, are the most relevant in MREIT imaging experiments. The low-frequency conductivity values of active and passive tissues determine the pathways of current flow and distributions of current density within biological tissues injected with MREIT imaging currents [56]. The low-frequency conductivity values of tissues found in the head are shown in **Table 2.1**.

External electrical currents are injected as electrical pulses in MREIT experiments [56]. A constant current source sequentially injects positive (I^+) and negative (I^-) currents through surface electrodes in synchrony with MR pulse sequences, as shown in **Figure 2.21**. The injected current induces a magnetic flux density $\mathbf{B} = (B_x, B_y, B_z)$ causing inhomogeneity in $\mathbf{B}_0$ changing **B** to ($\mathbf{B} + \mathbf{B_0}$). The magnetic field inhomogeneity leads to MR phase accumulation proportional to the *z*-component of **B** i.e. B_z, when the MR main magnetic field is in the *z*-direction. Electrical currents (I^+ and I^-) with the same amplitude and width are injected sequentially to remove systematic phase artifact of the MRI scanner, and to increase the phase change by a factor of 2 [56].

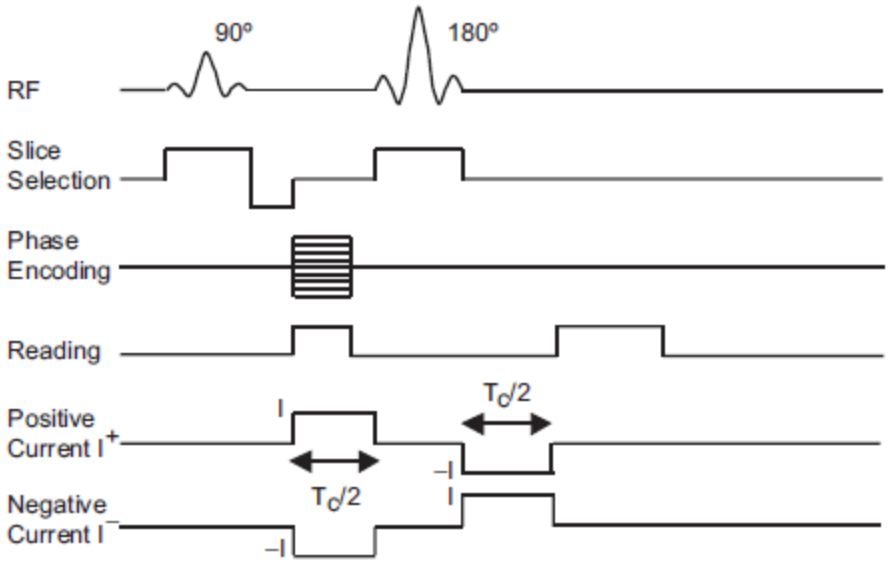

Figure 2.21: Standard spin echo pulse sequence for MREIT [56].

The MR spectrometer provides complex *k*-space data corresponding to positive (I^+) and negative (I^-) imaging currents as [56]

$$S^{I^{\pm}} = \iint_{-\infty}^{\infty} M(x,y)\, e^{j\delta(x,y)}\, e^{\pm j\gamma B_z(x,y)T_c}\, e^{j(xm\Delta k_x + yn\Delta k_y)} dx\, dy, \qquad [2.34]$$

where M is the MR magnitude image representing transverse magnetization, δ is any systematic phase error, $\gamma = 26.75 \times 10^7$ rad T^{-1} s^{-1} is the gyromagnetic ratio of hydrogen, T_c is the pulse width of the current in seconds. Two-dimensional discrete Fourier transformations of $S^{I^{\pm}}$ result in complex images $M_C^{\pm}(x,y)$ as shown [56]

$$M_C^{\pm} = M(x,y)e^{j\delta(x,y)}e^{\pm j\gamma B_z(x,y)T_c}. \qquad [2.35]$$

Incremental phase change is calculated by dividing the imaginary part of two complex images as [56]

$$Arg\left(\frac{M_c^+(x,y)}{M_c^-(x,y)}\right) = Arg\left(e^{j2\gamma B_z(x,y)T_c}\right) = 2\gamma B_z(x,y)T_c = \varphi_d(x,y), \qquad [2.36]$$

where Arg(w) denotes the argument of a complex number w. If the phase change φ_d is wrapped in $-\pi < \varphi_d < \pi$, a phase unwrapping algorithm such as Goldstein's branch cut algorithm may be useful [56].

Data quality in MREIT may be assessed using the noise in MR phase images by computing the standard deviation of phase (s_φ), standard deviation of phase difference (φ_d) and standard deviation of the Laplacian of phase difference images ($s_{\nabla^2\varphi_d}$) as [4, 31]:

$$s_\varphi = \frac{1}{\Upsilon_M},$$
$$s_{\varphi_d} = \frac{\sqrt{2}}{\Upsilon_M},$$
$$s_{\nabla^2\varphi_d} = \left(\frac{20}{\Delta x^4} + \frac{6}{\Delta z^4}\right) s_{\varphi_d}, \qquad [2.37]$$

where Υ_M = Signal to noise ratio (SNR) of magnitude image. To calculate the SNR of a magnitude image, a region of uniform intensity is chosen to compute the average value of all pixels within it. A region of the same size is chosen outside the object to compute the standard deviation. The ratio of the average signal to standard deviation in noise is multiplied by 0.655 for the SNR of the magnitude image [4, 31].

Phase difference images are scaled to produce B_z distributions of the internal magnetic flux density. B_z distributions induced during electrical current injection are crucial in determining the spatial resolution and accuracy of reconstructed conductivity images in MREIT [29]. B_z images are further processed with voltage distributions to reconstruct current density or conductivity distributions. *In vivo* MREIT experiments allowed conductivity reconstructions in canine brain [57] and imaging of both current flow and conductivity in human heads [28]. The spatial and temporal resolutions of conductivity reconstructions, and practical limitations of MREIT are compared with EIT in **Table 2.2**.

	Magnetic Resonance Electrical Impedance Tomography (MREIT)	**Electrical Impedance Tomography (EIT)**
Advantages	Better spatial resolution and accuracy	High temporal resolution
	Information from MREIT can be used as *a priori* information in EIT reconstructions for better results.	Portability
Disadvantages	Long imaging time	Poor spatial resolution
	Lack of portability	Inaccurate
	Requirement of an expensive MR scanner	Do not need MR scanner

Table 2.2: Comparison of the pros and cons of MREIT and EIT [43].

In conclusion, the passive and active behavior of neurons have been described with emphasis on the role of neuronal membrane conductance. The progression of membrane conductance in active neurons during the generation and propagation of action potentials was discussed in the context of conductivity mapping techniques – EIT and MREIT. Functional brain mapping using EIT and MREIT are explained in **Chapter 3**.

3. TECHNIQUES FOR FUNCTIONAL BRAIN MAPPING

Changes in electrochemical gradients, ionic currents, membrane conductance and membrane potentials generate electric and magnetic fields that may be used to map active neural sources. Mapping changes in membrane conductance, as in functional magnetic resonance electrical impedance tomography (fMREIT) and fast neural electrical impedance tomography (EIT), is a direct contrast mechanism underlying neural activity, and therefore may be classified as a *primary* method for detecting neural activity. Other examples of *primary* modalities involved in brain activity mapping are Electroencephalography (EEG) and magnetoencephalography (MEG). EEG records scalp potentials and MEG maps extracranial magnetic fields generated by internal neural sources. Methods such as functional magnetic resonance imaging (fMRI) that rely on mechanisms occurring secondary to neural activity such as hemodynamic changes through neurovascular coupling, may be classified as *secondary* methods of mapping brain activity.

3.1 Functional Magnetic Resonance Electrical Impedance Tomography (fMREIT)

Magnetic resonance electrical impedance tomography (MREIT) is sensitive to conductivity contrast of a medium through the application of external imaging currents synchronized to MR pulse sequences [56]. The use of MREIT-based phase measurements to detect changes in membrane conductance in active neural tissue is known as functional MREIT (fMREIT) [4]. At rest, the neuronal

membrane conductance is relatively constant. During neural activity, nerve impulses approaching a synapse trigger the release of synaptic vesicles into the synaptic clefts [58]. These vesicles fuse with a postsynaptic neuronal membrane and release neurotransmitters. These neurotransmitters cause membrane conductance changes in the postsynaptic membrane [58]. The increase in membrane conductance changes alters the pathways of externally applied MREIT imaging currents. External imaging currents generate a magnetic flux density. This magnetic flux density produces MR phase changes. In fMREIT, we attempt to capture activity-related membrane conductivity changes in MR phase images during external imaging currents [3].

Conductivity contrast in fMREIT is robust to cancellation effects due to neuronal and dipole orientation, polarity or presence of nearby activity [3]. Because conductivity is a positive and typically scalar quantity, fMREIT is advantageous over other direct methods of current flow based imaging because there is no loss of information due to conductivity cancellation or source orientation [3]. Furthermore, the magnitude of activity-related fMREIT phase signals should increase with externally applied imaging currents, and therefore may have an advantage over methods such as neuronal current(nc)-MRI [5].

A. Simulation studies

Finite element modeling of a well-studied neural complex, the *Aplysia* abdominal ganglion (AAG), placed in a saline-filled sample chamber was

investigated to establish the feasibility of MREIT to detect neural activity-related membrane conductivity changes [5]. A time-dependent, active, bidomain formulation of AAG neural tissue was used to estimate signal perturbations in fMREIT phase associated with spontaneous neural activity in the AAG neural complex [5]. Internal current source strengths of 500 pA, 1000 pA, 1500 pA or 2500 pA were used to model active AAG neural tissue [5]. External MREIT imaging current amplitudes of 1 mA, 2 mA or 5 mA were applied across diametrically opposite ports of the saline-filled sample chamber [5]. Model geometry with AAG tissue acting as "source" surrounded by saline solution with imaging current injection ports are shown in **Figure 3.1(a)**. The transient conductivity profile of active neural tissue is shown in **Figure 3.1(b)**. Imaging parameters from actual *in vitro* fMREIT experiments of AAG neural complexes were chosen to estimate signal sizes using 18.8 T field strength, and 70 × 70 × 500 μm^3/140 × 140 × 500 μm^3/280 × 280 × 500 μm^3 voxel sizes at 0.1 nT baseline noise level [5].

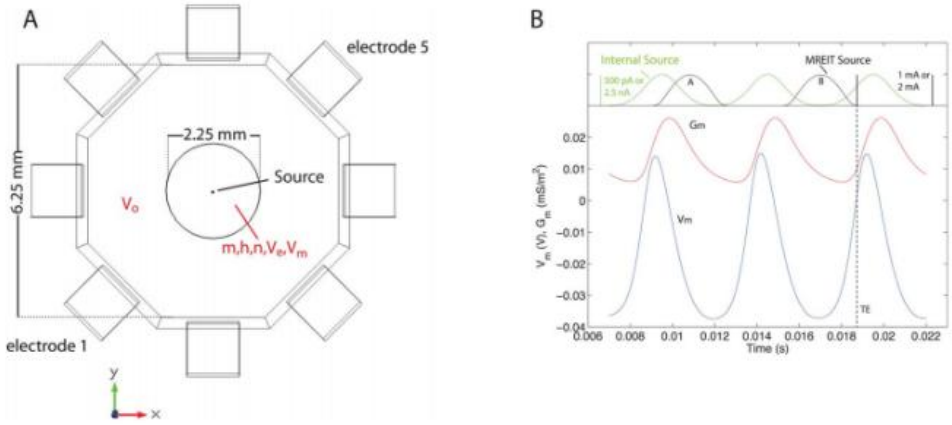

Figure 3.1: Active bidomain model of Aplysia abdominal ganglion (AAG). (A) Finite element model composition showing active AAG tissue as "source"

in a bath of saline solution. MREIT imaging currents injected between diametrically opposite electrodes – electrode 5 to electrode 1. (B) Waveforms showing MREIT imaging currents (black), internal current source (green), membrane conductance (red) and membrane voltage (V_m) at the center of the active tissue source [5].

fMREIT phase differences were found to depend on solely on activity-related membrane conductivity changes, rather than the strength of the internal current source [5]. At 1 mA imaging currents B_z signal changes (ΔB_z) showed minor increases from 0.12 nT to 0.14 nT as internal source strength increased from 500 pA to 2500 pA [5]. Imaging current amplitudes of 2 mA showed larger increases in ΔB_z from 0.27 nT at 500 pA internal source strength to 0.37 nT at 2500 pA [5]. Doubling imaging current amplitudes from 1 mA to 2 mA showed increases in the accumulated phase and B_z amplitudes due to MREIT-current induced membrane conductivity changes [5].

The influence of external imaging current size on fMREIT phase signals was assessed using 1 mA, 2 mA or 5 mA amplitude current [5]. The size of MR phase changes related to changes in membrane conductance of tissue scaled with imaging currents as the amplitude increased from 1 mA to 2 mA [5]. As imaging current amplitudes were increased to 5 mA, large non-linear increases in ΔB_z were suggestive of fMREIT signal changes caused by membrane conductivity changes rather than intrinsic current flow effects [5]. Complex interactions between internal source and imaging current amplitudes may lead to depolarizing tissue outside of the “source” as shown in **Figure**

3.1. Typical imaging current amplitudes of 2 mA resulted in current densities (40 A/m^2) at tissue periphery large enough to cause spiking activity and activity modulation, and therefore stimulate myelinated neurons [5]. Imaging geometry was noted to influence current densities, and therefore lead to neural stimulation during fMREIT experiments [5]. Imaging current associated neural stimulation effects must be taken into consideration when designing fMREIT experiments. Conversely, fMREIT is innately well-positioned to investigate neuromodulatory mechanisms underlying electrical stimulation therapies such as deep brain stimulation [5].

The ΔB_z signal sizes reported using a time-dependent and active model [5] was closer to actual *in vitro* fMREIT experiments compared to earlier passive bidomain modeling of AAG tissue [3]. The larger current amplitudes (1 mA – 5 mA) and time-varying conductivity profile used in the active model [5] resulted in 40× larger ΔB_z signal sizes compared to the passive model with 90 μA imaging current and constant membrane conductivity (active = 320 S/m^2, rest = 6.7 S/m^2) [3]. In conclusion, the feasibility of fMREIT to detect neural activity using membrane conductivity contrast using 1 mA imaging current amplitude at moderate resolutions was illustrated in FEM studies of realistic *in vitro* fMREIT studies [5].

Observation of small fMREIT phase signal perturbations due to activity-related membrane conductivity changes requires minimal noise in phase signals. Noise standard deviations in phase, as described in **section 2.4(B)**, determines the fMREIT signal quality level, and depends on voxel size, main magnetic field strength, overall system noise level, current injection time and number of excitations [31]. If activity occurs during T_C, there will be a difference between active and resting state phase images because results of activity-related membrane conductance changes will be integrated over this period [3]. Total measured phase change directly follows integrated conductance change [3]. SNR in phase is largely influenced by the expected differential level of activity between two sampling periods [3]. Overall, SNR in phase may be summarized as directly proportional to several factors as shown [3]:

$$SNR \propto (f_A - f_R)\, V_f \kappa (G_A - G_R) T_C, \qquad [3.1]$$

where f_A and f_R are the *active* and 'resting' spike rates,

V_f is the fraction of active tissue within a voxel,

κ is the shape factor that describes the integrated conductance profile of a single spike,

G_A and G_R are *active* and 'resting' membrane conductance over a single spike,

T_C is the imaging current injection duration.

To amplify fMREIT signal levels, imaging current waveforms (current amplitude and duration), current density distributions and MR pulse sequences must be carefully designed [3]. Furthermore, expected spike rate and fraction of active cells must be taken into consideration. The maximum current amplitude depends on the activity threshold and dynamic characteristics of the imaging current [3]. B_z signal changes scales with the amplitude of MREIT imaging current, and therefore stimulation effects must be taken into consideration [5]. At lower field strengths, use larger voxels to reduce noise in phase images and improve temporal resolution [3]. Reduced noise levels, or parallel data acquisition techniques may be useful in situations where long imaging times is not possible [3].

B. *In vitro* experimental studies

Tests were performed *in vitro* to confirm the studies described above were performed using AAG neural aggregates placed in a cylindrical sample chamber containing artificial sea water (ASW) at 11.8 T using voxel size 70 × 70 × 500 μm^3 [4]. Neural activity was modulated by injecting potassium chloride (KCl) solution into the sample chamber containing the neural tissue complex in ASW [4]. MREIT phase data was recorded under three tissue conditions, namely, PRE – spontaneously spiking neural tissue, POST – increased neural activity after the injection of KCl-doped sea water, and DEAD – 19 hours after imaging [4]. KCl solution was used to increase spike

rates to generate a conductivity contrast, wherein the conductivity of ASW and KCl-doped solution was 5.8 S/m and 6.6 S/m respectively [4].

Voxels coincident with active Aplysia tissue showed significant increases in MR phase changes after the injection of KCl-doped solution [4]. Using 100 μA and 1 mA imaging currents, MR phase signals showed non-linear increases with current amplitude from PRE to POST conditions [4]. However, MR phase signal differences was larger with 1 mA compared to 100 μA imaging currents [4]. Control solutions (ASW), resulted in significant decreases of MR phase possibly due to increase in the volume of the background solution [4]. Volume increases led to reduction in current density of the medium, and therefore, decreased the overall phase or B_z signal size from PRE to POST conditions [4]. Overall, MREIT imaging currents of 1 mA showed fMREIT phase signal changes at $70 \times 70 \times 500$ μm^3 in potassium-induced increased AAG activity relative to matched controls [4].

Additional *in vitro* experiments were performed at ultrahigh field strengths of 18.8 T using a similar experimental setup and imaging paradigm [6]. The KCl solution concentration was adapted to inhibit neural activity of AAG by injecting 50 μl KCl solution into the sample chamber containing ASW [6]. The extracellular K^+ concentration was increased to 89 mM to inhibit neural activity in the POST phase of the experiment [6]. Conventional SE-MREIT

pulse sequences were used with 1 mA surface current injections for 16 ms [6]. Initial testing of these experiments at 18.8 T revealed MR phase distortions potentially due to Lorentz forces acting on sample contents [6]. These magnetohydrodynamic (MHD) effects during imaging current injections were overcome by increasing the viscosity of the background solution[6]. ASW in the sample chamber was infused with 0.2 g methylcellulose powder to increase the viscosity of background solution [6].

In these studies, it was found that statistical measures in background ROIs were consistently smaller than AAG tissue compartments in phase and Laplacian phase analysis [6]. Statistical measures of phase in tissue ROIs were significantly different, however, the KCl group showed higher standard deviations compared to ASW, which contradicted the expected decrease in neural activity at KCl concentrations of 89 mM [6]. Cell shrinkage due to KCl may have complicated the relationship between membrane conductivity and neural activity [6]. Significant differences were found in differential Laplacian phase images in active tissue compartments, however, such differences were not observed in background compartments [6]. Laplacian of phase showed regions of rapid phase change, thereby explaining significant differences in tissue compartments as being due to neural activity that are absent in background compartments [6].

C. *In vivo* experiments

To aid the clinical translation of fMREIT as a viable conductivity imaging technique, *in vivo* preclinical studies must be conducted at lower magnetic field strengths. Complex physiological mechanisms occurring in the immediate vicinity of active neural tissue in whole and living organisms (e.g. live rats) may influence fMREIT phase signals that were not accounted for in simulation or *in vitro* studies. Non-neuronal physiological mechanisms such as vascular changes, respiratory and cardiac cycles may appear as physiological noise in fMREIT phase measurements. Vascular mechanisms altering the amount and flow of blood in the vicinity of active neural tissue may arise from neural activity or metabolic processes. Due to the high conductivity of blood (σ = 0.7 S/m), changes in cerebral blood flow may also confound and obscure small activity-related perturbations in fMREIT phase signals. Strategies to minimize contributions from blood flow to fMREIT signals are needed to accurately measure conductivity changes related to neural activity. In addition, careful design of fMREIT imaging current parameters and waveforms is needed to avoid the unintended stimulation of neurons by imaging currents.

3.2 Fast Neural Electrical Impedance Tomography

Electrical Impedance Tomography (EIT) has recently been adapted for imaging electrical impedance changes in the brain during stroke, epilepsy and normal

brain function [51]. EIT has the potential to directly measure fast neural activity over milliseconds covering the whole brain, using non-invasive surface electrodes [14]. Electrical currents of 1 Hz – 1 MHz frequency are injected using a pair of electrodes, and boundary voltage measurements are made at remaining passive electrodes to reconstruct impedance images using anisotropic finite element models of the subject and inverse mathematical formulations, as described in further detail in **Section 2.4(A)** [15, 51].

Brain impedance changes occur over two distinct timescales –seconds ("slow") and milliseconds ("fast") [51]. During ischemia or energy supply failure, slow impedance changes arise from the movement of water from extracellular spaces into cells, and thereby increasing brain impedance [51]. Neuronal depolarization, on the other hand, decreases bulk resistance of the brain due to the opening of ion channels over several milliseconds [51]. In the absence of neural activity, low-frequency current travels in the extracellular space, and only penetrates cell membranes when ion channels open, resulting in an impedance decrease [42]. Penetration of electrical currents across the cell membrane is frequency-dependent. When direct current (DC) is applied, impedance changes are about 1%, and reduce to 0.01% at 10 kHz [42]. Furthermore, regional cerebral blood flow to active brain regions decreases local impedance as blood has lower impedance than the brain [59].

Finite element modeling studies of the human head demonstrated brain impedance contrasts of 100% corresponded to scalp voltage changes of 7% against noise levels of 0.2% in acute stroke; 10% impedance changes related to 0.3 – 1% voltage changes on the scalp with 0.1% noise in epilepsy; and 1% impedance changes due to brain function resulted in 0.005% scalp changes, which is at the limit of detection [51]. The first human EIT brain function study was conducted using a ring of non-invasive EEG-like electrodes (16 – 64 electrodes) placed around the head to inject electrical currents of 1 – 2.5 mA amplitude over 50 kHz frequency using diametrically opposite electrodes [15]. Significant impedance changes above baseline noise levels were noted, however, these local impedance changes were inconsistent with brain regions expected to be active with stimulation paradigms [15, 16].

In vivo EIT studies were undertaken with invasive electrode arrays to image cortical neural activity in anesthetized rats [14]. Epicortical electrode arrays comprising of 30 electrodes were placed over the primary somatosensory cortex (S1) to inject electrical currents within a pair of electrodes and record voltage measurements at remaining electrode tips [14]. Mechanical stimulation of two whisker groups performed separately induced evoked responses. Tomographic images of impedance changes revealed somatotopically separate activity for stimulation of the two whisker groups [14]. Largest lateral spreads of impedance changes were found at layer II/III at predominantly barrel rows [14]. These

findings demonstrated the feasibility of EIT to image neural activity with high temporal (2 ms) and spatial (< 200 μm) resolution over large volumes, as shown in **Figure 3.2** [14].

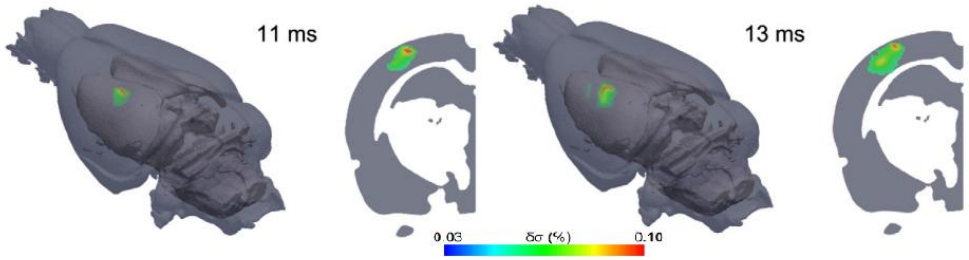

Figure 3.2: EIT images of impedance changes during mechanical stimulation of whiskers. Conductivity changes are shown with a color bar ranging within (0.03, 0.10). Changes in conductivity in the primary somatosensory region (S1) increase from 11 ms to 13 ms shows neuronal activity on the timescale of milliseconds [14].

Fast neural EIT and fMREIT are both conductivity imaging techniques that were adapted to detect neural activity. A brief comparison of both these techniques are summarized in **Table 3.1**.

fMREIT	Fast Neural EIT
Low temporal resolution limited by MRI sequence imaging parameters (~ 1 s).	High temporal resolution (~ 1 ms).
High spatial resolution (~ 70 μm).	Lower spatial resolution using non-invasive electrodes.
Can measure phase signals throughout the brain.	Cannot measure impedance changes from deep brain structures.
Non-invasive electrodes placed on the surface is sufficient to locate active neuronal sources.	Neuronal source localization needs invasive procedures to implant electrodes.
Electrode pairs (2 - 4 electrodes) needed for current injection purposes.	Electrode arrays (8 - 32 electrodes) needed for current injection and boundary voltage measurement.

Table 3.1: Comparison of the advantages and disadvantages of fMREIT and fast neural EIT.

3.3 Electroencephalography (EEG) and Magnetoencephalography (MEG)

In EEG, scalp potentials generated by electrical activity in the brain are measured, whereas, extracranial magnetic fields generated by similar mechanisms are measured in MEG [1]. Source estimation, also known as inverse modeling, is the reconstruction of the spatiotemporal patterns of neural activity based on the measured scalp potentials [1]. Source estimation comprises of two specific goals – source localization and spatiotemporal imaging [1]. Source localization is the process of locating the sources of measured signals as a function of time. Spatiotemporal imaging is the disentanglement of contributions from sources originating from different regions in the brain [1]. **Figure 3.3** shows the signals and source estimates resulting from EEG/MEG source estimation [1].

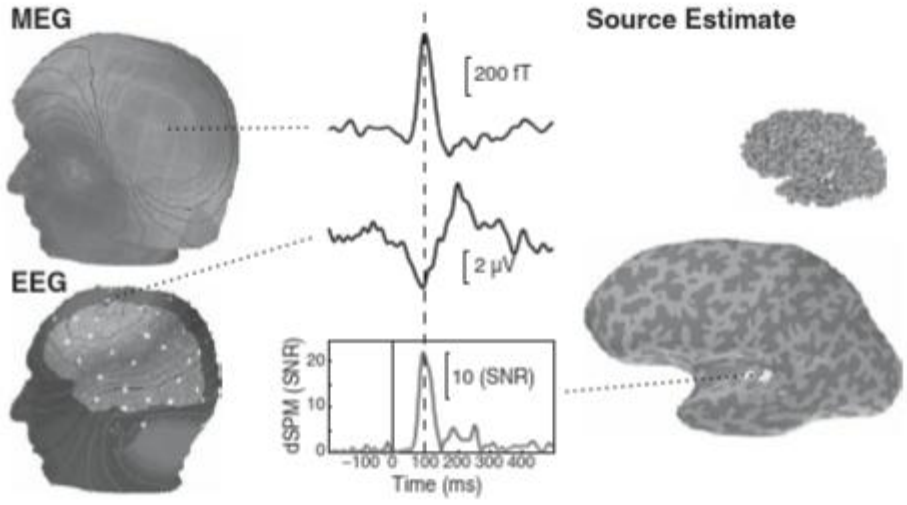

Figure 3.3: EEG and MEG signals, and source estimates. Left: Maps of event-related magnetic fields (top) and electric scalp potentials (bottom) shown with MRI reconstructions of the head [1].

Spatial patterns of scalp potential and extracranial magnetic signals generated by sources are specific to the type of source. These patterns may be calculated using a forward model. A forward model using the approximations of the conductor geometry (shape and tissue conductivities) and sensor configurations (engineering design, calibration) provides a solution to the Maxwell equations for current sources located in the brain [1]. While the accuracy of forward modeling depends on the physical and physiological approximations of the head and electrodes, the inverse modeling in EEG/MEG uses estimation theory, *a priori* assumptions and statistics [1]. For example, using a Bayesian approach, the inverse problem may be formulated as determining the posterior probability density of brain activation patterns, given the combination of the measured signals and *a priori* knowledge about the system [1]. **Figure 3.4** illustrates the analysis of EEG/MEG data for the reconstruction of active neural sources.

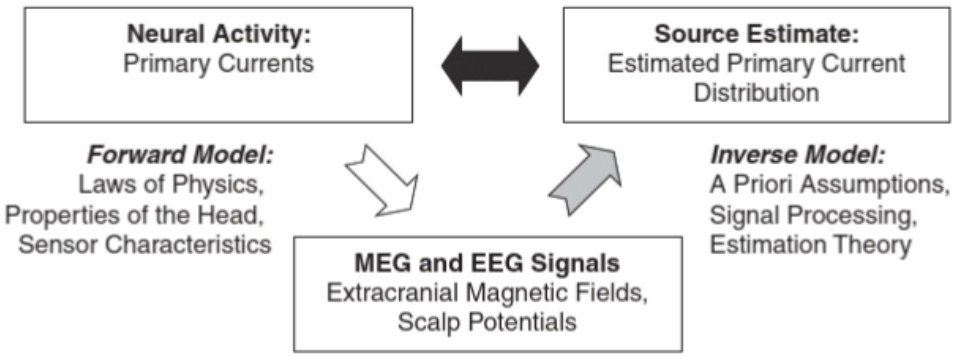

Figure 3.4: Relationship between neural activity and EEG/MEG source estimates [1].

EEG/MEG source currents depend on the global pattern of primary currents, unlike functional MRI (fMRI) as described below in **Section 3.4**, where signals are obtained for each voxel and is independent of signals from other voxels [1]. Using point-spread functions for local source elements, the accuracy of source localization was reported as 8 mm in MEG and 10 mm in EEG in the human brain [1]. Unlike other brain imaging techniques, EEG and MEG allow non-invasive mapping of electrical activity in the human brain with millisecond time resolution [1]. Hemodynamic methods such as fMRI do not have the same time resolution as EEG and MEG, and furthermore are only indirect measures of neural activity.

3.4 Functional Magnetic Resonance Imaging (fMRI)

fMRI is widely used as a non-invasive functional brain imaging technique that relies on proxy measures of neural activity such as local blood flow, oxygenation and metabolism to identify active brain areas [18]. Blood oxygen level dependent (BOLD) contrast imaging is the most common fMRI method that uses hemoglobin as an endogenous contrast agent [18]. BOLD-fMRI signals are generated by magnetic (T2*) property differences between oxyhemoglobin (diamagnetic) and deoxyheomoglobin (paramagnetic) [17]. In particular, BOLD-fMRI measurements are sensitive to local concentrations of paramagnetic deoxyhemoglobin (HbR). The BOLD signal decreases with local increases in HbR, and these BOLD-fMRI signal decreases are mapped as functional activity in the brain [18].

Neuronal action potentials lead to the release of neurotransmitters in the synaptic cleft such as glutamate and changes in ionic gradients in the postsynaptic membrane [17]. Continuous neural activity needs energy, which is provided by glucose and oxygen through cerebral blood flow [17]. Under normal resting conditions, the energy demands of neurons in the passive state are met by glucose oxidation. Glucose consumption in the resting state is oxidative, and the energy yield of glucose oxidation is large enough to support 99% of ATP production [17]. Under functional activation, the cerebral metabolic rate for glucose and cerebral blood flow increases by ~50%, whereas the cerebral metabolic rate for oxygen increased only by 5%. With about 90% of activity-induced glucose uptake not being metabolized, an alternative pathway for glucose metabolism known as glycolysis is initiated that yields lactate [17]. As the cerebral blood flow exceeds cerebral metabolic rate for O_2, a highly significant reduction in oxygen extraction fraction occurs. The decrease in oxygen consumption presents as over-oxygenation of the region surrounding active neural tissue, thereby representing a decrease in HbR [17].

Neurovascular coupling is the relationship between neural activity and associated increases in local blood flow [17]. Classical fMRI assumes neurovascular coupling is robust irrespective of brain regions, brain development or pathological state, i.e. any increase in neuronal activity will generate a proportional increase in

local blood flow [18]. Therefore, BOLD signals measure the hemodynamic response as a correlate of neural activity [17].

Classic positive BOLD signals under evoked functional stimulation correspond to local increases in blood flow and blood volume to active neural tissue to increase local oxygenation levels [18]. The hemodynamic response depends on cerebral oxygenation, blood flow and blood volume. The hemodynamic response starts within ~500 ms and reaches maximum at 3-5 s after onset of the stimulus [18]. The appropriateness of fMRI functional brain maps depends on the characterization of underlying neural activity, the immediate microvasculature and other factors that modulate the BOLD signal [17].

Carbogen, a mixture of 95% O_2 and 5% CO_2, has frequently been administered as a gaseous inhalant to induce vasodilation and venous saturation [60]. The vasodilatory effect of CO_2 is further enhanced by the high O_2 content dissolved in blood during carbogen inhalation [60]. Carbogen increases cerebral blood flow that leads to excess venous blood oxygenation levels. Blood O_2 saturation increases correspond to deoxygenated hemoglobin decreases in brain tissues [60], thereby creating a limit on oxygenation increases and diminishing the activated BOLD signal [61]. Switching gaseous inhalant mixtures from air to carbogen requires produces rapid and reversible effects on cerebral vessel caliber and blood

flow with minimal side effects, whereas pharmacological alternatives to carbogen such as acetazolamide, produces long-lasting effects on cerebral tissues [62].

In vivo fMRI studies on anesthetized rats undergoing forepaw stimulation during inhalant delivery ranging from normal air to carbogen were used as the basis to design *in vivo* fMREIT studies [61]. BOLD signal magnitudes and spatial extents were found to decrease under carbogen compared to air delivered as an inhalant [61]. Functional imaging paradigm described in **Chapter 6** is based on the passage of carbogen to suppress BOLD signals and saturate vascular signals that could potentially interfere with fMREIT phase signals from active neural tissue.

4. DEVELOPMENT OF CARBON ELECTRODES FOR fMREIT-CURRENT DELIVERY IN NEURAL TISSUE

The *in vivo* mapping of neural activity in a whole intact organism necessitates imaging at lower field strengths, for instance 7 T MRI fields, rather than previous *in vitro* fMREIT experiments conducted at 11.8 T or 18.8 T field strengths. SNR decreases linearly with main magnetic field strength, and therefore the noise floor of 7 T MR system is expected to exceed those of 11.8 T or 18.8 T. Neural activity-related membrane conductance changes produce small fMREIT phase signal perturbations under externally applied imaging currents. To increase phase signal sizes above the noise floor, imaging currents need to be delivered directly into the brain to avoid electrical current losses due to low conducting skull. Platinum-iridium (Pt-Ir) is conventionally used for neural stimulation, however, Pt-Ir causes local noise due to signal dropout in MR images. Carbon electrodes were developed as alternatives to Pt-Ir for use in fMREIT imaging current delivery. In clinical contexts, Pt-Ir is extensively used in neuromodulatory treatments such as Deep Brain Stimulation (DBS) to deliver electrical impulses for the treatment of neurological disorders such as Parkinson's Disease. The chapter describes the development, characterization and testing of carbon electrodes in comparison to Pt-Ir electrodes in DBS contexts.

4.1 Introduction

Typical DBS electrodes are composed of platinum-iridium (Pt-Ir) alloy, which has high magnetic susceptibility compared to surrounding tissues. Susceptibility differences between implanted metal objects and tissues can cause local magnetic field inhomogeneities and artifacts such as geometric distortion, fat suppression failure, signal loss and pile-up artifacts in MR images [63-66]. Susceptibility artifacts scale with main magnetic field strengths and may obscure exact electrode boundaries on MR magnitude images [67]. Safety issues caused by heating of metal objects, due to RF or gradient field switching, is a major limitation in imaging [68]. Heating effects tend to be greater in long thin objects, such as leadwires or electrodes [69-71]. Ongoing efforts to mitigate RF-induced heating include introducing RF chokes [72], modifying lead design [73], coiling wires [74], or designing new leads based on resistive tapered stripline technology [75]. Despite these efforts, *in vitro* studies demonstrate risks of irreversible tissue damage due to DBS electrode heating [76, 77] at 1.5T, even as field strengths of 3T and above are becoming standard [78] for brain and spine studies. Higher magnetic fields, coupled with higher gradients, accelerated imaging sequences and gradient slew rates could potentially worsen DBS-electrode susceptibility artifacts and tissue heating, necessitating a search for an MR-compatible alternative to metal implanted neuromodulation electrodes.

Carbon electrodes and leadwires have previously been used in ECG [79], fMRI [80], simultaneous EEG-MRI [81] and EEG-fMRI [82] studies to overcome the challenges of using metals in a magnetic field. Carbon-fiber electrodes have been successfully used for stimulation of epilepsy and subsequent fMRI studies [80]. Carbon fiber nanotube yarns have also been tested as potential DBS implants, with the smaller susceptibility differences between carbon and surrounding tissues being found to reduce MR artifacts on T1- and T2- images compared to Pt-Ir electrodes [83, 84].

DBS surgery involves the uni- or bilateral implantation of DBS leads (e.g. Medtronic DBS 3387/3389 kit, Medtronic, Minnesota, USA) for the delivery of current pulses to target structures [85]. A single DBS lead is composed of insulated Pt-Ir conductor wires and four Pt-Ir electrodes [85]. DBS electrodes are commonly positioned at locations in the basal ganglia including ventral intermedius nucleus of the thalamus, subthalamic nucleus or internal globus pallidus [86, 87]. Current injected through a single Pt-Ir electrode (‘source’) may return to a pulse generator (‘sink’) typically implanted in the subcutaneous pectoral area [85]. DBS pulses are tuned to individual patients, with stimuli typically delivered as short (60–200-μsec pulse width) electrical pulses of 1-5 V amplitude, and 120 -180 Hz frequency [85, 86]. However, the mechanism underlying DBS is poorly understood [88]. While extensive modeling of DBS

fields and effect extent have been performed [89, 90] experimental determinations of DBS fields have not yet been performed.

MR magnetic flux and electrical current density imaging may be useful in the measurement of effects caused by DBS current flow. Recently, Magnetic Resonance Electrical Impedance Tomography (MREIT) has been used to reconstruct *in vivo* conductivity, current density and electric field distributions using measurements of a single component of magnetic flux density (B_z), caused by the current administration, that is parallel to the main MRI field [56, 91, 92]. Practical implementation of MREIT with clinically approved DBS systems would require no additional hardware. Measurements of electric field distributions caused by DBS stimulation nearby and throughout target structures may provide novel insights into the neuromodulatory mechanisms underlying DBS.

The novelty of this work lies in the development and testing of custom DBS-style carbon electrodes for MR magnetic flux and electrical current density mapping using MREIT. Carbon electrode performance is compared to diameter-matched Pt-Ir and clinical DBS electrodes at 7 T in terms of MR magnitude, phase and thermal properties, using uniform gel phantoms and anisotropic brain tissue samples. Impedance properties of carbon electrodes are also compared with DBS electrodes. It is anticipated that current density, electric field and conductivity imaging near carbon DBS electrodes may aid in the detailed investigation of DBS

mechanisms, as well as facilitating conductivity based direct functional imaging [3, 4].

4.2 Materials and Methods

4.2.1 Electrodes

Electrodes constructed using carbon or Pt-Ir were compared in the study. Electrode types and compositions are described in the sections below. Details of the protocol used to construct carbon electrodes are described in the **Appendix C** (**Section 1.1, Figure C1.1**).

A. One-contact (1C) carbon electrodes

Bundles of conductive carbon fibers (TC-33 3K, Formosa Plastics Group, Taiwan) were insulated using a three-stage dip-coating process: Nafion insulation, followed by immersion in two increasing concentrations of polyvinylene fluoride (PVDF) in acetone. Fabrication stages of 250- and 500-µm one-contact (1C) carbon electrodes are shown in **Figure 4.1(a)** and **Table C1.1**. These diameters were chosen to produce electrodes of similar diameters to conventional DBS electrodes. The concentration and viscosity of PVDF solutions was increased from stage II to stage III of electrode fabrication, to protect Nafion-coated electrodes from buckling during

immersion. Higher PVDF concentrations can be used with larger-diameter electrodes.

Before use, carbon electrodes were inspected under an optical microscope (Discovery V8 Stereo, Carl Zeiss Microimaging GmbH, Thuringia, Germany) to confirm electrode diameter, and check for cracks in insulation, stray carbon fibers and other obvious defects. The electrode insulation quality was electrically validated using two-terminal measurements of their electrical impedance in saline solution. Electrical validation and characterization tests used are detailed in **Appendix C** (**Section 1.3, Figure C1.2**). Impedance values were recorded as electrode depth in saline solution was increased in 3-5 mm increments. If the impedance at any depth deviated from 10% of the impedance measured with only the electrode tip immersed, electrode insulation was considered to be inadequate. The typical *closed-tip* impedance of 1C carbon electrodes (500-μm diameter) measured by the two-terminal test was around 100 kΩ at 1 kHz. Only electrodes with closed-tip impedance values >100 kΩ at 1 kHz were used in experiments.

Ends of 1C electrodes were exposed by cutting the end with scissors to construct either straight or beveled tip types. The insulative quality of

open-tipped electrodes was validated using the methods described above. A 45^{o}-beveled *open-tip* 1C carbon electrode with diameter 500-μm, similar to that shown in **Figure 4.1(b)**, had an impedance of around 100 Ω at 1 kHz.

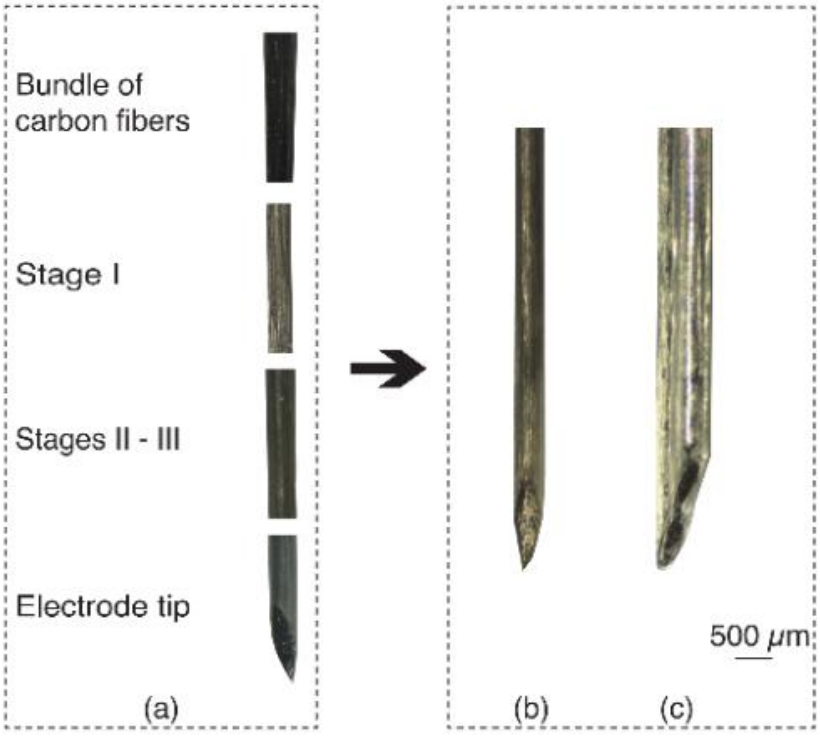

Figure 4.1: Carbon electrodes. (a) Fabrication stages of carbon electrodes (b) One-contact (1C, 500-μm diameter) and (c) Two-contact (2C, dimensions 1000 × 500 μm^2) carbon electrodes.

B. Two-contact (2C) carbon electrodes

Two-contact (2C) carbon electrodes were constructed by combining an offset pair of 1C (500-μm diameter) carbon electrodes. The 2C electrode fabrication process is described in **Appendix C** (**Section 1.2,**

Figure C1.1). The insulative quality of 2C carbon electrodes was measured using methods described in S**ection A** above.

Electrode contacts were exposed by cutting a bevel through both electrodes. In the tests described in 2.2 below, both conductive sites were combined (shorted) for electrical current delivery to approximate DBS electrode areas. A beveled open-tip 2C carbon electrode with an approximate cross-sectional area of $1000 \times 500\ \mu m^2$ is shown in **Figure 4.1(c)**.

C. Metallic electrodes (Pt-Ir wire) electrodes

Insulated Pt-Ir wire (203-μm diameter; A-M Systems, WA, USA) was compared with diameter-matched 1C carbon electrodes (250-μm diameter).

D. Deep Brain Stimulation (Pt-Ir)

A cylindrical quadripolar DBS lead (1.27-mm diameter Brain Neurostimulation Lead 3389, Medtronic Inc, Minnesota, USA) with four Pt-Ir ring electrodes was compared to 2C ($1000 \times 500\ \mu m^2$ cross-sectional area) carbon electrodes. While it was not possible to measure the connector-to-electrode tip resistance directly for carbon electrodes, it was possible for the DBS lead. The lead resistance (connector-to-

electrode resistance) was measured to be 41.5 Ω at 1 kHz. However, the resistance of the DBS lead using the two-terminal method described in **Appendix C** (**Section 1.3, Figure C1.2**) was 42.4 Ω at 1 kHz. This two-terminal measurement was used as the reference resistance for DBS leads.

4.2.2 Samples

MRI and MREIT experiments were conducted using carbon or Pt-Ir electrodes placed in gel phantoms or fixed tissue samples.

A. Gel phantoms

Cylindrical gel phantoms shown in samples 1-3 **(Figure 4.2(a-c))** were prepared by combining 20 g Agar, 3 g NaCl, 0.5 g $CuSO_4$ and 1000 ml distilled water. The mixture was microwaved until air bubbles rose towards the top layer of the solution. The solution was allowed to cool at room temperature into a solid gel within a cubic chamber of side 5 cm. Two opposing inner surfaces of the cube were covered with copper plates. The two-terminal resistance (R) between the plates at 100 Hz was measured using a low-frequency impedance analyzer (HP4192A, Hewlett Packard, Palo Alto, CA). The gel conductivity (σ) was then calculated using

$$\sigma = \frac{L}{RA}, \qquad [4.1]$$

where L is the electrode separation (m) and A is the electrode cross-sectional surface area (m^2). The area of the electrodes was assumed large enough that electrode impedances were negligible compared to gel resistances. Gel conductivity was calculated to be approximately 1 S/m at 100 Hz.

B. Phantom configuration

In experiments using Samples 1-2 (diameter 55 mm, height 42 mm) diameter-matched DBS 3389/2C or Pt-Ir/1C ('source') electrodes were placed within the phantom and surface carbon ('ground') electrodes were placed on the phantom periphery. Current pulses (amplitude: 1 mA, total current duration: 20 ms, frequency: 4 Hz) were passed between source and ground electrodes. In Samples 1-3, care was taken to align Pt-Ir and carbon electrodes along the $\mathbf{B_0}$ (i.e. z-axis) during current injection to minimize stray field contributions from active electrodes.

In experiments using Sample 3, sinusoidal RF signals (amplitude = 0.13 mW, frequency = 298 MHz) amplified using a RF power amplifier (gain = 30 dBm) were transmitted into the sample via a custom-made RF surface coil that covered the upper half of the phantom. A maximum power (amplitude = 10 mW, SAR $\leq$ 0.15 W/kg) was deposited in the center of the phantom. The field geometry was

symmetric, and each electrode type was subject to similar B_1 field patterns. Fiber optic sensors (TS3, Optocon, Germany) were secured to DBS 3389/2C electrodes to measure temperatures at electrode tips. A third "central" sensor was placed equidistant from both electrodes, in the center of the phantom. Temperature sensors were connected to a temperature signal conditioner (FOTEMP-OEM-PLUS, Optocon, Germany) and temperatures at each sensor were recorded every 2 seconds over 30 minutes' continuous RF application. More details of benchtop temperature experiments are provided in **Appendix C (Section 2, Figure C1.3)**.

C. Paraformaldehyde-fixed rodent brain

A 250 g Wistar rat was euthanized by transcardial perfusion with saline [93] containing Heparin (1 unit/ml) and 4% Paraformaldehyde in 0.1 M Phosphate Buffer prior to surgery following an Arizona State University Institutional Animal Care and Use Committee-approved protocol. A 1C carbon electrode (250-μm diameter) and an insulated Pt-Ir wire (203-μm diameter) was implanted at a posterior inclination of 50^o into the left and right hippocampus respectively (Sample 4, **Figure 4.2(d)**). The stereotaxic target coordinates were 4.20 mm lateral to midline, 3.40 mm anterior and 4 mm ventral to lambda. Current was injected from the 1C/Pt-Ir ('source') to surface carbon ('ground') electrodes. Care was taken to ensure stimulation electrodes

(1C, 2C, DBS, Pt-Ir) in samples 1-4 were parallel to $\mathbf{B_0}$ (the *z*-axis) as shown in **Figure 4.2(e)**.

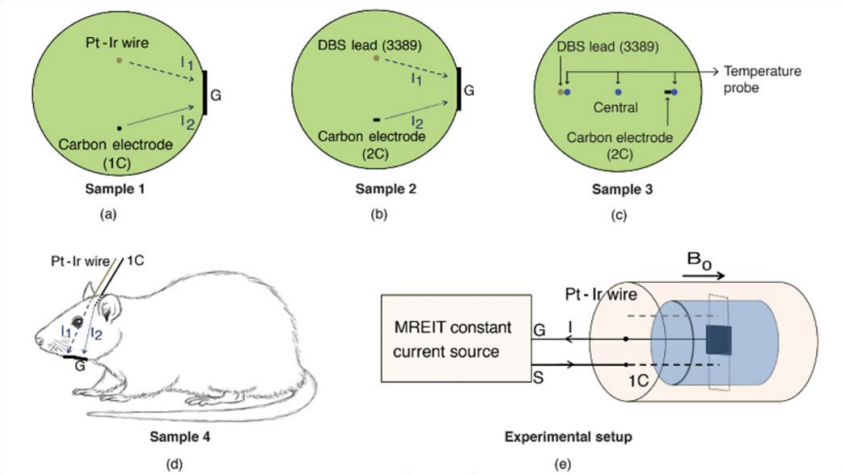

Figure 4.2: MREIT samples and experimental setup. (a) Sample 1: Pt-Ir wire/1C (b) Sample 2: DBS 3389/2C along with ground (G) electrodes (c) Sample 3: DBS 3389/2C and optic-fiber temperature probes in cylindrical gel phantoms (d) Sample 4: Pt-Ir wire/1C and ground electrodes in fixed rodent brain (e) Schematic of MREIT experimental setup of sample 1. Magnetic flux density distributions caused by synchronized current pulses injected from source (S) to ground (G) electrodes were mapped in the imaging slice (dashed rectangle).

4.2.3 Imaging Experiments

Imaging was conducted using a 12-cm bore Bruker Biospin 7 T MRI system (Barrow Neurological Institute, Arizona, USA). A 70-mm birdcage RF volume coil was used for imaging. MR data were acquired using both conventional spin echo (SE) and gradient echo (GE) pulse sequences.

A. MRI Experiments

Imaging was conducted using a 12-cm bore Bruker Biospin 7 T MRI system (Barrow Neurological Institute, Arizona, USA). A 70-mm birdcage RF volume coil was used for imaging. MR data were acquired using both conventional spin echo (SE) and gradient echo (GE) pulse sequences. MR imaging parameters are summarized in **Table 4.1**.

B. MREIT Experiments

A constant current source [94] was used to synchronize monopolar current to a spin echo MREIT pulse sequence (SE-MREIT) via spectrometer transistor-transistor logic control signals [56]. A schematic of a typical MREIT experimental setup is shown in **Figure 4.2(e)**. In MREIT experiments, current was injected via carbon or Pt-Ir electrodes and surface carbon electrodes (cross-sectional area 10×10 mm^2, Hurev, Republic of Korea). Complex k-space MREIT data resulting from two monopolar, biphasic current injections (I^+, I^-) were collected, as shown in **Figure 4.3**.

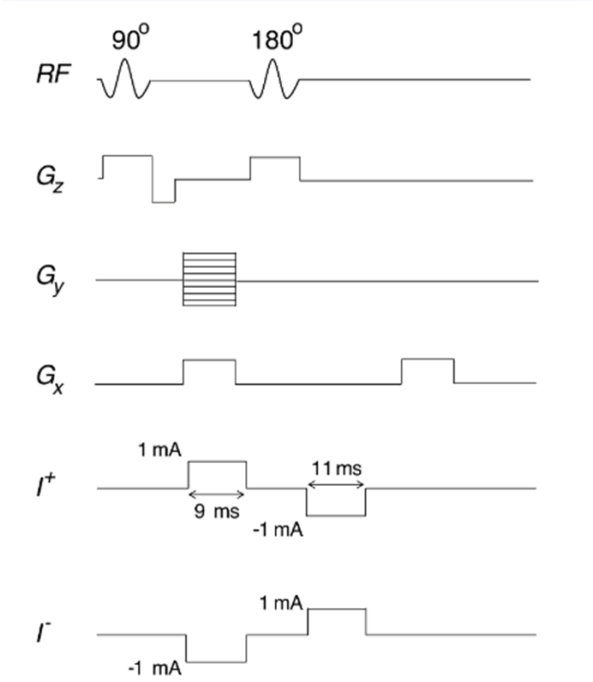

Figure 4.3: Spin echo-MREIT (SE-MREIT) pulse sequence. Positive (I^+) or negative (I^-) MREIT currents were used interchangeably in the SE-MREIT pulse sequence [56].

'Monopolar' refers to a configuration having one electrode placed within a sample and a ground electrode on the sample surface. MREIT currents synchronized with spin echo sequences were reversed after the 180° RF pulse to align with re-phased spins to increase MR phase after the 180° refocusing RF pulse, and were therefore biphasic. Positive (or negative) current was injected for 9 ms between the 90° and 180° RF pulses followed by negative (or positive) current for 11 ms between the 180° RF pulse and start of the read-out gradient. The excess 2 ms current injection was intended to increase MREIT-phase

changes using the ICNE pulse sequence [95] but may have produced some phantom composition changes. The imaging parameters used in MR and MREIT experiments are summarized in **Table 4.1**.

Sample No.	Imaging Parameters								
	SEQ	**TR/TE (ms)**	**FOV (mm^2)**	**Matrix size**	**Δz (mm)**	**No. of slices**	**NAV**	**Current (mA, ms)**	**Scan time (mm:ss)**
1	SE	1491/20	60 × 60	128 × 128	1/3	40/14	2/6	0/1, 0/20	06:21/12:48
	GE	450/6	60 × 60	128 × 128	1	40	8	0, 0	07:40
2	SE	1400/20	60 × 60	128 × 128	1	40	1	0, 0	06:21
	SE	1400/25	60 × 60	128 × 128	1	40	1	0, 0	06:21
	GE[a]	3500/6	60 × 60	128 × 128	1	40	4	0, 0	08:32
	GE[b]	3500/6	60 × 60	128 × 128	1	40	4	0, 0	08:32
	SE	1000/22	60 × 60	128 × 128	1/3	40/14	1/6	0/1, 0/20	06:21/12:48
	GE[c]	501/6	60 × 60	128 × 128	1	40	4	0, 0	08:32
4	SE	1000/22	40 × 40	128 × 128	2.5	10	6	0/1, 0/20	12:48

[a,b] Flip angles used in GE sequences for B_1 field mapping were 40^o and 80^o respectively.
[c] Flip angle used in GE acquisitions for MR magnitude image artifacts was 30^o.

Table 4.1: MRI and MREIT Imaging Parameters. Pulse sequences (SEQ) used were Spin echo (SE) and Gradient echo (GE). Abbreviations of imaging parameters: Repetition time (TR), Echo time (TE), Slice thickness (Δz), Number of averages (NAV), MREIT imaging current (Current) and total scan time (Scan time).

4.2.4 Data Analysis

A. Field Inhomogeneity and MR Magnitude Image Analysis

Local field homogeneity in regions surrounding diameter-matched carbon and Pt-Ir electrodes were assessed using $\mathbf{B_0}$ and $\mathbf{B_1}$ field maps. $\mathbf{B_0}$ field maps were computed using MR phase images acquired using

two different echo times [96]. MR data acquired at two different tip angles was used to compute $\mathbf{B_1}$ field maps [97]. Apparent sizes of diameter-matched carbon and Pt-Ir electrodes were measured on MR magnitude images. Electrode boundaries were estimated by computing FWHM values of magnitude profile plots through electrode centers. Ratios of FWHMs to actual electrode sizes were calculated to assess artifact extents associated with each electrode type.

B. MREIT Analysis

a. Experimental Data Processing (B_z)

Raw data collected from positive and negative MREIT current injections were processed to complex MR images [56]. Complex images from positive and negative MREIT current injections were divided to remove the systematic phase artifact and extract B_z [56, 98, 99], via

$$B_z(x, y, z_0) = \frac{1}{2\gamma T_c} arg \frac{M_{I^+}(x,y,z_0)}{M_{I^-}(x,y,z_0)}. \quad [4.2]$$

b. Synthetic Distributions ($\boldsymbol{J^0}, B_z^0$)

Uniform-conductivity ($\sigma = 1\ S/m$) finite-element (FE) computational models constructed from experimental MREIT magnitude data were solved for synthetic magnetic (B_z^0) and current density ($\mathbf{J^0}$) distributions as follows. Experimental MREIT

magnitude data were segmented using ScanIP (Simpleware Ltd., Exeter, UK) into source electrode, ground electrode and gel regions. The resulting meshes were exported to COMSOL 5.0 (COMSOL Inc., Massachusetts, USA). Tetrahedral element FE meshes were used to solve the Laplace equation for the voltage distribution (u) in a domain (Ω) using Neumann boundary conditions. The Laplace equation was solved in the form

$$\nabla.\left(\sigma(\boldsymbol{r})\nabla u(\boldsymbol{r})\right) = 0, \quad [4.3]$$

where $\boldsymbol{r} = (x, y, z)$ is a position vector in $\mathbb{R}^3$. Current density **J** was calculated using **equation 4.4** based on the conductivity (σ) and electric field ($\boldsymbol{E} = -\nabla u$) distribution within Ω

$$\mathbf{J}(\boldsymbol{r}) = -\sigma(\boldsymbol{r})\nabla u(\boldsymbol{r}). \quad [4.4]$$

The *z*-component of the induced magnetic flux density B_z in Ω was computed from the solved current densities in MATLAB using a Fourier transform version of the Biot-Savart law

$$B_z^0(r) = \frac{\mu_0}{4\pi}\int J(r') \times \frac{r-r'}{|r-r'|^3}\,dr', \quad [4.5]$$

where $\mu_0 = 4\pi \times 10^{-7}$ Tm/A is the permeability of free space.

C. Projected Current Density ($\mathbf{J}^{\mathrm{P}}$)

Current flow distributions were reconstructed as the projected current density ($\mathbf{J}^{\mathrm{P}}$) [100, 101]. Computation of $\mathbf{J}^{\mathrm{P}}$ involved the combination

of synthetic current and magnetic flux densities ($\mathbf{J}^0$, B_z^0) and experimental magnetic flux density (B_z) as described by,

$$\mathbf{J}^{\mathrm{P}} = \mathbf{J}^0 + \frac{1}{\mu_0}\left(\frac{\partial\left(B_z - B_z^0\right)}{\partial y}, -\frac{\partial\left(B_z - B_z^0\right)}{\partial x}, 0\right). \quad [4.6]$$

4.3 Results

4.3.1 Impedance Characteristics of Carbon and Pt-Ir electrodes

Two-terminal impedance magnitudes (|Z|) for carbon (1C and 2C) electrodes and Pt-Ir (DBS 3389) electrodes are shown in **Figure 4.4**. Data plotted for 1C and 2C electrodes were averaged over 6 samples of each type (one trial each), while measurements for the single DBS lead were averaged over six trials. As expected, 1C electrodes (|Z| = 2570 Ω, R = 1375 Ω), with the smallest contact surface area were found to have higher impedance and resistance values, with the resistance of this electrode type being around 1.4 kΩ at 100 Hz, approximately 6.5× the resistance of the thicker 2C electrodes (|Z| = 437 Ω, R = 210 Ω). While both carbon electrode types had larger resistances and impedances than the DBS lead, the frequency dependence of all electrodes was broadly similar.

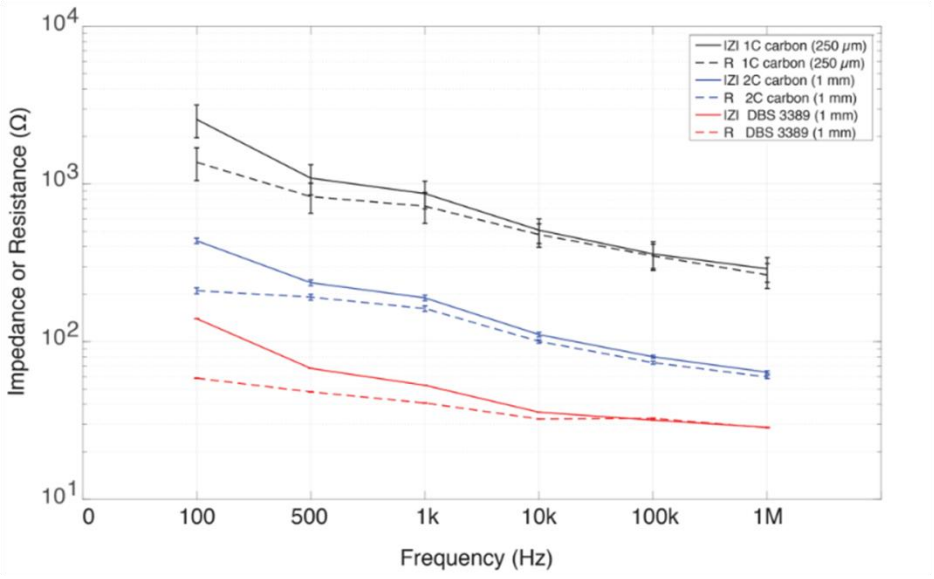

Figure 4.4: Electrical characteristics of carbon (1C, 2C) and Pt-Ir (DBS 3389) electrodes. Impedance (|Z|) and Resistance (R) of electrodes as a function of frequency are represented with solid and dashed lines respectively for 1C (250-μm diameter, black) and 2C carbon electrodes (dimensions 1000 × 500 μm^2, blue) and a single DBS 3389 electrode (1270-μm diameter, red). Mean (±SE, standard error) values measured for one trial of six samples of each carbon electrode type are shown. Measurements for the DBS lead were sampled six times and averaged to produce mean and SE values. Lengths of all carbon electrodes were approximately 45 mm.

4.3.2 Field mapping and MR magnitude artifacts surrounding carbon and Pt-Ir electrodes

Local $\mathbf{B_0}$ and $\mathbf{B_1}$ field inhomogeneities surrounding diameter-matched carbon (2C) and Pt-Ir (DBS lead 3389) electrodes in sample 2 are shown in **Figure 4.5**. The $\mathbf{B_0}$ field map in **Figure 4.5(b)** shows local decreases in field strength nearby both electrode types. However, there is a region of negative values around Pt-Ir and a positive region around carbon

electrodes. **Figure 4.5(c)** demonstrates larger spatial extent and scale of $\mathbf{B_1}$ inhomogeneity surrounding Pt-Ir electrodes compared to carbon electrodes. $\mathbf{B_1}$ inhomogeneities had an extent 3.32× around Pt-Ir electrodes and 0.74× around carbon electrodes compared with actual electrode sizes.

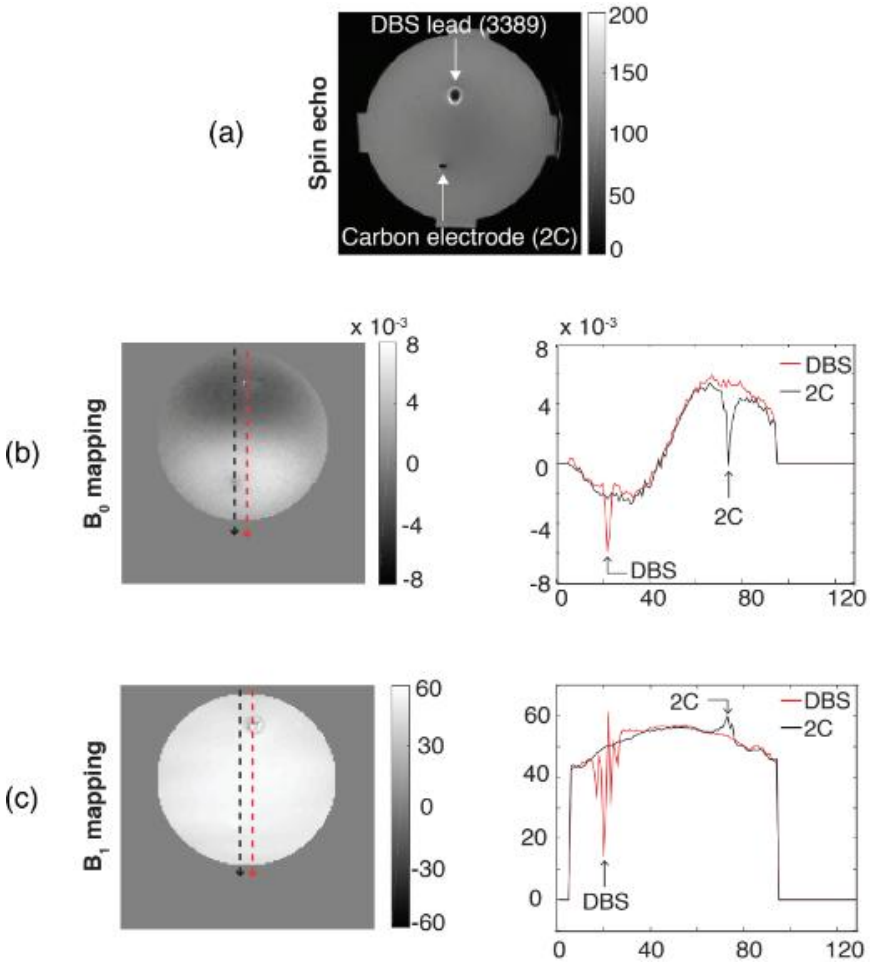

Figure 4.5: $\mathbf{B_0}$ and $\mathbf{B_1}$ field maps. (a) MR magnitude image showing Pt-Ir (DBS 3389) and carbon (2C) electrodes placed within cylindrical gel phantom. (b) $\mathbf{B_0}$ and (c) $\mathbf{B_1}$ field maps with vertical profiles through DBS 3389 (red) and carbon (black) electrodes.

Artifacts surrounding diameter-matched carbon and Pt-Ir electrodes in Samples 1 and 2 are shown in **Figure 4.6**. FWHM values for electrodes in

SE and GE acquisitions are summarized in **Table 4.2**. In general, apparent sizes of carbon electrodes were smaller than those of diameter-matched Pt-Ir electrodes. Substantial differences between apparent sizes were noted between the 1C and Pt-Ir wire electrodes, with apparent sizes of Pt-Ir electrodes being 21.19× in SE and 15.62× in GE images and apparent sizes of 1C electrodes being 2.59× in SE, and 1.81× in GE images.

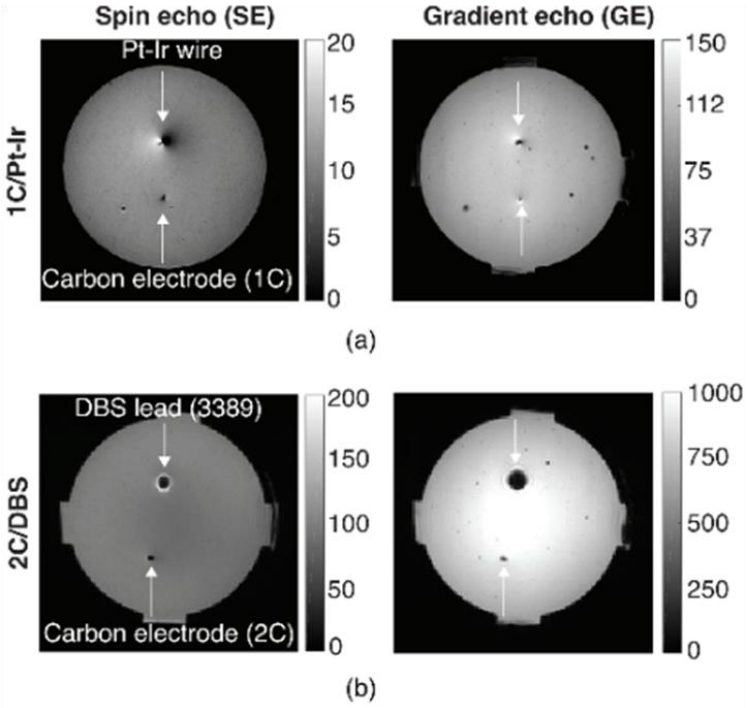

Figure 4.6: Susceptibility artifacts. Comparison of MR magnitude image artifacts around carbon (1C, 2C) and Pt-Ir (wire, DBS 3389) electrodes during spin echo (SE) and gradient echo (GE) acquisitions. (a) One-contact (1C, 250-μm diameter) carbon and Pt-Ir wire (203-μm diameter) (b) Two-contact (2C, dimensions 1000 × 500 μm^2) and Pt-Ir DBS 3389 (1270-μm diameter) electrodes placed in cylindrical gel phantoms (Samples 1 and 2).

Electrodes	Actual diameter (mm)	Voxel size (mm)	Apparent diameter (FWHM, mm)	
			Spin Echo	Gradient Echo
1C carbon	0.27	0.47	0.70 (2.59×)	0.49 (1.81×)
Pt-Ir wire	0.21	0.47	4.45 (21.19×)	3.28 (15.62×)
2C carbon	1.40	0.47	1.88 (1.34×)	1.41 (1.00×)
DBS 3389	1.27	0.47	2.34 (1.84×)	4.69 (3.69×)

Table 4.2: FWHM extents of artifacts surrounding diameter-matched carbon and Pt-Ir electrodes for spin echo (SE) and gradient echo (GE) sequences.

4.3.3 Temperature Changes near Carbon and Pt-Ir Electrodes

The temperature evolution recorded in sample 3 under the influence of continuous RF sinusoidal signals (amplitude = 10 mW, frequency = 298 MHz) transmitted through the surface coil is shown in **Figure 4.7**. Initial temperatures recorded from each sensor were subtracted and values are presented here show two-minute moving-averages of temperature changes over the 30-minute recording period. Temperatures around Pt-Ir electrodes increased by 0.9^{o}C during recording whereas those around carbon electrodes increased by 0.1^{o}C under similar RF energy deposition conditions. The temperature at the central temperature probe steadily increased, with a final temperature ranging between those of carbon and Pt-Ir electrodes.

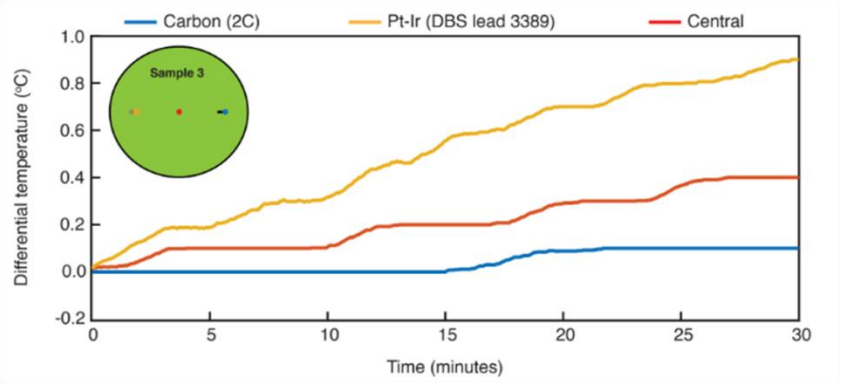

Figure 4.7: MR-related thermal effects. Local temperature changes around carbon (2C) and Pt-Ir (DBS 3389) electrodes under continuous RF excitation (amplitude = 10 mW, gain = 30 dB, frequency = 298 MHz). Inset shows a cylindrical gel phantom with both electrode types (Sample 3), and temperature sensors with solid circles. The progression of local temperature changes at temperature-sensing tips under continuous RF excitation around carbon (yellow), Pt-Ir (blue) electrodes and a central (red) sensor over 30 minutes is shown.

4.3.4 Magnetic Flux (B_z) and Current Density ($\mathbf{J}^{\mathrm{P}}$) Distributions

Reconstructed magnetic flux density (B_z) and current density magnitude (J^P) distributions established within homogeneous gel phantoms and fixed tissue samples during SE-MREIT are shown in **Figure 4.8**. Synthetic magnetic flux density (B_z^0) and current density magnitude (J^0) were combined with experimental B_z to reconstruct J^P distributions. The slice shown was chosen close to exposed electrode areas. Active electrode areas (1C, 2C, DBS) were masked as precisely as possible to minimize noise contribution from electrode-artifact regions. Slight misalignments of stimulation electrodes (1C, 2C, DBS) contributed to the formation of dipoles in measured B_z distributions. B_z dipoles around the active DBS

electrode (**Figure 4.8(a)**) were not observed in B_z^0, possibly because the cylindrical geometry of the DBS electrode led to field cancellation. Possible mismatches in electrode orientation (**Figures 4.8(b-d)**) between experimental and simulation conditions led to differences in orientations of B_z and B_z^0 dipoles. The scales of B_z and J^P distributions were similar for diameter-matched 2C-G and DBS-G configurations (**Figure 4.8(a-b)**). Current densities surrounding the cylindrical DBS lead were symmetric. However, the J^P distribution around 2C electrodes was relatively asymmetric. Local current density magnitudes (arrows) around non-current-carrying DBS electrodes were larger than for 2C carbon electrodes. Error percentages in J^P reconstructions in samples 1, 2 and 4 were 9.9%, 5.16% and 6.44% respectively.

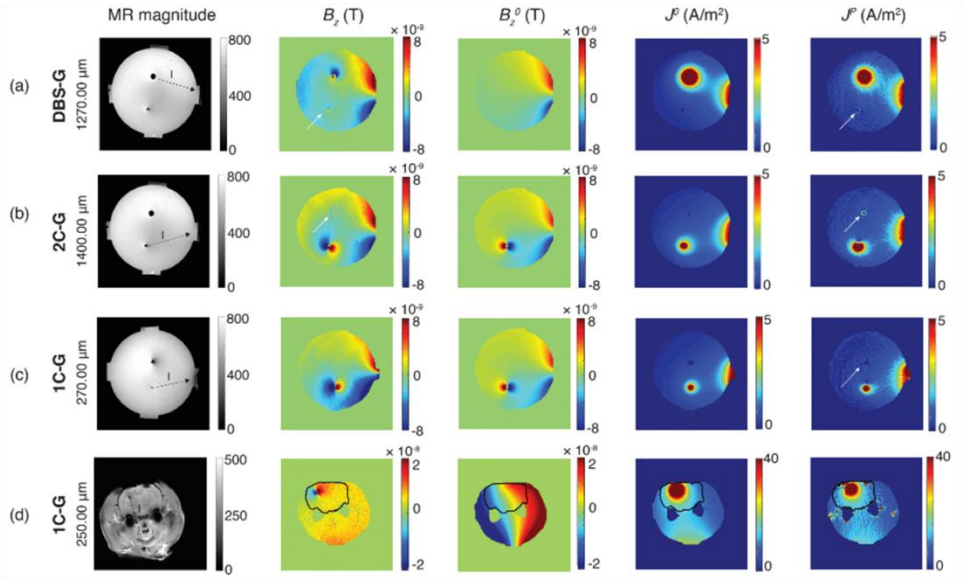

Figure 4.8: Magnetic flux and current density distributions established by synchronized current injection during SE-MREIT. MR magnitude (first column), reconstructed magnetic flux density (B_z, second column), synthetic magnetic flux density (B_z^0, third column), synthetic current

density magnitude (J^0, fourth column) and projected current density magnitude (J^P, fifth column) distributions established via current injections through electrode pairs (a) DBS – G; Sample 2 (b) 2C – G; Sample 2 (c) 1C – G; Sample 1 (d) 1C – G; Sample 4 are shown. Electrode sizes: One-contact (1C) carbon electrodes (250 μm diameter in Sample 1, 270 μm diameter in Sample 4), Two-contact (2C) carbon electrodes (dimension 1000 × 500 μm^2 in Sample 2), platinum-iridium (DBS 3389) electrodes (1270 μm diameter in Sample 2). White arrows indicate non-current carrying electrodes.

4.4 Discussion

DBS currents have traditionally been administered via Pt-Ir electrodes implanted within disease-specific brain targets. Both safety factors caused by electrode heating and metal related artifacts may result when subjects with implanted electrodes undergo MR imaging. Even if imaging is performed safely at 1.5 T — the current safety standard for patients implanted with DBS leads [102], artifacts may prevent clear images being obtained near areas targeted by electrodes. The novelty of this work relates to the characterization of carbon electrodes for MREIT imaging and stimulation as well as mapping current density distributions in DBS settings. Artifact and thermal effects related to each electrode type were compared under SE and GE scanning conditions. It was found that the artifact and thermal characteristics contributed by carbon electrodes were overall smaller than those caused by Pt-Ir electrodes. The smaller temperature changes around non-current-carrying carbon electrodes, along with the finding that impedances, as well as B_z and J^P images created by these electrodes were similar or superior to those obtained using Pt-Ir electrodes, suggests that implanted carbon electrodes may both be suitable for safe delivery of neuromodulation currents in MRI

environments and allow imaging of neuromodulation currents. Therefore, as anticipated, use of carbon electrodes may potentially make MR-guided surgical placement of DBS electrodes easier, enable routine MRI scans to be carried out, and facilitate studies of DBS dosimetry and mechanism via MREIT.

4.4.1 Impedance Characteristics of Carbon and Pt-Ir Electrodes

Characteristic differences between electrode types could be explained using equivalent electrical circuits of the two-terminal test configuration, shown in **Appendix C** (**Section 1.3, Figure C1.2)**. The circuit properties depend on the inline resistance of the electrodes and properties at electrode-electrolyte interfaces. Contributions to the measured impedances due to properties of the copper reference were neglected because of the comparatively large area of copper exposed to the saline solution. As expected, impedances and resistances of smaller carbon electrodes (1C: 500-μm diameter) were largest. Resistances of 1C carbon electrodes were around 6.5× those of 2C electrodes, which was consistent with the approximate ten-fold decrease in electrode surface area. Substantial differences between electrode resistivities ($\rho_{Carbon(1C,2C)} \approx 2\text{x}10^{-5}$ Ω·m [103], $\rho_{Pt-Ir(3389\ DBS)} \approx 2\text{x}10^{-8}$ Ω·m [104]), resulted in inline carbon electrode resistances being much larger than those of DBS electrodes, dominating overall impedance property comparisons. The overall trend of decreasing electrical impedance and resistance observed in all three electrodes with increasing frequency, as shown in **Figure 4.4,** was in

accordance with behavior expected at electrode-electrolyte interfaces [105].The detailed properties of carbon electrode-electrolyte interfaces were not examined here because the exact areas of carbon electrode ends were not precisely known.

A 210 Ω resistance was characteristic of carbon electrode circuits (2C-ground). The DBS-ground electrode pair was around 59 Ω. Replacement of Pt-Ir electrodes with carbon therefore represents usage of approximately 3.5× Pt-Ir power requirements. Typical battery life of current sources using Pt-Ir DBS electrodes is reported as 3-5 years in Parkinson's disease and essential tremor patients [106, 107]. Replacing existing Pt-Ir (DBS) electrodes with carbon (2C), may result in a 3.5× reduction of non-rechargeable battery life, ultimately lasting ≈1.5 years before needing replacement. Use of rechargeable batteries [108-111] may improve the longevity of DBS systems with carbon electrodes, and potentially allow safer MR imaging compared to Pt-Ir electrodes.

4.4.2 Field Inhomogeneity and MR Magnitude Artifacts around Carbon and Pt-Ir Electrodes

$\mathbf{B_1}$ field inhomogeneity around carbon (2C) electrodes had lower spatial extent compared to diameter-matched Pt-Ir (DBS 3389 lead) electrodes as shown in **Figure 4.5**. As expected, the local homogeneity of RF (i.e. $\mathbf{B_1}$)

fields around metal electrodes were affected to a greater extent than around carbon electrodes, potentially leading to larger MR magnitude artifacts around Pt-Ir electrodes as observed in **Figure 4.6**. Carbon consistently showed smaller MR artifacts compared to diameter-matched Pt-Ir electrodes as demonstrated in **Table 4.2**. Artifact extent improved by 12% around carbon compared to diameter-matched Pt-Ir (1C/Pt-Ir wire: 2.59×/21.19× in SE, 1.81×/15.62× in GE) electrodes. These superior MR characteristics of carbon agree with other similar studies [80, 82-84]. Therefore, reduced carbon artifacts are expected to allow easier localization of carbon compared to Pt-Ir electrodes on MR images.

Differential susceptibilities at electrode-medium interfaces produce field inhomogeneities, thereby contributing to artifacts surrounding electrodes [63-65, 80, 83]. Eddy currents induced by gradient switching and/or the RF field are known to contribute to susceptibility artifacts [66]. Moreover, susceptibility variations are known to scale with the static magnetic field strength ($\mathbf{B_0}$) [67, 112]. The paramagnetic susceptibility of Pt-Ir (at 90% platinum and 10% iridium) was reported as 230 ppm ($\chi_{Pt-Ir} = 230$ ppm) [84]. The diamagnetic susceptibility of PAN (polyacrylonitrile)-based carbon, in sharp contrast with Pt-Ir, was reported as -26 ppm ($\chi_{Carbon} = -26$ ppm) [84], although certain grades of carbon fiber have been found

to be paramagnetic [80]. In sum, the lower susceptibility of carbon led to smaller artifacts surrounding carbon electrodes on MRI images.

4.4.3 MRI-induced Heating Mechanisms Influencing Carbon and Pt-Ir Electrodes

Changes in temperature around carbon electrodes during the course of RF energy deposition were smaller than Pt-Ir electrodes, as shown in **Figure 4.7**. Overall, larger temperature increases were observed around Pt-Ir electrodes than for nearby carbon electrodes or the central probe, demonstrating the expected RF heating caused by the presence of metal [68, 69, 82]. Temperatures recorded from sensors next to the Pt-Ir DBS lead increased faster and attained larger values at the end of continuous RF energy deposition compared to carbon (2C) electrodes. Sensors measured both the temperature at electrode tips and that of gel in contact with these electrodes. While the thermal conductivity (k) of Pt-Ir (31 W/mK) is greater than carbon (1.5 W/mK) materials [113], RF heating of Pt-Ir electrodes likely exceeded any changes caused by heat conduction mechanisms. Magnitudes of local temperature increases around Pt-Ir electrodes (0.9^{o}C) exceeded carbon electrodes (0.1^{o}C) by 8%. The central electrode showed an intermediate increase in temperature, reflecting the larger B_1 values in this location.

RF heating near Pt-Ir electrodes in commercially-available DBS leads has been found to be influenced by the length, orientation, and presence of loops in the lead, with heating effects associated with looped DBS leads greater than for straight leads parallel to the longitudinal axial direction of the coil [70, 71, 114]. In the benchtop experiments performed here, the DBS lead orientation was maintained parallel to the axial direction of the simulated-bore, and excess lead length was not looped. Magnitudes of temperature changes observed in gel-phantom experiments (0.9 ^{o}C) were of the same scale as those (1–5 ^{o}C) reported in excised porcine heads at 3 T and 9.4 T implanted with DBS leads oriented parallel to the main magnetic field [70, 71]. The total length of DBS lead used in these benchtop experiments was 40 cm, which was reported as the length associated with maximum heating [114]. Smaller temperature increases around Pt-Ir electrode contacts were observed in this experiment, because of the much lower power used here.

Both this study and those reported in [70, 71] used continuous wave RF excitation. Heating effects may also depend on pulse sequence speed and type. *In vitro* safety studies using fast and high SAR sequences such as turbo spin echo and echo planar imaging have found temperature increases < 2^{o}C at Pt-Ir electrode contacts [115-117]. Overall, RF heating induced temperature increases around Pt-Ir electrodes under optimum conditions

such as non-looped and parallel leads, observed in benchtop experiments were consistent with previous *in vitro, in vivo* and *ex vivo* MR safety studies.

Smaller temperature changes were observed about carbon electrodes than similarly oriented Pt-Ir DBS electrodes, due to carbon having substantially lower conductivity than Pt-Ir or other metallic materials, limiting antenna effects and gradient-related heating effects.

4.4.4 Magnetic Flux Density Component (B_z) and Current Density ($\mathbf{J}^P$) Magnitude Distributions

Similar magnetic flux (B_z) and projected current density magnitude (J^P) distributions were produced using DBS-G and 2C-G electrode configurations (**Figure 4.8(a-b)**). The geometry of electrode boundaries influenced J^P distributions. Rectangular 2C electrodes were surrounded by asymmetrical J^P distributions whereas cylindrical DBS electrodes produced more symmetrical J^P distributions. Electrode pairs were scaled down in size to 270-µm/250-µm diameter 1C carbon electrodes as shown in **Figure 4.8(c-d)**. These smaller electrodes were used in a homogeneous gel phantom and heterogeneous rodent brain samples. B_z and J^P values were eight-fold larger in the fixed rodent head compared to the gel phantom, because of the reduced effective electrode area (G) and volume

of rodent head. As expected, the magnitudes of $\mathbf{J}^P$ distributions surrounding electrode tips were large in all samples.

Within gel phantoms (**Figure 4.8(a-c)**), the diameter-matched and non-current-carrying Pt-Ir electrodes were clearly visible in B_z and J^P distributions established using current-carrying carbon electrodes (1C-G, 2C-G). B_z and J^P values around these non-current-carrying yet highly conductive Pt-Ir electrodes were much larger than for carbon equivalents. Concentrations of current around Pt-Ir electrodes resulting from RF or magnetic gradient induced currents or MREIT current injections may present a risk of tissue burns. Therefore, low-conductivity carbon could be a safer alternative for electrode or implant materials in MRI environments.

4.4.5 Clinical and Experimental Implications

Carbon is proposed as an improved and potentially safer alternative to Pt-Ir due to the improved magnetic field homogeneity, and smaller MR magnitude artifact extent and RF-heating-induced changes observed near carbon electrodes. Post-surgical image analysis near DBS electrode sites may aid in the early diagnosis and treatment of complications, as well as allowing verification of electrode placement. In other clinical imaging procedures, MR magnitude artifacts observed around Pt-Ir electrodes may obscure image features, particularly in fast MR pulse sequences such as

echo planar imaging and would also indicate benefits from the replacement of Pt-Ir with carbon in DBS leads. Furthermore, the ability to perform MR imaging in the immediate surroundings of carbon electrodes will allow for DBS field mapping within neural structures directly affected by DBS currents, paving the way for experimental studies geared towards understanding neuromodulatory mechanisms underlying DBS.

4.5 Conclusion

Carbon electrodes were found to have superior MR artifact and thermal performance, while having similar impedance properties to conventional DBS electrodes. The smaller thermal changes observed in the neighborhood of carbon electrodes indicate that they should also allow subjects to safely undergo other routine MR imaging procedures. The DBS-style carbon electrodes developed in this work may be appropriate for use with fast imaging sequences and stronger main magnetic fields, potentially enabling DBS-fMRI studies and improved intra- and post-operative monitoring. Improved imaging near electrodes combined with spatial mapping of MR magnetic flux and electrical current density around carbon electrodes may allow experimental determination of current density within target brain structures and aid in probing mechanisms underlying DBS. Carbon electrodes developed, characterized and tested for use in rodents were surgically implanted into the hippocampus as described in **Chapter 5**. These electrodes were

used for imaging current delivery during fMREIT experiments as described in **Chapter 6**.

5. DEVELOPMENT OF *IN VIVO* ANIMAL MODEL FOR MR-BASED FUNCTIONAL BRAIN MAPPING

5.1 Introduction

MREIT has been extensively studied in passive tissue phantoms composed of homogeneous and heterogeneous conductivity distributions [56, 118]. More recently, MREIT has been indicated for use in functional (fMREIT) neuroimaging [3]. The ability of fMREIT to successfully detect neural activity was demonstrated in *in vitro* preparations of bloodless Aplysia Abdominal Ganglia (AAG) [4, 6]. The clinical translation of fMREIT necessitates the *in vivo* detection of neural activity. Therefore, an *in vivo* animal model was developed to investigate the ability of fMREIT to detect neural activity in physiological environments similar to the human brain.

5.1.1 Rationale for the Use of Animals

Animal research has led to major biomedical advancements, particularly in neuroscience, physiology, psychology, immunology, pharmacology and toxicology [119]. Although a wide variety of mammalian species is available, the rat has been the most widely used animal models in preclinical phases of biomedical research [120]. The well-characterized rodent brain is ideal for use in the study of functional neural systems [33]. The largely similar (~95%) genetic make-up of rats with humans, and the well-understood physiological pathways in rats, led to rats being the

optimal choice for neuroscientific studies [119]. Moreover, rats are hardy animals and resistant to infections compared to higher-order mammals [120].

Forepaw and whisker stimulation of rodents has been well-studied, and known to be reliable models for inducing neural activity in *in vivo* settings. Whiskers are the main effector organs in rodents with whisker representation in the brain being more widespread compared to the forepaw [32]. However, fMRI studies have found that BOLD signal changes associated with whisker stimulation are smaller in magnitude compared to BOLD forepaw stimulation [121]. Considering the technical difficulties in implementing whisker stimulation within an MRI scanner and the inherent increase in BOLD signal magnitudes associated with forepaw stimulation, the stimulation type chosen to evoke neural activity was forepaw stimulation.

Forepaw stimulation in rodents is known to activate the somatosensory cortex, as described in **Section 5.1.2**. Membrane conductance is expected to increase in cortical somatosensory neurons associated with forepaw stimulation. In order to detect these conductance changes using fMREIT, external electrical currents must be applied to map current pathways sensitive to changes in the conductivity distribution. Carbon electrodes

were developed and tested for use in rodent brains, as described in **Chapter 4**, to administer imaging currents in fMREIT experiments. These electrodes were implanted in close proximity to the activated somatosensory cortex, in rodent hippocampi. At the onset of neural activity, neuronal cell membrane conductances have experimentally been measured to increase ~30×. These membrane conductance increases were expected to affect current pathways, thereby affecting magnetic field perturbations recorded as changes in fMREIT phase signals. The anatomy of the somatosensory cortex and hippocampus, and somatosensory pathway involved in forepaw stimulation are described in **Section 5.1.2**.

5.1.2 Rat Nervous system

A. Somatosensory system

The somatosensory system encompasses neural structures from the somatosensory receptors to the cerebral cortex, including primary afferent neurons, ascending spinal pathways, somatosensory nuclei in the brainstem and thalamus [122]. Somatosensory receptors are the peripheral terminals of primary afferent neurons, and are sensitive to mechanical, thermal and other tactile stimuli such as electrical current stimulation [122]. The central processes of primary afferent neurons enter the spinal cord in the dorsal root, which further bifurcate into ascending and descending pathways [122]. Dorsal column pathways

contain ascending collaterals of myelinated primary afferents carrying somatosensory information from the forelimbs to the dorsal column nuclei [122]. Some of the neurons from these nuclei ascend as internal arcuate fibers, cross the midline, enter the contralateral medial lemniscus and terminate in the ventroposterolateral nucleus, part of the somatosensory thalamus [122]. Medullary nuclei such as the dorsal column nuclei, including the gracile, cuneate, and external cuneate nuclei, and nucleus Z receive somatosensory afferents [122]. **Figure 5.1** shows the representation of limbs and forepaws in the dorsal column nuclei. Neurons in these nuclei project to the ventrobasal thalamus; with axons entering the contralateral medial lemniscus, ascending to terminate in the ventral posterolateral nucleus of the thalamus [122]. Thalamocortical afferents from the ventral posterolateral nucleus project into the somatosensory cortex [122].

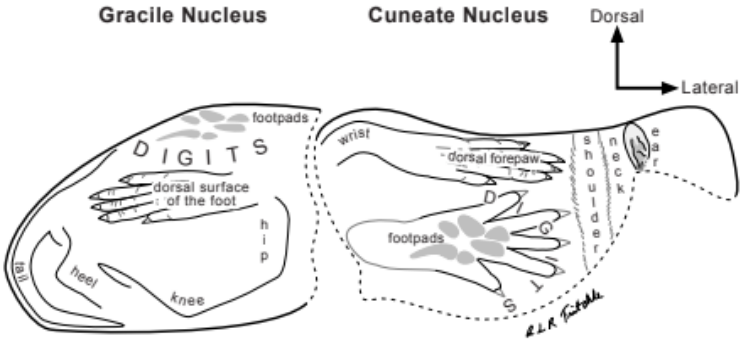

Figure 5.1: Somatotopic organization of dorsal column nuclei – gracile and cuneate nuclei [122].

The somatosensory cortex has two regions, namely, the first and second somatosensory areas (SI and SII) [122]. In rats, SI contains a complete somatotopic representation of the contralateral body. The tail is represented medially and the foot and trunk more laterally, the forelimb further lateral and the face and oral structures most lateral [123]. On the other hand, SII contains another complete representation of the face and body as shown in **Figure 5.2** [122].

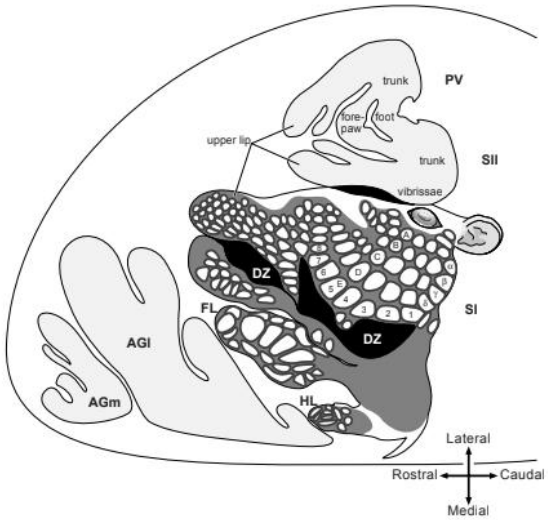

Figure 5.2: Somatotopic organization of the first and second somatosensory areas (SI and SII). Abbreviations include FL, forelimb area; HL, hindlimb area; AGl, lateral agranular cortex corresponding to the primary motor area; AGm, medial agranular cortex corresponding to supplementary motor area; DZ, dysgranular zone [122].

B. Forepaw electrical stimulation to evoke neural activity in rat somatosensory cortex

Non-invasive cortical brain activation has been achieved through the stimulation of the rat forepaw [124-126], hindlimb [126], tail [126],

whiskers [124, 127] and olfactory bulb [128]. Forepaw stimulation is a type of peripheral nerve stimulation that activates the contralateral forepaw area of the primary somatosensory cortex. Of the available peripheral stimulation types, forepaw stimulation was preferred due to large BOLD-fMRI signal changes and well-characterized neural activity [129]. BOLD signal change magnitudes are frequency-dependent, with maximal forepaw responses measured at 1.5 Hz whereas whisker stimulation yielded maximum BOLD responses at 12 Hz in α-cholarose anesthetized rodents [121]. The activation area and magnitude of BOLD signals measured under forepaw stimulation were larger when compared to whisker stimulation [121]. Although the exact magnitudes of BOLD signal changes under isoflurane may differ from α-cholarose, in general, fMRI activations associated with forepaw stimulation were assumed to exceed whisker stimulation irrespective of the anesthetic agent.

Forepaw stimulation was shown to provide robust activation of the primary somatosensory cortex. The somatosensory pathway relaying neural information from electrical stimulation of the rat forepaw to the somatosensory cortex is shown in **Figure 5.3**. Electrophysiological recordings have demonstrated activations in cortical and subcortical structures under forepaw stimulation. Subcortical structures such as

thalamus, basal ganglia and cerebellum were found to show BOLD signal changes under long pulse durations of forepaw stimulation [130]. However, typical short-duration forepaw stimulation follows the pathway as shown in **Figure 5.3**. Electrical stimulation of the rat forepaw is encoded and conducted by afferent nerves through the spinal cord, synapse, across the midline in the medulla and the ventroposterolateral nucleus (VPL) of the thalamus. Impulses are further conducted to the primary somatosensory cortex (SI) and secondary somatosensory cortex (SII) through neurons that project from the thalamus. Neurons from somatosensory cortical areas cross the midline in the pons, and finally project to the cerebellum [33].

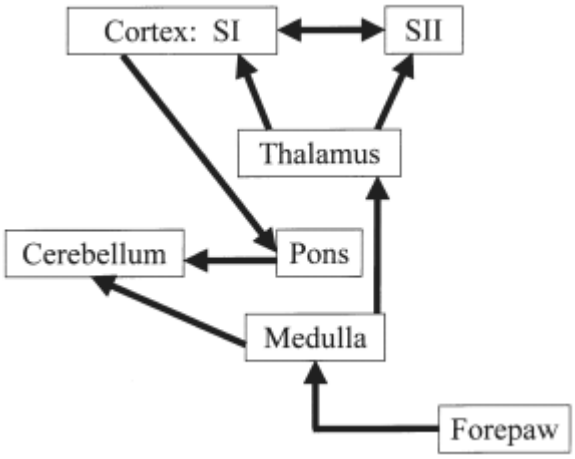

Figure 5.3: Somatosensory pathway responsible for contralateral somatosensory activations associated with electrical stimulation of the rat forepaw [33].

Electrical stimulation parameters such as current amplitude, pulse width and onset-to-onset intervals (i.e. frequency) are used to generate

forepaw stimulation waveforms [131]. Standard forepaw stimulation parameters are 1 – 2 mA current amplitude, 0.3 ms pulse width and 3 Hz frequency. Each parameter impacts the time-course of cerebral blood flow, and therefore the BOLD signal. Furthermore, care must be taken to accommodate for neural adaptation effects, which is reduction in neural response over time, based on the frequency and duration of stimulation [129]. Maximum neural and hemodynamic changes, unaffected by neural adaptation, were observed for short duration (<10 s) at 8 – 12 Hz frequency and long duration (>30 s) at 6 – 8 Hz frequency [129].

C. Hippocampus

The hippocampus is a heterogeneous region involved in sensory, emotional and cognitive processing [132]. In rodents, the hippocampus is a relatively large, cashew-shaped structure lying just beneath the neocortex [132], with the longitudinal axis in the dorsal-ventral direction. Dorsal hippocampus is the most rostral whereas the hippocampus curves ventrally at caudal levels [132]. The hippocampus is divided into three *cornu ammonis*(CA) fields, namely, CA3, CA2 and CA1, as shown in **Figure 5.4**.

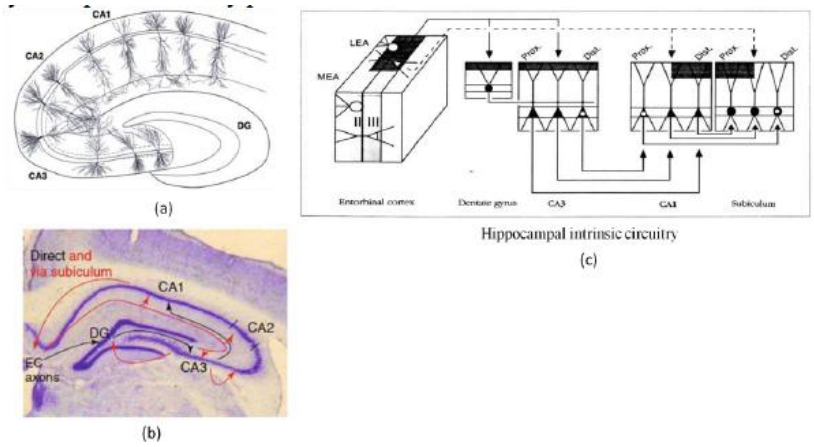

Figure 5.4: Structure and connectivity of the hippocampus. (a) Organization of pyramidal neurons in CA1, CA2 and CA3. (b) Trisynaptic circuit (c) Functional connectivity in the hippocampal formation [132, 133].

Pyramidal cells and interneurons are the two types of cells in the hippocampus [132]. Pyramidal cells are smaller (dendritic length ~ 13.5 mm, soma ~ 193 μm^2) and tightly packed in CA1 [132]. CA1 pyramidal cells show remarkable homogeneity of their dendritic trees – one apical dendrite or two dendrites [132]. The firing patterns of CA1 neurons are in the frequency of 1-10 Hz with amplitude 100 mV [132]. CA2 pyramidal cells share similarities between CA1 and CA3 pyramidal cells since CA2 represents a transition region between CA1 and CA3 fields. CA2 has large pyramidal cell bodies similar to CA3, however without mossy fiber innervation similar to CA1 [132].

CA3 pyramidal cells exhibit substantial heterogeneity in dendritic organization [132]. Small CA3 pyramidal cells (dendritic length ~ 8-

10 mm, soma ~ 300 μm^2), located in the limbs of the dentate gyrus (DG), receive little to no direct input from the entorhinal cortex (EC) [132]. Larger CA3 cells (dendritic length ~ 16 - 18 mm, soma ~ 700 μm^2), located distally in the field receive only apical mossy fiber input [132, 133]. Bursting is a hallmark feature of firing patterns in CA3 pyramidal neurons with 30 – 50 ms duration and 100 – 300 Hz frequency [132]. A heterogeneous group of interneurons are scattered through the layers of the hippocampus [132], with cell bodies lying in the pyramidal cell layer and axons projecting on dendritic shafts and dendritic spines of pyramidal cells or other interneurons [132].

The anatomical connectivity of the hippocampus described by the "trisynaptic circuit" (**Figure 5.4(b, c)**) shows the classical circuitry for information processing. The first link begins in the entorhinal cortex (EC) and ends in the dentate gyrus (DG), providing major cortical input to the hippocampus. The link provides the strongest projections via the perforant path to the dentate gyrus [134, 135]. The second link begins in the granule cells of DG and ends on CA3 pyramidal cells via the mossy fiber pathway [134, 135]. The third link is between axons of the CA3 pyramidal cells and CA1 pyramidal cells via the Schaffer Collateral pathway [134, 135].

5.1.3 Effects of forepaw stimulation and hippocampal imaging currents on target neurons

The *in vivo* animal model suggested for neural activity detection using fMREIT involves the simultaneous use of two independent electrical interventions, namely forepaw stimulation of the somatosensory cortex and hippocampal imaging currents for fMREIT imaging. Forepaw stimulation induces neural activity in the somatosensory area (SI) and somatosensory area (SII) of the somatosensory cortex. Carbon electrodes placed in the hippocampus for imaging current delivery are ~ 3 mm from SI and ~ 5 mm from SII. **Figure 5.5** illustrates the location of hippocampal current delivery electrodes (1-C) and surrounding electrical field with respect to the forepaw-activated SI and SII. To consider the influence of each electrical intervention separately, the following cases are discussed:

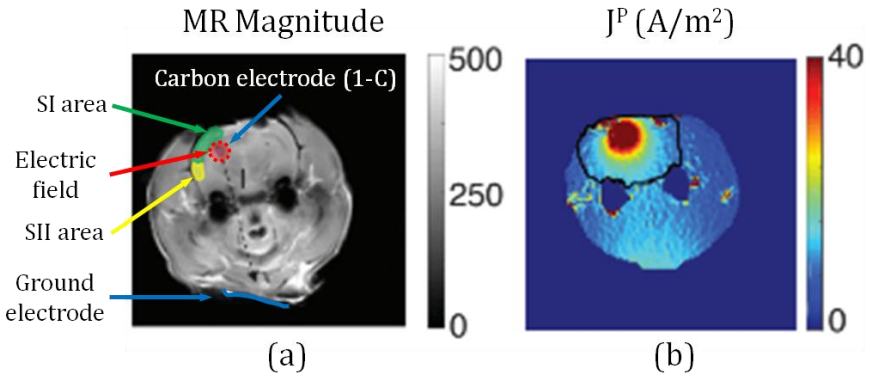

Figure 5.5: Illustration of hippocampal 'imaging' current delivery electrode relative to target somatosensory areas. (a) MR magnitude image showing the position of 'imaging' current delivery electrode (1-C, blue) within the hippocampus. Electrical fields around the hippocampal carbon electrode is shown in red. Somatosensory areas (SI in green and SII in yellow) show the regions of somatosensory cortex activated by forepaw stimulation. (b)

Current density distribution due to hippocampal 'imaging' current injection in *ex vivo* rat head.

A. Forepaw stimulation applied without hippocampal imaging currents

When forepaw stimulation is applied, pyramidal cells in SI and SII generate action potentials and transmembrane currents. These active pyramidal cells are considered to be dipole current sources [136]. If a recording electrode is placed at the hippocampal current injection site, the amplitude of recorded signals varies inversely with the square of the distance between active neurons and the recording electrode [136]. Previous pyramidal cell recordings detected spikes 50 μm from an active neuron using a monopolar electrode [136], however intrinsic current flow resulting in spikes from SI and SII neurons is not expected to be visible at electrode-neuron distances of 3 mm and 5 mm in the hippocampus.

B. Hippocampal imaging currents applied without forepaw stimulation

Carbon electrodes (1-C) implanted in the hippocampus deliver fMREIT imaging currents to image neural activity in SI and SII. Assuming constant current pulses of -1 mA amplitude are delivered as imaging currents, the current required for extracellular stimulation of pyramidal cells in the somatosensory cortex is given as threshold

current ($I_{threshold}$) includes intrinsic and external current contributions [137]:

$$I_{threshold} = I_o + kr^2, \quad [5.1]$$

where I_o = absolute threshold, k = current-distance constant that ranges from 155 μA/mm^2 to 3460 μA/mm^2 in pyramidal cells and r = distance between stimulating electrode and neuron. I_o is the minimum amount of current needed to elicit an action potential at r = 0 [137]. I_o and k are intrinsic parameters of a neuron, and are independent of a stimulating electrode. kr^2 accounts for contribution from extracellular electrical currents delivered by external electrodes, such as carbon electrodes for imaging current delivery [138]. Contributions from hippocampal -1 mA current pulses to the threshold current of SI pyramidal neurons and SII pyramidal neurons may be calculated using kr^2. Assuming k = 200 μA/mm^2, the threshold currents of SI pyramidal neurons (r = 3 mm) exceed 1.8 mA and SII pyramidal neurons (r = 5 mm) exceed 5 mA. Therefore, the likelihood of stimulation in SI pyramidal neurons depends on I_o magnitude, however, the stimulation of distant SII pyramidal neurons is highly unlikely. As a carbon electrode is placed in the hippocampus, there is a high probability of stimulation in hippocampal neurons. To assess the stimulatory effect of imaging currents, functional imaging experiments were performed with and without forepaw stimulation.

C. Use of both forepaw stimulation and hippocampal imaging currents

Hippocampal imaging currents are applied for the whole duration of fMREIT acquisitions, whereas forepaw stimulation is applied for shorter periods. When forepaw stimulation is applied along with pre-existing imaging currents, target somatosensory neurons will undergo neuronal depolarization. Conductivity increases in regions of active neural tissue may allow imaging currents to concentrate as electrical currents follow the path of least resistance. Potential imaging current concentrations in the somatosensory cortex may allow interaction between transmembrane and ionic currents of somatosensory neurons with hippocampal imaging currents. However, under the assumption of no association between neural activity induced by forepaw stimulation and stimulation of neurons by hippocampal imaging currents, it should be possible to isolate the effects of forepaw stimulation by comparing fMREIT phase signals measured during forepaw stimulation (*stim*) with baseline (*rest*) time periods.

5.2 Materials and Methods

The development of an animal model for fMRI/fMREIT imaging experiments necessitated the delivery of electrical currents into the rat hippocampus in conjunction with forepaw stimulation. Custom MREIT carbon electrodes were

developed and tested in passive phantoms and *ex vivo* neural tissue, as described in **Chapter 4**, prior to the surgical implantation of a pair of carbon electrodes into rat hippocampi. Each carbon electrode was deployed into the hippocampus, and anchored to the skull using 10 mm-diameter cannulas. To accommodate these relatively large-sized cannulas on the rat head, and ensure mechanical fit within a 70 mm MRI bore during imaging, care was taken to choose rats of appropriate size. Sprague Dawley rats (female) weighing 370 g - 390 g were found to serve as stable animal models under the aforementioned surgical and imaging space constraints over 3-month imaging periods.

5.2.1 Surgery

A surgical procedure was developed to implant needle-shaped carbon electrodes at 50^{o} to the dorsoventral axis with electrode tips placed into rodent hippocampi. A detailed description of the surgical procedure is provided in **Appendix A.**

A. Pre-operative preparation

Prior to surgery, the weight, age and health status of the animal was evaluated. Ketamine and xylazine cocktail was administered as an intraperitoneal injection to induce anesthesia. Ketamine has been known to produce sedation and respiratory depression, however, ketamine is often premixed with xylazine to achieve surgical plane of

anesthesia. After confirming anesthetic depth through a foot pinch test, an ophthalmic ointment was applied over the eyes to prevent corneal drying. Owing to the large surface to body weight ratio in rodents, hypothermia is a serious problem that could prolong anesthetic effects, thereby increasing the risk of complications. A warm fluid bag was placed under the anesthetized animal to maintain adequate body temperature (32 - 34^{o}C).

To prepare the surgical site for skin incision, the portion of the head between the ears and eyes was shaved using hair clippers. The shaved area was further cleaned using gauze soaked in a disinfectant (for example, chlorhexidine). To spatially localize the rat hippocampus with respect to skull landmarks, the anesthetized rat was mounted on a stereotaxic frame in skull flat position. After loading the front teeth over the bite bar, the ear bars were locked into the head through the ear canal. The shaved head portion was disinfected using chlorhexidine and ethyl alcohol (70%) immersed cotton swabs with linear strokes.

B. Intra-operative procedure

A midline skin incision starting between the eyes and extending 2 cm over the cranium was made using a single scalpel stroke. Four towel clamps were used to open the skin incision. Using a cotton swab, the periosteum was gently removed to expose the coronal and sagittal

sutures. Using a needle mounted on a stereotaxic probe holder, the spatial coordinates of skull landmarks, namely Bregma and Lambda, were determined for use with a stereotaxic atlas of the rat brain [120]. Using stereotaxic coordinates of skull landmarks and the distance between each landmark and the hippocampal target, the skull entry position into the hippocampus was determined. Tissue edges and the skull surface was moistened with sterile saline drops to prevent tissue drying.

A stereotaxic arm inclined at 50^{o} to the vertical with a needle-tip was positioned over the entry point on both left and right hemispheres of the skull. Using a fine-tip sterile skull marker, both entry points were marked on the skull surface. Once the locations were marked, the head was tilted 20^{o} in the ventral direction and the arm was adjusted to 30^{o} for ease of drilling. A dental drill was used to carefully drill burr holes of 10 mm diameter at each entry point. Each burr was ~2 mm deep to get through the skull thickness. The drilling process was intermittent with short periods of moistening the burr hole with water drops to reduce friction-induced heating. Both holes were further threaded using a tap for up to 2 threads, and later screwed in with cannulas for up to 2-3 threads, as shown in **Figure 5.5(a)**.

A head cap was made using dental cement to secure both cannulas to the skull. After solidifying, a pair of carbon electrodes were deployed through the capillary of each cannula for a length of ~12 mm such that electrode tips were introduced within the hippocampus. Dummy caps were screwed onto the cannulas to secure the electrodes in place, as shown in **Figure 5.5(b)**.

C. Post-operative management

Post-operative care was aimed at recovery from anesthesia and pain management. Fluids (composition and volume) were administered subcutaneously to help with anesthesia metabolism, and meloxicam was provided for pain management. Body temperature was maintained between 32 ^{o}C – 34 ^{o}C with a warm fluid bag to prevent heat loss and further aid in anesthetic recovery.

5.2.2 Imaging experiments

Each animal was allowed two weeks of post-surgical recovery before commencing MR imaging experiments in a Bruker Biospin 7T magnet at Barrow Neurological Institute, Phoenix. AZ. The rodent was transferred into a gas chamber for inducing anesthesia using 3-5% isoflurane in air. After confirming absence of response to a foot-pinch test, the rodent was transferred to a preparation table and anesthesia was lowered to 1-2% isoflurane in air delivered through nose cone. Waste gases were vacuumed

out and temperature was maintained between 32-34 ^{o}C. Ophthalmic ointment was applied over the eyes to prevent corneal drying. The region under the rodent's jaw was shaved and cleaned with saline solution to prepare for the placement of a surface electrode. A pair of Pt-Ir needle electrodes were inserted just under the skin of the right (left) forepaw between digits 2 and 4. A dummy cap with carbon wires was secured to the carbon electrode implanted in the left (right) hippocampus. The electrical impedance between forepaw electrodes was measured around 500 kΩ. The surface carbon electrode was smeared with a layer of conductive gel to improve skin contact. The electrical impedance between implanted and surface carbon electrodes was 600 kΩ. The animal was loaded into the magnet and the breathing rate was maintained at ~50 breaths per minute using 1.5 – 2% isoflurane in air. *Carbogen* was used as an alternative to *air*, as an anesthetic medium, for half of the scans (~30 minutes). The breathing rate seemed to decrease when switched from *air* to *carbogen*, however the breathing rate recovered over time (~10 minutes). The MR imaging parameters used in the acquisition of high-resolution anatomical images were TR/TE = 313/5.4 ms, FOV = 40×40 mm^2, slice thickness = 1 mm, matrix = 256×256, number of slices = 25, number of averages = 4, flip angle = 30^{o}. Detailed description of animal preparation for imaging experiments is provided in **Appendix B**.

5.3 Results

Precise localization of a carbon and size-matched Pt-Ir electrode implanted within the rodent brain was achieved through non-invasive and high-resolution MR imaging. **Figure 5.5(c)** shows the sagittal section of a rodent head tilted 40^{o} with a carbon electrode inserted in the rodent brain. **Figure 5.5(d)** shows an axial section of the same rodent brain with a carbon and Pt-Ir electrode implanted in the rodent hippocampus. Although both electrodes are of similar size, large susceptibility artifacts around the Pt-Ir electrode were noted.

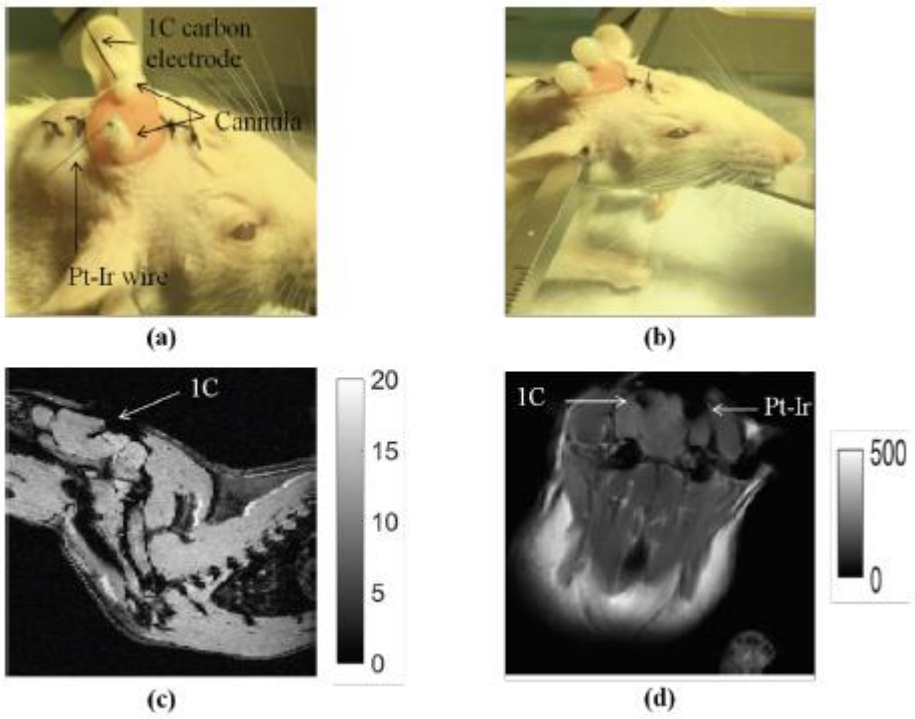

Figure 5.6: Electrode implantation in rodent hippocampi. (a) One-contact (1C) carbon and platinum-iridium (Pt-Ir) electrodes introduced at posterior inclinations of 50^{o} through cannulas (b) Implanted rodent with electrodes secured by dummy cannula caps prepared for imaging (c) Sagittal MR magnitude image showing the trajectory of 1C carbon electrode into the left hippocampus (d) Coronal MR magnitude image showing both 1C and Pt-Ir electrodes terminating in the shown slice.

5.4 Discussion

Development of an *in vivo* model was critical to the practical implementation of fMREIT in preclinical settings. Rodent surgeries mainly involved the implantation of cannulas at a dorsoventral inclination of 50^{o}, through which carbon electrodes were passed into the hippocampus. As shown in **Figure 5.5(a-b)**, long conducting fibers from carbon electrodes were used as connectors to a current source during fMREIT experiments, as will be described in further detail in **Chapter 6**. Dummy cannulas shown in **Figure 5.5(b)** were replaced with wired analogs for MREIT imaging current delivery. MR imaging confirmed the location of carbon electrode tips within rodent hippocampi as shown in **Figure 5.5(c-d)**.

5.5 Conclusion

An asceptic surgical procedure for the bilateral implantation of carbon electrodes into rodent hippocampi was developed for use in high MR fields. The development and characterization of MREIT carbon electrodes are described in greater detail in **Chapter 4**. The use of these carbon electrodes with the *in vivo* animal model for functional brain mapping using individual and contemporaneous fMRI/fMREIT imaging experiments are described in **Chapter 6**.

6. *IN VIVO* DETECTION OF NEURAL ACTIVITY: EXPERIMENTAL DESIGN AND DATA ANALYSIS

6.1 Introduction

Experimental determinations of functional brain maps using fMREIT requires the administration of MREIT imaging current to encode neural activity induced by forepaw electrical stimulation as MR phase changes. To verify the activation of somatosensory cortical areas due to forepaw stimulation, fMRI imaging experiments were performed. Using *a priori* knowledge of tissue conductivities from **Table 2.1**, the electrical conductivity of blood ($\sigma = 0.7$ S/m) is comparable with active neural tissue, and therefore may confound fMREIT phase measurements. Carbogen is preferred as a blood flow suppressant to reduce the contribution of blood to fMREIT phase measurements. As described in further detail in **Section 6.2**, fMRI and fMREIT experiments were conducted using a block-design imaging paradigm to measure stimulation induced neural activity changes in BOLD signals and MR phase.

6.2 Materials and Methods

6.2.1 Experimental Setup

Sprague-Dawley female rats weighing 300-350 g were implanted with carbon electrodes as described in **Section 5.2.1** and **Appendix A**. After two weeks of recovery post-surgery, these rats were anesthetized under 3-

5% isoflurane and 1.5 L/min air for imaging as described in **Appendix B**. Pt-Ir needle electrodes were inserted between the second and fourth digits of the right forepaw for subcutaneous electrical stimulation. A 'ground' carbon electrode was attached to the lower head region to inject MREIT imaging currents as a pair with hippocampal carbon electrodes. MREIT currents were injected between the left hippocampal carbon electrode and 'ground' electrode. Upon confirming the impedance between both electrode pairs to measure ~500 kΩ, the animals were primed for imaging using a 70-mm transmit-receive volume coil in a Bruker Biospin 7T MRI at Barrow Neurological Institute.

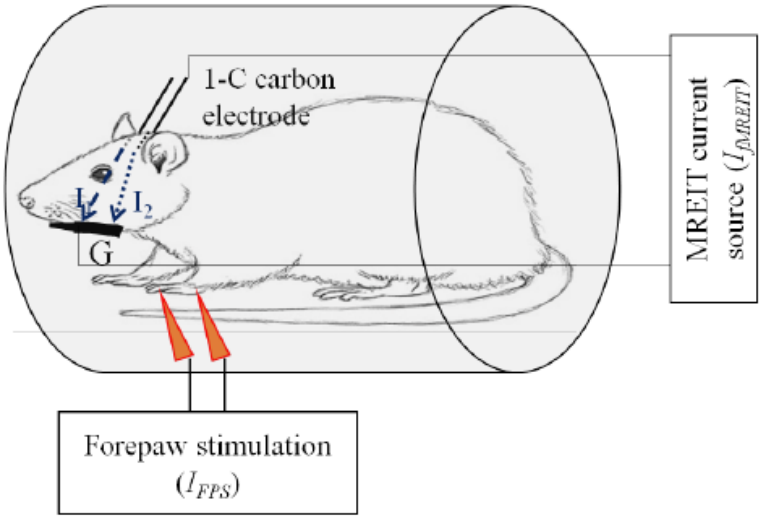

Figure 6.1: Experimental setup during fMRI and fMREIT imaging experiments. Electrical fore-paw stimulation of 2 mA amplitude, 300 μs pulse width and 3 Hz frequency is chosen as a potential method for functional stimulation. Bipolar fMREIT electrical currents are applied with a total charge injection of 3.2 μC.

6.2.2 Imaging Paradigm

Functional imaging using fMREIT and fMRI techniques commenced with high-resolution anatomical acquisitions followed by functional imaging under carbogen and air medium, as shown in **Figure 6.2**. Gradient echo (GE) MR sequences were used to collect high-resolution sagittal and coronal slices of rodent head to locate electrode positions within hippocampi. Medium-resolution multiple slice multiple echo (MSME) MR pulse sequences were used to inject two independent biphasic currents (I_1, I_2) to further confirm electrode positions within MREIT phase images as B_z dipoles.

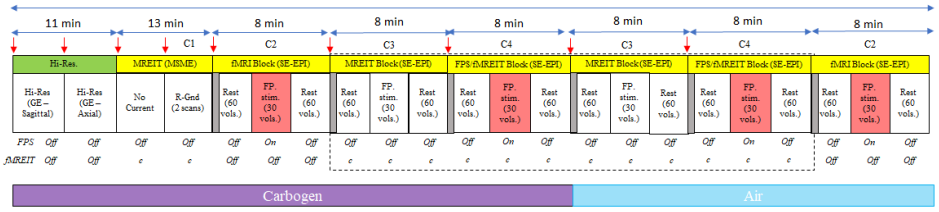

Figure 6.2: Consecutive anatomical and functional imaging experiments conducted per imaging session. From left to right: high-resolution gradient echo (*Hi-Res., GE*) anatomical acquisitions performed for electrode localization; Multiple spin multiple echo MR pulse sequence used for non-functional MREIT imaging (MREIT (MSME)); Spin echo-echo planar imaging (SE-EPI) for plain-fMRI imaging (fMRI Block (SE-EPI)) using forepaw stimulation (I_{FPS}) ; SE-EPI for baseline MREIT imaging (MREIT Block (SE-EPI) using *continuous* (I^{c}_{fMREIT}) MREIT imaging current; SE-EPI for contemporaneous fMREIT imaging (FPS/fMREIT Block (SE-EPI)) using *continuous* (I^{c}_{fMREIT}) MREIT imaging current and forepaw stimulation (I_{FPS}) under carbogen medium. SE-EPI for baseline MREIT and contemporaneous fMREIT imaging was also conducted using *interleaved with rest* (I^{ilr}_{fMREIT}) and *interleaved with positive* (I^{ilp}_{fMREIT}) MREIT imaging currents under carbogen. Forepaw stimulation was applied during 30-volume periods indicated as *FP stim* during plain-fMRI

and contemporaneous-fMREIT imaging scans. $I_{fMREIT}^{c,ilr,ilp}$ were applied during baseline-MREIT and contemporaneous-fMREIT scans. These SE-EPI MREIT, fMRI and fMREIT experiments were repeated under air as shown.

After visually confirming electrode positions, a 160-volume scan using spin echo-echo planar imaging (SE-EPI) was used to acquire fMRI data under forepaw electrical stimulation. Carbogen (1.5 L/min) was switched on to replace air in the isoflurane-air mixture at the beginning of the first anatomical scan, and the effects of carbogen were assumed to have stabilized over the 25-minute period of anatomical and MREIT (MSME) scans. The fMRI imaging block was followed by a MREIT (SE-EPI) imaging block with a *continuous* MREIT imaging current (I_{fMREIT}^{c}), however, the forepaw stimulation (I_{FPS}) was not applied. An fMREIT (SE-EPI) imaging block with similar *continuous* MREIT imaging current (I_{fMREIT}^{c}) and forepaw stimulation (I_{FPS}) was applied. Similar MREIT (SE-EPI) and fMREIT (SE-EPI) was acquired under *interleaved with rest* (I_{fMREIT}^{ilr}) MREIT imaging current and *interleaved with positive* (I_{fMREIT}^{ilp})imaging current. Immediately after completing these imaging blocks, the medium is switched back to air for consecutive MREIT and fMREIT experiments using I_{fMREIT}^{c}, I_{fMREIT}^{ilr} and I_{fMREIT}^{ilp} imaging currents. An fMRI scan is collected towards the end of the imaging paradigm under air using only I_{FPS}. Shannon criteria was used as a starting point for charge and current limits, however, the amplitude of fMREIT current

injection was increased until B_z dipole was observed in MREIT (MSME) images. The imaging parameters for each block in the imaging paradigm are described below and a schematic of current injections are shown in **Figure 6.3**.

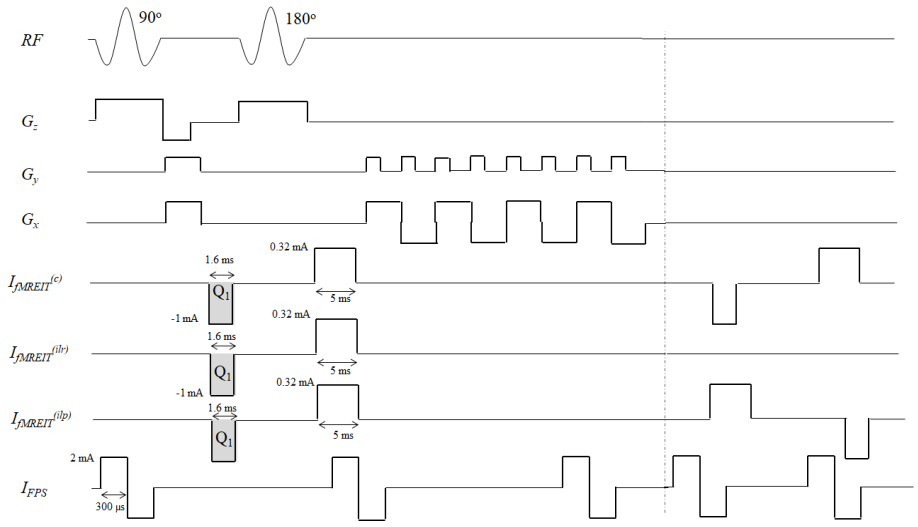

Figure 6.3: Spin echo-echo planar imaging (SE-EPI) pulse sequence with TR = 3 seconds, 160 volumes and total scan time of 8 minutes used in fMREIT and fMRI imaging experiments. The dashed vertical line shows the end of the first TR. Three MREIT current injections used are – *continuous* (I_{fMREIT}^{c}), *interleaved with rest* (I_{fMREIT}^{ilr}) and *interleaved with positive* (I_{fMREIT}^{ilp}) pulses – all inject 3.2 µC per TR. The waveform of MREIT current injections vary in even TRs, as illustrated by the second TR. Forepaw electrical stimulation (I_{FPS}) is shown with 2 mA amplitude, 300 µs pulse width and 3 Hz frequency.

6.2.3 Imaging Parameters

Anatomical (GE): TR/TE = 313/5.4 ms, FOV = 40×40 mm^2, slice thickness = 1 mm, matrix = 256×256, number of slices = 25, number of averages = 4, flip angle = 30^o.

MREIT (MSME): TR/TE = 1000/20 ms, FOV = 40×40 mm^2, slice thickness = 2 mm, matrix = 64×64, number of slices = 12, number of averages = 4, I_{MREIT}= (±200 μA, 8 ms).

fMRI (SE-EPI): TR/TE = 1500/30 ms, FOV = 40×40 mm^2, slice thickness = 2 mm, matrix = 64×64, number of slices = 12, number of averages = 2, number of shots = 1, I_{FPS} = (200 mA, 300 μs, 3 Hz).

MREIT (SE-EPI): TR/TE = 1500/30 ms, FOV = 40×40 mm^2, slice thickness = 2 mm, matrix = 64×64, number of slices = 12, number of averages = 2, number of shots = 1, I^c_{MREIT} = ((-1 mA, 1.6 ms), (0.32 mA, 5 ms)) during the first TR and I^c_{MREIT} = ((-1 mA, 1.6 ms), (0.32 mA, 5 ms)) during the second TR; I^{ilr}_{MREIT} = ((-1 mA, 1.6 ms), (0.32 mA, 5 ms)) during the first TR and I^{ilr}_{MREIT} = ((0 mA, 1.6 ms), (0 mA, 5 ms)) during the second TR, I^{ilp}_{MREIT} = ((-1 mA, 1.6 ms), (0.32 mA, 5 ms)) during the first TR and I^{ilp}_{MREIT} = ((0.32 mA, 5 ms), (-1 mA, 1.6 ms)) during the second TR.

fMREIT (SE-EPI): TR/TE = 1500/30 ms, FOV = 40×40 mm^2, slice thickness = 2 mm, matrix = 64×64, number of slices = 12, number of averages = 2, number of shots = 1, I^{c}_{MREIT} = ((-1 mA, 1.6 ms), (0.32 mA, 5 ms)) during the first TR and I^{c}_{MREIT} = ((-1 mA, 1.6 ms), (0.32 mA, 5 ms)) during the second TR; I^{ilr}_{MREIT} = ((-1 mA, 1.6 ms), (0.32 mA, 5 ms)) during the first TR and I^{ilr}_{MREIT} = ((0 mA, 1.6 ms), (0 mA, 5 ms)) during the second TR, I^{ilp}_{MREIT} = ((-1 mA, 1.6 ms), (0.32 mA, 5 ms)) during the first TR and I^{ilp}_{MREIT} = ((0.32 mA, 5 ms), (-1 mA, 1.6 ms)) during the second TR and I_{FPS} = (200 mA, 300 µs, 3 Hz).

6.2.4 Analysis

fMREIT and fMRI experimental data collected from individual blocks are analyzed in detail in the following subsections. fMREIT data collected using I^{c}_{MREIT} under I_{FPS} and carbogen medium is analyzed in **Section A**. The analysis of fMRI data under I_{FPS} and carbogen medium is described in **Section B**.

A. fMREIT Data Analysis

a. Phase difference (φ_d) and Laplacian of phase difference ($\nabla^2\varphi_d$) images

MR complex data collected using SE-EPI during forepaw electrical stimulation was considered for MR phase image analysis. The first 10 dummy volumes were discarded to allow for MR signal saturation. Successive MR complex images from the remaining 150 volumes were complex divided to compute phase difference (φ_d) images as shown:

$$\varphi_d = Arg\left(\frac{M_c^i(x,y)}{M_c^j(x,y)}\right), \quad [6.1]$$

where M_C^i are complex image volumes of odd volumes and M_C^j of even volumes. Laplacian of φ_d ($\nabla^2\varphi_d$) images were computed with a step size (h) of 1 as:

$$\nabla^2\varphi_d = \frac{\varphi_d(x+h,y)+\varphi_d(x-h,y)+\varphi_d(x,y+h)+\varphi_d(x,y-h)-4*\varphi_d(x,y)}{h^2}. \quad [6.2]$$

Single-slice images of φ_d and $\nabla^2\varphi_d$ (64 x 64 x 75 size) coincident with carbon electrode tips were used to construct fMREIT activation maps.

A standard measure to assess MR image quality is the signal-to-noise ratio (SNR). MR magnitude intensities within a homogeneous region of the rat brain was averaged over 8 voxels to assess signal strength. A similar sized region outside the rat head was chosen to estimate standard deviation of noise in the magnitude image. A ratio of these values was performed to compute SNR in the magnitude image,

$$SNR = 0.635 * \frac{mean(signal)}{standard\ deviation\ (noise)}. \quad [6.3]$$

SNR of magnitude images is insufficient to directly indicate MR phase quality. Instead, SNR is used in calculating baseline noise in φ (s_{φ}) images, noise in φ_d (s_{φ_d}) and noise in $\nabla^2\varphi_d$ ($s_{\nabla^2\varphi_d}$) as,

$$s_{\varphi} = \frac{1}{SNR},$$

$$s_{\varphi_d} = \frac{\sqrt{2}}{SNR},$$

$$s_{\nabla^2\varphi_d} = \left(\frac{20}{\Delta x^4} + \frac{6}{\Delta z^4}\right) s_{\varphi_d}. \quad [6.4]$$

b. Time-periods within φ_d and $\nabla^2\varphi_d$ images

ϕ_d and $\nabla^2\varphi_d$ images ranging over 75-volumes were subject to subcutaneuous electrical stimulation during the *active* time-period spanning volumes (31, 45). Volumes acquired prior to *active* were known as *Rest 1*, with the first 15 volumes (1,15) known as *Rest 1a* and the second 15 volumes (16, 30) as *Rest 1b*. The volumes acquired after *active* were known as *Rest 2*, with the first 15 volumes (46, 60) as *Rest 2a* and the second 15 volumes (61, 75) as *Rest 2b*.

c. Voxel-wise statistical comparisons of between *active* and *rest* time-periods of φ_d and $\nabla^2\varphi_d$ images

t-tests and F-tests were performed to compare average and variance measures of φ_d and $\nabla^2\varphi_d$ within each voxel between *active* and *rest* time-periods. Each rest time-period is represented with a generic 'τ' such that, τ = (*Rest 1a*, *Rest 1b*, *Rest 2a*, *Rest 2b*). Voxel-wise comparisons in φ_d and $\nabla^2\varphi_d$ images of size 64x64 yields 4096 computations per rest period. Statistically significant voxels (t-tests, p <0.05) indicate regions where the average of φ_d (and $\nabla^2\varphi_d$) during *active* are significantly different from *rest* periods. Similarly, significant voxels (F-tests, p <0.05) indicate regions with significantly different variance of φ_d (and $\nabla^2\varphi_d$) between *active* and *rest* periods. Statistical maps produced by voxel-wise t-tests and F-tests indicate activations at each voxel if statistically significant (p <0.05) differences between *active* and *rest* periods are noted. The formulation of voxel-wise statistical comparisons between *active* and *rest* time-periods, at voxel (i, j) where i and j lie within range from 1 to 64, in φ_d and $\nabla^2\varphi_d$ images is:

i. Comparison of means in φ_d between *active* and *rest* time-periods

   Two-sample t-tests were conducted at 95% significance level to test the hypothesis of equal means:

   $$H_o: \mu\left(\left[\varphi_d^{(i,j,active)}\right]_{1\times 15}\right) = \mu\left(\left[\varphi_d^{(i,j,\tau)}\right]_{1\times 15}\right)$$

$$H_a: \mu\left(\left[\varphi_d^{(i,j,active)}\right]_{1\times15}\right) \neq \mu\left(\left[\varphi_d^{(i,j,\tau)}\right]_{1\times15}\right) \quad [6.5]$$

ii. Comparison of variances in φ_d between *active* and *rest* time-periods

Two-sample F-tests were performed at 95% significance level to test the hypothesis of equal variances by comparing sample variances in φ_d (s^2_{active}/s^2_{τ}) during *active* and each *rest* period:

$$H_o: \sigma^2\left(\left[\varphi_d^{(i,j,active)}\right]_{1\times15}\right) = \sigma^2\left(\left[\varphi_d^{(i,j,\tau)}\right]_{1\times15}\right)$$

$$H_a: \sigma^2\left(\left[\varphi_d^{(i,j,active)}\right]_{1\times15}\right) \neq \sigma^2\left(\left[\varphi_d^{(i,j,\tau)}\right]_{1\times15}\right) \quad [6.6]$$

iii. Comparison of means in $\nabla^2\varphi_d$ between *active* and *rest* time-periods

Two-sample t-tests were conducted at 95% significance level as:

$$H_o: \mu\left(\left[\nabla^2\varphi_d^{(i,j,active)}\right]_{1\times15}\right) = \mu\left(\left[\nabla^2\varphi_d^{(i,j,\tau)}\right]_{1\times15}\right)$$

$$H_a: \mu\left(\left[\nabla^2\varphi_d^{(i,j,active)}\right]_{1\times15}\right) \neq \mu\left(\left[\nabla^2\varphi_d^{(i,j,\tau)}\right]_{1\times15}\right) \quad [6.7]$$

iv. Comparison of variances in $\nabla^2\varphi_d$ between *active* and *rest* time-periods

Two-sample F-tests were performed at 95% significance level to test the hypothesis of equal variances by comparing sample variances in $\nabla^2\varphi_d$ (s^2_{active}/s^2_{τ}) during *active* and each *rest* period:

$$H_o: \sigma^2\left(\left[\nabla^2\varphi_d^{(i,j,active)}\right]_{1\times15}\right) = \sigma^2\left(\left[\nabla^2\varphi_d^{(i,j,\tau)}\right]_{1\times15}\right)$$

$$H_a: \sigma^2\left(\left[\nabla^2\varphi_d^{(i,j,active)}\right]_{1\times15}\right) \neq \sigma^2\left(\left[\nabla^2\varphi_d^{(i,j,\tau)}\right]_{1\times15}\right) \qquad [6.8]$$

d. fMREIT Activation Maps

Statistical testing for differences in φ_d and $\nabla^2\varphi_d$ between *active* and *rest* periods leads to 4096 *p*-values per comparison. These 4096 values were rearranged as *p*-value images of size 64x64 to reflect the *p*-value at voxel (i,j) resulting from statistical comparisons at voxel (i,j) between *active* and a *rest* period. These *p*-value maps indicate the presence of differential activity in voxels with significant φ_d and $\nabla^2\varphi_d$ differences (p <0.05) between *active* and *rest* periods correlated with forepaw stimulation. φ_d encodes current density changes caused by imaging current pathways due to conductivity changes related to neural activity. $\nabla^2\varphi_d$ images show spatial changes in membrane conductivity to reveal locations of neural activity. fMREIT activation maps, also known as *p*-value maps, indicate stimulation-induced neural activity in voxels coincident with p <0.05.

In addition to computing fMREIT activation maps of size 64x64, spatial averages and standard deviations of φ_d and $\nabla^2\varphi_d$ were calculated using block size of 4x4. The mean and standard deviation of each image in the 64x64x75 φ_d and $\nabla^2\varphi_d$ image volumes was calculated using contiguous blocks to produce mean and standard deviation maps of size 16x16. The mean of φ_d should be relatively unchanged between *active* and *rest* periods due to scanner noise and drift. Standard deviations of φ_d and $\nabla^2\varphi_d$ quantify the variability of fMREIT phase (φ_d and $\nabla^2\varphi_d$) due to activity-related conductivity changes in neural tissue integrated over the echo time of the imaging sequence [4, 6, 139]. Mean of $\nabla^2\varphi_d$ could potentially show activity related phase changes. Therefore, spatially averaged fMREIT activation maps of size 16 x 16 may reveal activity-related phase changes not reported by 64 x 64 size fMREIT activation maps.

B. fMRI Data Analysis

Complex MR datasets were collected using SE-EPI sequences during forepaw electrical stimulation under varying hemodynamic environments. Forepaw stimulation (2 mA amplitude, 3 Hz frequency, 0.3 ms pulse width) was applied to either the left or right forepaw

using a block design (60 volumes during *rest*, 30 volumes during *active*, 60 volumes during *rest*). Isoflurane, used as the inhalation anesthetic, was delivered using either *air* or *carbogen* as the inhalation medium. Switching between *carbogen* and *air* facilitated hemodynamic manipulation by allowing control over blood flow around active neuronal regions. fMREIT imaging currents were switched off during plain-fMRI and baseline-MREIT imaging, and were switched on during contemporaneous fMRI/fMREIT imaging. Three distinct fMREIT imaging current waveforms were chosen from as described in **section 6.2.2**.

Plain-fMRI and contemporaneous fMRI/fMREIT datasets were analyzed using SPM 12 (Statistical Parametric Mapping). Datasets with acceptable SNR levels (spatial and temporal) and minimal head movement were processed using a first-level general linear model for single subject analysis. The steps used to process a typical functional dataset to produce fMRI activation maps in SPM12 are detailed as:

1. DICOM to NIFTI file format conversion

   Each functional dataset comprised of 160 imaging volumes – 10 dummy, 60 *Rest*, 30 *Active* and 60 *Rest* – in DICOM format. Excluding the first 10 dummy volumes, the remaining 150

functional volumes were converted to the NIFTI file format using the ‘DICOM Import’ utility in SPM12.

2. Pre-processing
    a. Slice timing - The SE-EPI imaging sequence collects data as a set of 2D images, known as slices, rather than the entire 3D imaging volume. To correct for intrinsic acquisition delays between image slices, the time-course of voxel data was interpolated such that all slices were acquired at the same time stamp. The inputs provided to the slice timing utility were - number of slices = 12, TR = 1.5 seconds, TA = 1.375 seconds, slice order = (1:2:12 2:2:12) and reference slice = 11.

    b. Motion correction - Head movement during functional scans may cause motion-induced BOLD activations, thereby obscuring neural activity related BOLD signal changes. The ‘Realign (EST&RES)’ utility was used to assess the extent of head motion during functional scans. Using a motion threshold equal to a voxel side (i.e. 0.625 mm), if the movement exceeded 0.625 mm in any volume of the functional dataset, the entire dataset was discarded.

c. Registration - Spatial alignment between the fMRI activation map and a high-resolution structural dataset is necessary to localize activation patterns with brain structures. A structural dataset was aligned with the mean of 150 volumes in a functional dataset using the 'Coregister (EST&RES)' utility, and specifying the mean functional image as *reference* and structural image as *source*.

d. Smoothing - Data points in functional volumes are averaged with their neighbors to suppress high frequency signals while enhancing low frequencies. fMRI signals are convolved with a Gaussian function of a suitable size for spatial smoothing. Gaussian kernel size is specified as Full width half maximum (FWHM), which usually begins with twice the voxel side. Using the 'smooth' utility, the 150 realigned volumes are smoothed using Gaussian kernels of FWHM measuring 1.25 x 1.25 x 1.25 mm.

3. General linear model (GLM) - The time series of fMRI signals are modeled as a linear combination of explanatory variables to test whether activity in a specific brain region is associated with forepaw stimulation as:

$$Y = X * \beta + \varepsilon \quad [6.9]$$

where Y is the observed BOLD response, X is the design matrix, β is related to parameter estimates and ε is the error . The 'specify 1st-level' utility is used for single-subject GLM analysis with the following as inputs - units for design = scans, inter scan interval = 1.5 seconds, condition 1 = (Name = Rest, Onsets = (1, 91), duration = (60, 60)), condition 2 = (Name = Active, Onsets = 61, duration = 30), basis functions = canonical HRF.

Statistical testing using t-contrasts with (-1, 1) as the weights vector and *p*-value as p <0.05, brain regions showing differential neural activity associated with forepaw stimulation was overlayed over coregistered structural images.

6.3 Results

fMREIT and fMRI analysis of a single dataset acquired using SE-EPI during forepaw stimulation (60 volumes *rest*, 30 volumes *active*, 60 volumes *rest*) under *carbogen* and *continuous* imaging current is explained below.

6.3.1 fMREIT Data Analysis

MR complex data was processed to magnitude, phase (φ), phase difference (φ_d) and Laplacian of phase difference ($\nabla^2\varphi_d$) distributions as

described in equations **6.1 - 6.2,** and these images are shown for a specific imaging volume (volume #45) in **Figure 6.4**.

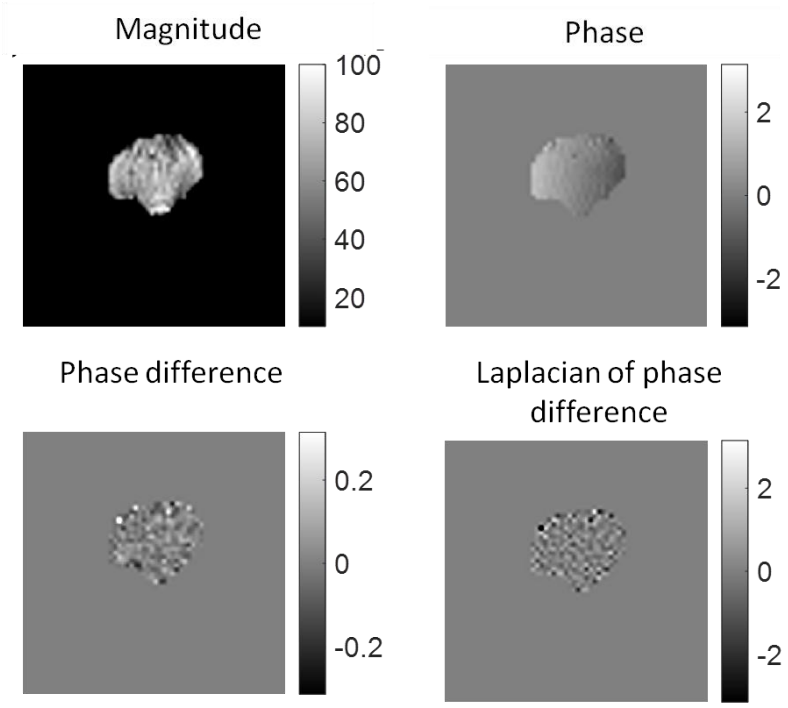

Figure 6.4: Magnitude, fMREIT phase (φ), fMREIT phase difference (φ_d) and Laplacian of phase difference ($\nabla^2\varphi_d$) in a candidate volume (for example, volume 45) spanning across the whole rat brain under air medium and *continuous* imaging current.

Data quality was assessed by computing measures of baseline noise in φ, φ_d and $\nabla^2\varphi_d$ images as described in equation **6.4**. SNR in magnitude images was computed as 107.12, and the baseline noise in φ, φ_d and $\nabla^2\varphi_d$ was found as $9.2\text{x}10^{-3}$, $1.3\text{x}10^{-2}$ and $2.0\text{x}10^{-7}$ respectively.

φ_d and $\nabla^2\varphi_d$ images across 150 imaging volumes were divided into five groups (*Rest*$_{1a}$, *Rest*$_{1b}$, *Active*, *Rest*$_{2a}$, *Rest*$_{2b}$) of 15 successive imaging

volumes. Statistical testing between *active* and *rest* periods in φ_d and $\nabla^2\varphi_d$ images using two-sided t-tests and F-tests at 95% significance level at each voxel to produce *p*-value maps, also known as fMREIT activation maps. fMREIT activation maps due to F-tests between *active* and *rest* periods in φ_d images, as described in **Equation 6.8**, is shown in **Figure 6.5**. Similarly, fMREIT activation maps resulting from t-tests and F-tests of φ_d and t-tests of $\nabla^2\varphi_d$ between *active* and *rest* periods were computed.

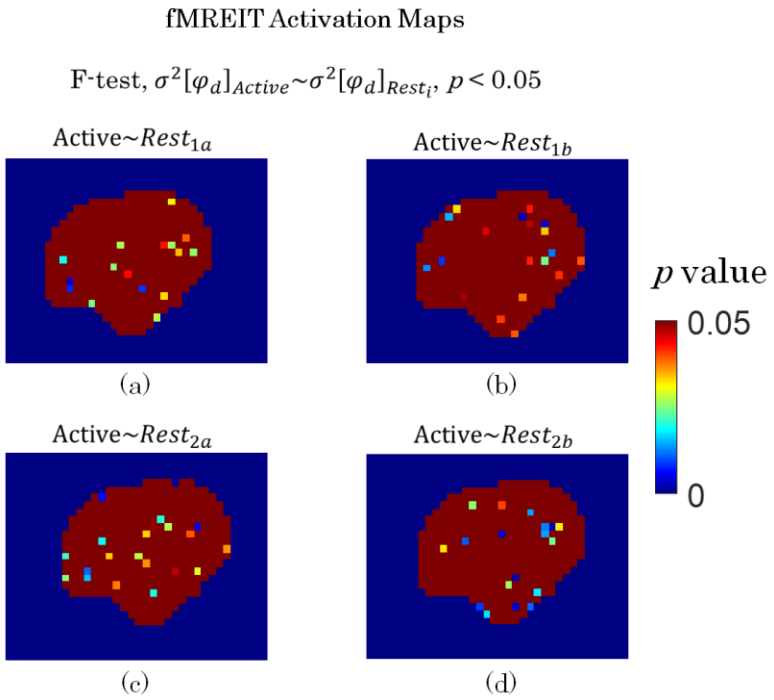

Figure 6.5: fMREIT activation maps showing *p*-values resulting from voxel-wise statistical comparisons of φ_d by conducting two-sided F-tests between (a) *active* and $Rest_{1a}$ (b) *active* and $Rest_{1b}$ (c) *active* and $Rest_{2a}$ (d) *active* and $Rest_{2b}$ time-periods within a rat brain. Color map shows *p*-values ranging within (0, 0.05). Brown represents $p >= 0.05$. Other colors represent $p < 0.05$ which may indicate neural activity due to forepaw stimulation.

Density and distribution of statistically significant voxels in fMREIT activation maps shown in **Figure 6.5**, vary across time-period comparisons. $Rest_{1a}$ shows the largest number of significant voxels that are widely spread across the brain. Significant voxels are concentrated in the activated somatosensory cortical region in **Figure 6.5(c)**. $Rest_{1b}$ and $Rest_{2b}$ show comparable distribution and number of significant voxels in the rat brain.

6.3.2 fMRI Data Analysis

fMRI image analysis of the same imaging dataset, as described in **Section 6.3.1**, was performed using the first-level general linear model in SPM12. Head movement during the functional imaging scan is shown about six degrees of freedom as translation and rotation in **Figure 6.6**. Motion was negligible when compared with the imaging voxel size of 0.625 mm.

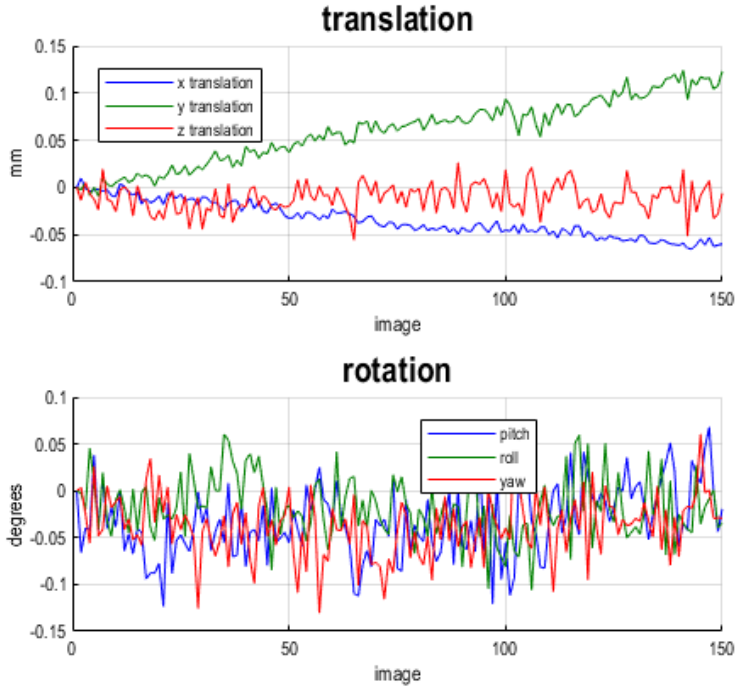

Figure 6.6: Head motion during SE-EPI based functional imaging acquisition.

BOLD regions of differential neural activity in a rat brain overlaid on a coregistered structural image are shown in **Figure 6.7**. Voxels showing statistically significant differences between *active* and *rest* conditions ($p < 0.05$) are shown in red. Note that activations in the brain occur only in somatosensory cortical regions.

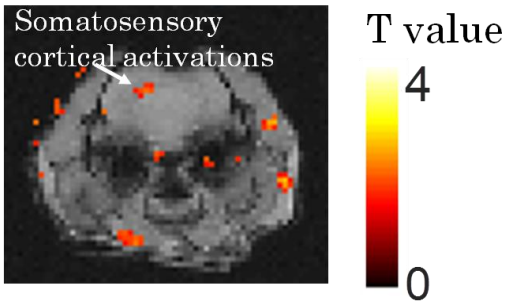

Figure 6.7: fMRI BOLD activation map displayed over a coregistered structural image. Color map shows T-values within range (0, 4).

6.4 Discussion

As the first *in vivo* study to detect neural activity using fMREIT, several measures were taken to minimize the effects of potentially confounding physiological signals, and therefore ensure the proper detection of neural activity related changes in membrane conductivity. Vascular networks surrounding active neural tissue could obscure subtle conductivity changes because of the relatively high conductivity of blood ($\sigma = 0.7$ S/m). Carbogen was delivered as an inhalation medium to saturate blood effects and therefore desensitize MR phase signals to blood flow. Functional imaging experiments were conducted under air and carbogen media to determine the influence of blood on fMREIT signals, as discussed in **Chapter 7**.

Forepaw electrical stimulation was used to induce neural activity in the somatosensory cortex. fMRI BOLD activation maps shown in **Figure 6.7**. demonstrates neurovascular activity in the first somatosensory cortical area (SI).

These somatosensory cortical activations are in agreement with those found in similar *in vivo* fMRI studies [140].

fMREIT activation maps were produced as fMRI BOLD map equivalents to investigate regions of neural activity identified by fMREIT. BOLD maps display t-values marking those exceeding the critical value as being statistically significant. fMREIT maps, however, represent *p*-values as a result of two-tailed t-tests and F-tests. fMREIT maps with p-values < 0.05 are equivalent to t-values exceeding the critical value, and are designated as statistically significant voxels.

fMREIT activation maps of shown in **Figure 6.5** show heterogeneous *p*-value distribution across rest periods. $Rest_{1a}$ shows the largest extent of significant voxels potentially indicating changes related to signal saturation. $Rest_{1b}$ and $Rest_{2a}$ are temporally adjacent to *active* period, and therefore are useful to compare with *active*. The density and distribution of significant voxels differ greatly between $Rest_{1b}$ and $Rest_{2a}$. $Rest_{1b}$, the rest time-period immediately before forepaw stimulation, shows larger number of active voxels with greater spread across the brain compared to $Rest_{2a}$, which is the rest period immediately after forepaw stimulation. The mismatch in $Rest_{1b}$ and $Rest_{2a}$ fMREIT maps suggests the presence of potential restorative mechanisms after forepaw stimulation, that were absent during $Rest_{1b}$. Relative similarity between $Rest_{1a}$ and $Rest_{2b}$ is suggestive of the return of baseline processes after forepaw stimulation.

6.5 Conclusion

On comparing fMRI activation maps with fMREIT, it is evident that the spatial specificity of fMRI maps is greater than fMREIT. The computation of fMRI and fMREIT activation maps detailed here are utilized on multiple datasets, and analyzed in the context of changing imaging currents and hemodynamic environments in **Chapter 7**.

7. *IN VIVO* FMREIT/FMRI MAPPING OF EVOKED NEURAL ACTIVITY UNDER ELECTRICAL CURRENT AND HEMODYNAMIC CONDITIONS

7.1 Introduction

Experimental design and analysis pipelines for a single fMREIT/fMRI dataset have been described in detail in **Chapter 6**. These analyses were used on multiple datasets under varying imaging conditions collected from the same subject and same imaging session to determine whether fMREIT can detect neural activity *in vivo*.

7.2 Materials and Methods

Experimental data collected as described in **Chapter 6** are used for analysis here. Three fMREIT current waveforms – *continuous* (c), *interleaved with rest* (ilr) and *interleaved with positive* (ilp) pulses – were used along with two media – *carbogen* and *air*. fMREIT and fMRI experimental data were analyzed using the single dataset pipelines described in **Section 6.2.4** respectively.

A. Confirm somatosensory activations induced by forepaw stimulation using fMRI

   Electrical stimulation of a rat forepaw is known to induce neural activity in the contralateral somatosensory cortex, as detailed in **Chapter 5**. The functional imaging paradigm used to measure neural activity using fMREIT needs hippocampal imaging currents (*continuous, interleaved with rest*,

interleaved with positive) to encode activity-related conductivity changes as MR phase changes. Magnitude portions of the complex data collected was analyzed for fMRI BOLD activity maps to indicate neurovascular changes around active neural tissue. fMRI BOLD maps were computed using *SPM12* under three cases – in the absence of imaging currents, absence of forepaw electrical stimulation and the presence of both imaging currents and forepaw stimulation – to validate somatosensory cortical activations due to forepaw electrical stimulation.

B. Phase difference (φ_d) images across imaging current waveforms

Phase difference (φ_d) images were computed from the phase portion of MR complex data for acquisitions under both inhalation media (*air* and *carbogen*) and imaging current (*continuous, interleaved with rest, interleaved with positive*) waveforms. fMREIT phase (φ_d) analysis was conducted in distinct regions of the brain - contralateral cortical, ipsilateral cortical, cortical, non-cortical and whole brain regions as shown in **Figure 7.1**.

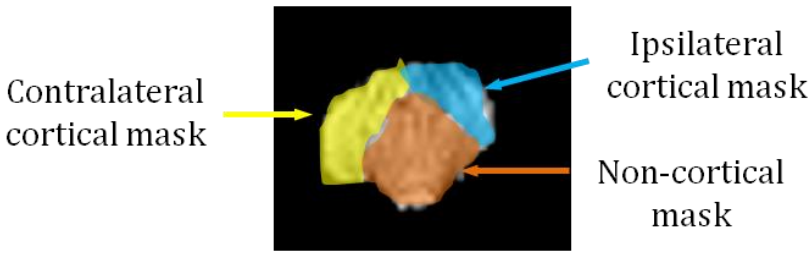

Figure 7.1: Brain sub-structure masks to categorize whole brain into distinct contralateral cortical, ipsilateral cortical and non-cortical masks for use in fMREIT analysis.

Contralateral cortical mask was defined as the cortical portion of the brain contralateral to the site of forepaw stimulation, and somatosensory activations due to forepaw stimulation are expected in the contralateral cortical region. Ipsilateral cortical mask was the ipsilateral portion of the cortex that is not stimulated by forepaw stimulation. Contralateral and ipsilateral cortical regions were combined to form the cortical mask. Non-cortical mask covered the portion of the brain without the cortical mask. A 'representative' brain voxel from the somatosensory cortex contralateral to the site of forepaw stimulation was chosen to track φ_d and $\nabla^2\varphi_d$ changes over time.

C. Standard deviation of phase difference (φ_d) and Laplacian of phase difference ($\nabla^2\varphi_d$)

Aggregate measures of variance in φ_d and $\nabla^2\varphi_d$ for each imaging volume was computed as standard deviations of φ_d and $\nabla^2\varphi_d$ within contralateral cortical, ipsilateral cortical and whole brain regions using brain masks shown in **Figure 7.1**.

D. Contemporaneous fMRI/fMREIT analysis

Functional images acquired using SE-EPI during imaging current application and forepaw electrical stimulation are known as 'contemporaneous fMRI/fMREIT' experiments. Magnitude portion of the MR complex image is analyzed in SPM for fMRI BOLD activation maps. Phase portion is further processed to produce phase difference (φ_d) maps. Voxel-wise two-tailed F-

tests between *active* and *rest* time-periods were computed to produce fMREIT activation maps for each rest period.

E. Statistical significance in fMREIT activation maps in *air* and *carbogen* medium

fMREIT activation maps displayed *p*-value images for voxel-wise comparisons between *active* and *rest* periods using two-sided t-tests or F-tests at 95% significance level. Two-sided F-tests were performed on φ_d and $\nabla^2\varphi_d$ images under *air* and *carbogen* media within contralateral cortical, ipsilateral cortical, whole cortical, non-cortical and whole brain regions. Cumulative numbers of active voxels ($p < 0.05$) within each region was compared across imaging sessions for all six combinations of inhalation media and imaging current types.

7.3 Results

A. Confirm somatosensory activations induced by forepaw stimulation using fMRI

Functional imaging using fMREIT consists of contemporaneous fMRI/fMREIT experiments as described in **Chapter 6**. fMREIT needs imaging currents to detect neural activity related conductivity changes in the brain. Since forepaw stimulation was chosen to induce neural activity, the

effect of imaging currents on neural activity induced by forepaw stimulation was assessed, as described below.

a. Use of forepaw stimulation only

Plain-fMRI functional imaging experiments conducted using SE-EPI without hippocampal imaging currents were processed to BOLD activation maps as shown in **Figure 7.2**. Neural activity was induced in the contralateral somatosensory cortex (white arrows) under *air* medium. These activations were not found under *carbogen* medium, thereby validating the use of *carbogen* to saturate blood effects.

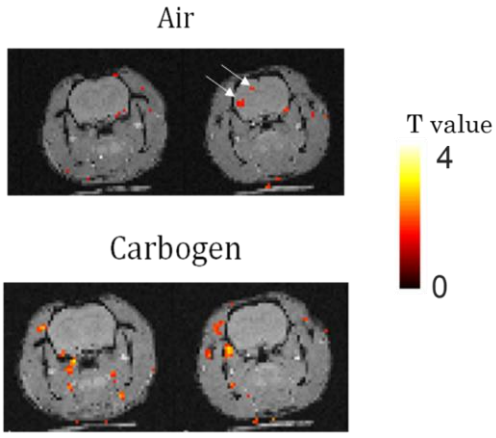

Figure 7.2: BOLD maps (T-values) acquired during plain-fMRI acquisitions under *air* or *carbogen* inhalant without imaging currents. SPM maps superimposed over structural images show forepaw stimulation associated activations in primary somatosensory cortex (SI; upper white arrow) and secondary somatosensory cortex (SII; lower white arrow) under *air*, as indicated by white arrows.

b. Use of hippocampal imaging current only

Functional imaging experiments using the same imaging parameters, inhalation media and external imaging currents were conducted without the use of forepaw electrical stimulation. In the absence of forepaw stimulation, contralateral somatosensory cortical areas were not found active, as shown in **Figure 7.3**.

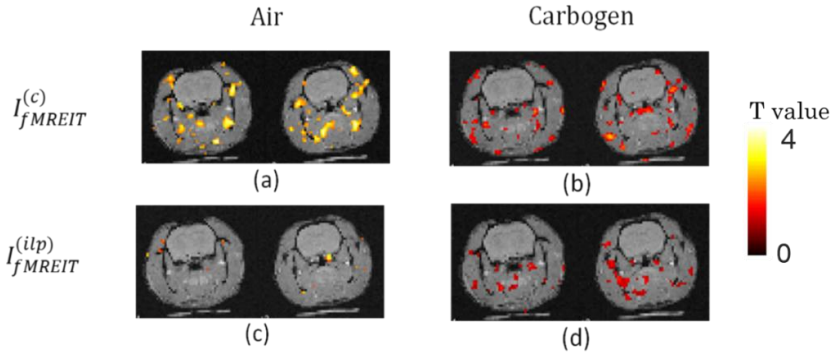

Figure 7.3: BOLD maps (T-values) acquired during contemporaneous fMRI/fMREIT imaging without forepaw stimulation. No somatosensory activations noticed under (a) *air* and *continuous* (b) *carbogen* and *continuous* (c) *air* and *interleaved with positive* (d) *carbogen* and *interleaved with positive* current waveforms.

c. Use of both forepaw stimulation and hippocampal imaging currents

Contemporaneous fMRI/fMREIT functional imaging experiments were conducted using SE-EPI under *air* and *carbogen* media as well as three imaging current waveforms. **Figure 7.4** shows somatosensory activations under *continuous* imaging currents in *air* medium, however, these activations were not sustained in *carbogen*. Somatosensory activations were reduced under *interleaved with rest*, and sustained in *air* and *carbogen* media. No cortical activations were observed under *interleaved with positive* imaging currents.

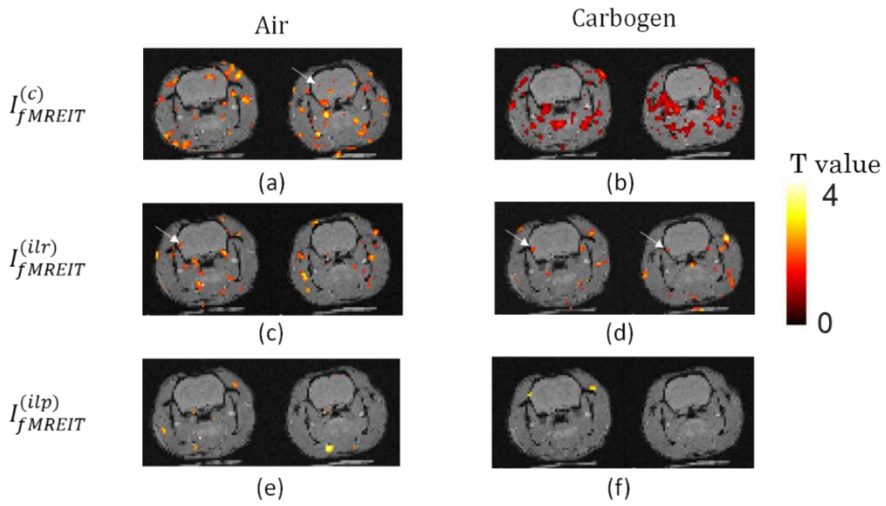

Figure 7.4: BOLD maps (T-values) from contemporaneous fMRI/fMREIT experiments under three imaging current waveforms - *continuous* (*c*), *interleaved with rest* (*ilr*) and *interleaved with positive* (*ilp*) - and two inhalation media - *air* and *carbogen*. White arrows show somatosensory activations.

B. Phase difference (φ_d) images across imaging current waveforms

Variations of phase difference (φ_d) images in a representative brain voxel under all combinations of media (*air*, *carbogen*) and imaging currents (*continuous*, *interleaved with rest*, *interleaved with positive*) are shown in **Figure 7.5**. φ_d images appear largely similar across inhalation media and imaging currents. Small differences were noted between air and carbogen traces of φ_d and $\nabla^2\varphi_d$. As expected, changes in φ_d were amplified in Laplacian of φ_d (i.e. $\nabla^2\varphi_d$).

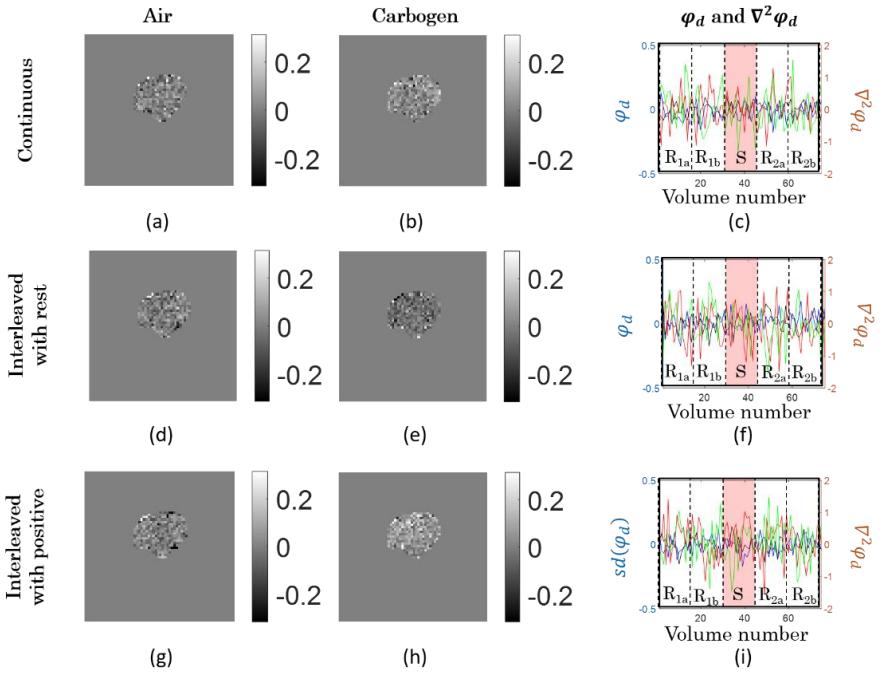

Figure 7.5: Phase difference ($\boldsymbol{\varphi_d}$) images under forepaw stimulation and (a) *air - continuous*, (b) *carbogen - continuous*, (d) *air - interleaved with rest*, (e) *carbogen - interleaved with rest*, (g) *air - interleaved with positive*, (h) *carbogen - interleaved with positive* combinations of media and hippocampal imaging currents. Progression of fMREIT $\boldsymbol{\varphi_d}$ and $\boldsymbol{\nabla^2\varphi_d}$ over imaging volumes shown in (c), (f) and (i) during *continuous*, *interleaved with rest* and *interleaved with positive* imaging currents. Each functional scan consists of *active* ($\boldsymbol{S}$) and *rest* ($\boldsymbol{R_{1a}}$, $\boldsymbol{R_{1b}}$, $\boldsymbol{R_{2a}}$, $\boldsymbol{R_{2b}}$) periods. $\boldsymbol{\varphi_d}$ under *air* is shown in black and under *carbogen* in blue. $\boldsymbol{\nabla^2\varphi_d}$ under *air* is shown in green and under *carbogen* in red.

C. Standard deviation of phase difference (φ_d) and Laplacian of phase difference ($\nabla^2\varphi_d$)

Standard deviations of φ_d and $\nabla^2\varphi_d$ images per volume in the whole brain, contralateral cortical and ipsilateral cortical brain regions are shown in **Figure 7.6**. Across all three imaging current waveforms, standard deviations of φ_d and $\nabla^2\varphi_d$ in *air* and *carbogen* media were similar. Larger contralateral

standard deviations of φ_d and $\nabla^2\varphi_d$ traces were observed compared to ipsilateral cortical masks, as the cortical region contralateral to forepaw stimulation was closest to the imaging electrode.

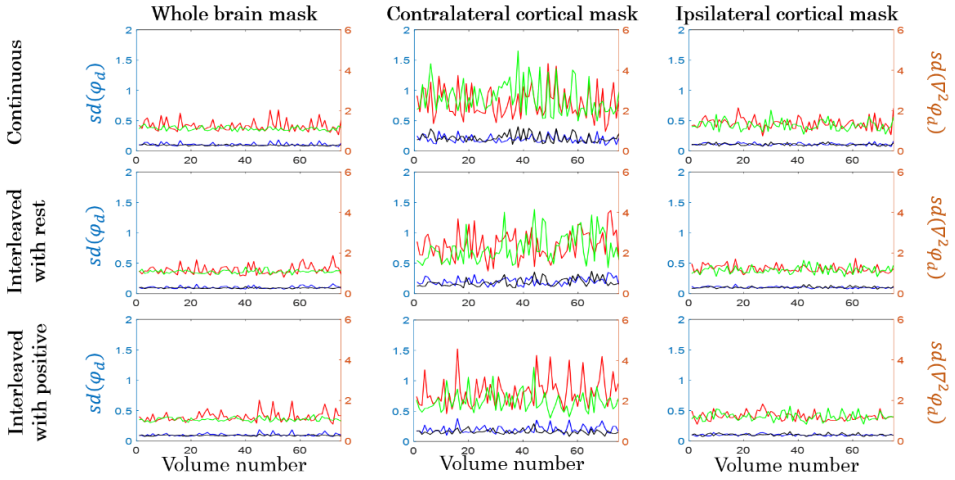

Figure 7.6: Standard deviation of phase difference ($\boldsymbol{sd(\varphi_d)}$) and Laplacian of phase difference ($\boldsymbol{sd(\nabla^2\varphi_d)}$) in the whole brain, contralateral cortical and ipsilateral cortical masks. $\boldsymbol{sd(\varphi_d)}$ under *air* is shown in black and under *carbogen* is shown in blue. $\boldsymbol{sd(\nabla^2\varphi_d)}$ under *air* is shown in green and under *carbogen* is shown in red.

D. Contemporaneous fMRI/fMREIT activation maps

Magnitude and phase portions of complex functional imaging datasets were processed to produce fMRI and fMREIT activation maps respectively. **Figure 7.7** shows the fMRI and fMREIT activation maps for imaging experiments performed under *air* medium and *interleaved with rest* hippocampal imaging currents. Four fMREIT activation maps were processed to compare the variance in φ_d between *active* and *rest* periods using voxel-wise F-tests with $p < 0.05$.

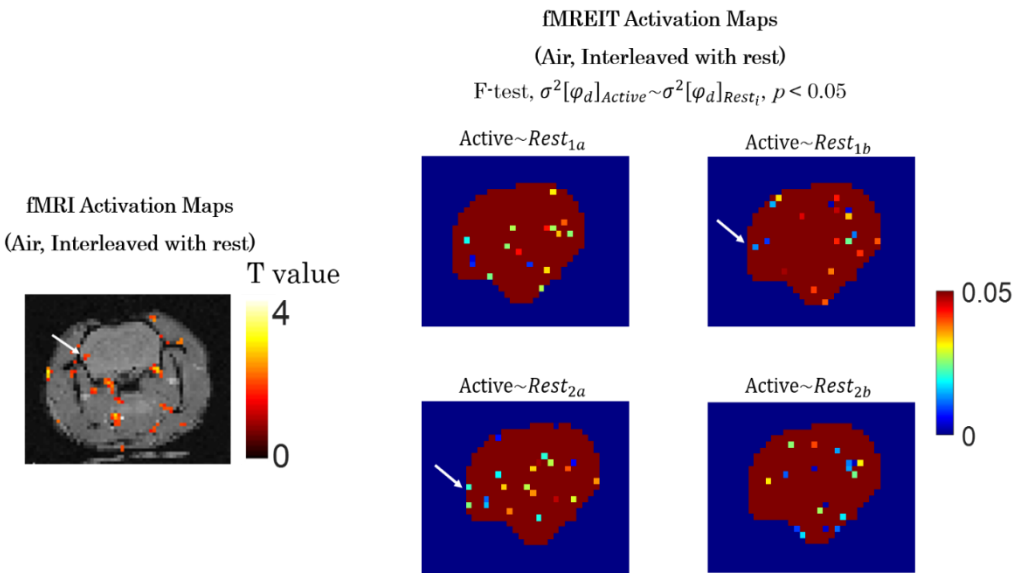

Figure 7.7: fMRI and fMREIT activation maps for SE-EPI acquisitions during *air* medium and *interleaved with rest* hippocampal imaging current. fMREIT maps show comparisons between *active* and four *rest* periods. Significant differences between *active* and each *rest* period is shown with $p < 0.05$. White arrows in BOLD map show somatosensory activations, and those in fMREIT maps show approximate location of somatosensory cortex.

The fMRI activation map in **Figure 7.7** shows a cluster of active voxels (white arrow) in the somatosensory region contralateral to the site of forepaw stimulation. fMREIT activation maps show active voxels spread across the brain during all four rest periods. fMREIT maps for $Active \sim Rest_{1b}$ and $Active \sim Rest_{2a}$ comparisons show activity (white arrows) in locations matched with BOLD activations that are likely coincidental due to the similar activations observed across the brain. Similar observations are noted during $Active \sim Rest_{1b}$ and $Active \sim Rest_{2a}$ comparisons in **Figure 7.8**, under *carbogen* medium and *interleaved with rest* hippocampal imaging currents.

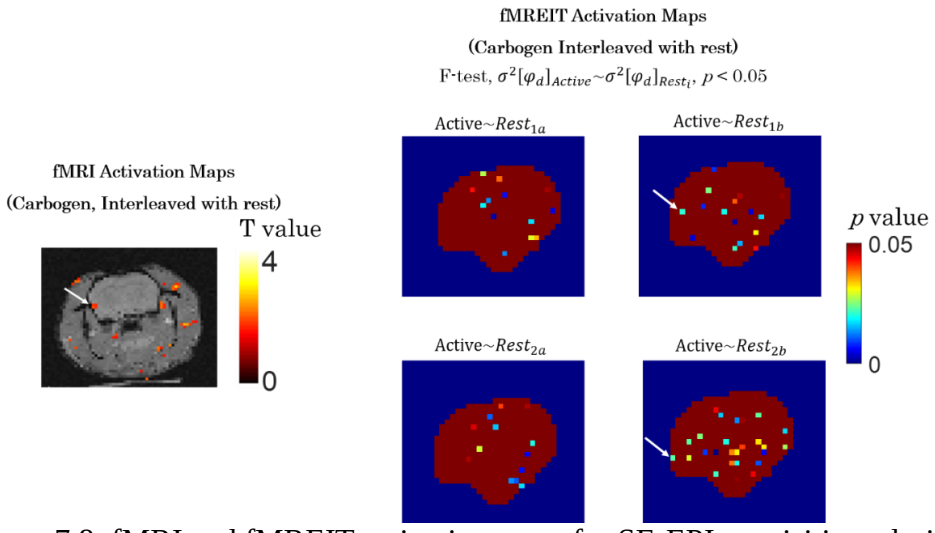

Figure 7.8: fMRI and fMREIT activation maps for SE-EPI acquisitions during *carbogen* medium and *interleaved with rest* hippocampal imaging current. fMREIT maps show comparisons between *active* and four *rest* periods. Significant differences between *active* and each *rest* period is shown with $p < 0.05$. White arrows in BOLD map show somatosensory activations, and those in fMREIT maps show approximate location of somatosensory regions.

Figure 7.9 and **Figure 7.10** show fMRI and fMREIT activation maps for all combinations of inhalation medium – *air* and *carbogen* – and hippocampal imaging currents – *continuous, interleaved with rest* and *interleaved with positive*. fMREIT maps are shown for rest periods that are temporally adjacent to forepaw stimulation – $Rest_{1b}$ and $Rest_{2a}$ periods.

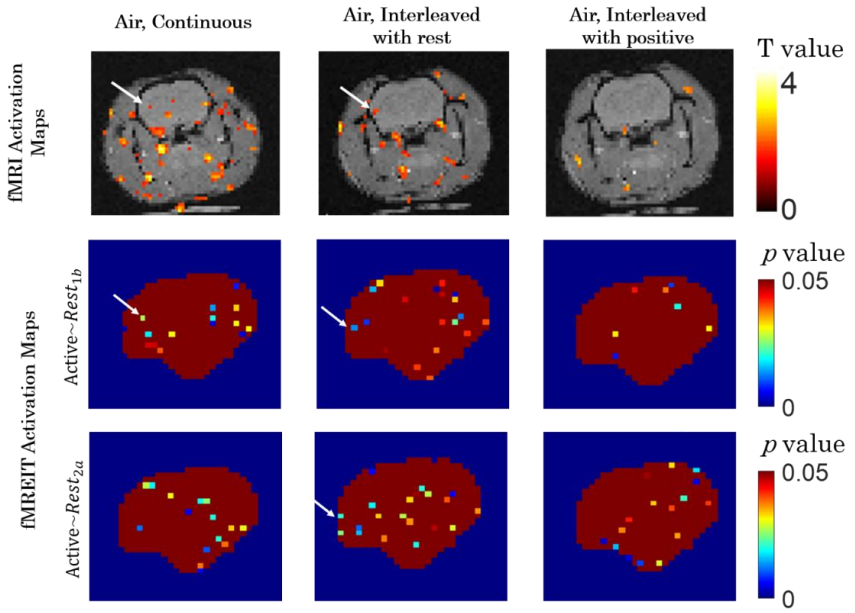

Figure 7.9: fMRI and fMREIT activation maps during *air* medium and three distinct hippocampal imaging current waveforms – *continuous*, *interleaved with rest* and *interleaved with positive*. fMREIT maps show comparisons between *active* and two *rest* periods immediately adjacent to forepaw stimulation period. White arrows in fMRI activation maps show somatosensory activations, and in fMREIT shows the approximate location of somatosensory cortex. Significant differences between *active* and each *rest* period is shown with $p < 0.05$.

BOLD activations found during *continuous* and *interleaved with rest* currents under *air* (**Figure 7.9**) sustained in *carbogen* (**Figure 7.10**) for *interleaved with rest* only. BOLD activations were not found during *interleaved with positive* imaging currents. fMREIT maps showed active voxels dispersed across the brain irrespective of inhalation medium and hippocampal imaging currents.

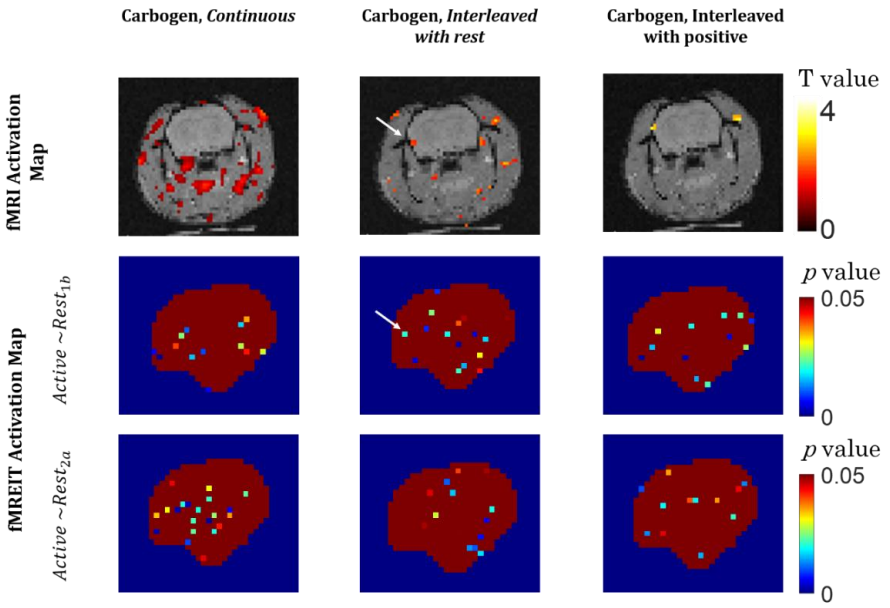

Figure 7.10: fMRI and fMREIT activation maps during *carbogen* medium and three distinct hippocampal imaging current waveforms – *continuous*, *interleaved with rest* and *interleaved with positive*. fMREIT maps show comparisons between *active* and two *rest* periods immediately adjacent to forepaw stimulation period. White arrows show approximate locations of the somatosensory cortex in fMREIT maps, and somatosensory activations in fMRI maps. Significant differences between *active* and each *rest* period is shown with $p < 0.05$.

E. Statistical significance in fMREIT activation maps in *air* and *carbogen* medium

F-tests performed on φ_d and $\nabla^2\varphi_d$ images within cortical and non-cortical masks were constructed as fMREIT activation maps. Significant voxels ($p < 0.05$) between *active* and four *rest* time-periods were counted for *air* and *carbogen* media. Significant number of voxels under *air* exceeds *carbogen* in both cortical and non-cortical masks as shown in **Figure 7.11**.

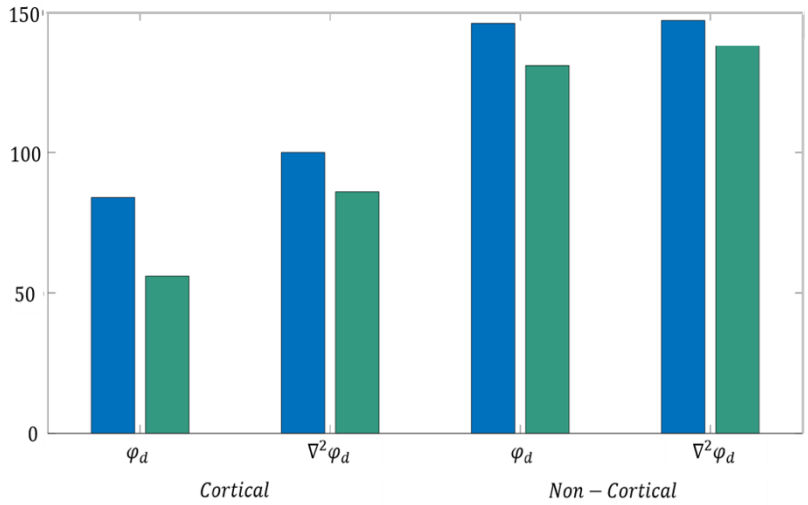

Figure 7.11: Numbers of statistically significant voxels (F-test, $p < 0.05$) in phase difference ($\boldsymbol{\varphi_d}$) and Laplacian of phase difference ($\boldsymbol{\nabla^2\varphi_d}$) under *air* (blue) and *carbogen* (green) media within cortical and non-cortical masks.

F-tests across φ_d images volume between *active* and *rest* time-periods yielded significant differences between *air* and *carbogen* media as shown in **Figure 7.12**. Similar to the trend observed in **Figure 7.11**, the number of significant voxels in *air* exceeds *carbogen*.

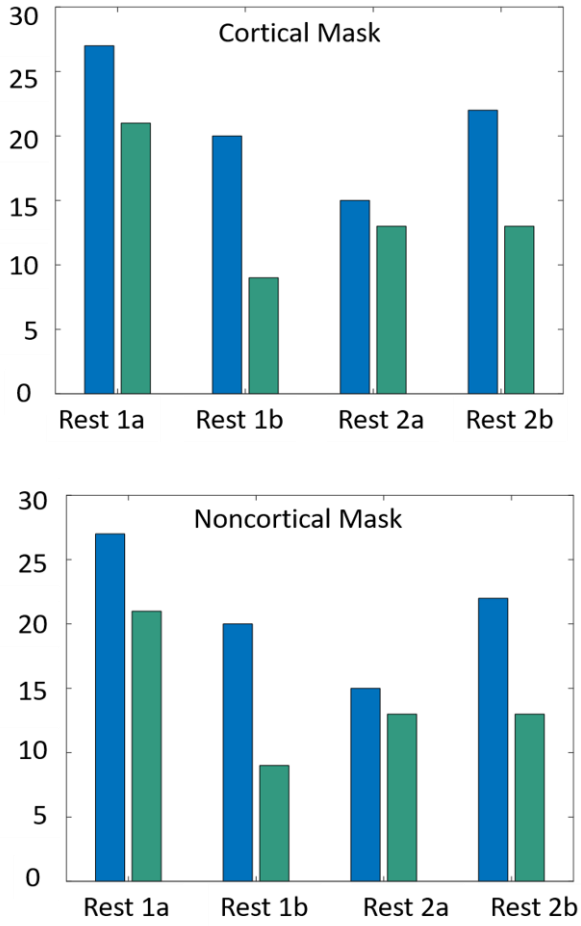

Figure 7.12: Total numbers of statistically significant voxels identified by F-tests ($p < 0.05$) of phase difference ($\boldsymbol{\varphi_d}$) between *active* and four *rest* time-periods within cortical and non-cortical masks. *Air* is represented with blue bars and *carbogen* with green.

F. Differential neural activity in fMREIT activation maps across brain regions

Active voxels identified in fMREIT activation maps were categorized into distinct brain regions – contralateral cortical, ipsilateral cortical, cortical, non-cortical and whole brain masks. Similar activation maps (i.e. MREIT activation maps) were constructed for functional imaging experiments without forepaw stimulation to assess baseline MREIT activations. Total number of

fMREIT active voxels in each brain region during combinations of inhalation medium – *air* and *carbogen* – and hippocampal imaging currents – *continuous*, *interleaved with rest* and *interleaved with positive* were assessed relative to corresponding baseline MREIT active voxel counts. **Figure 7.13** shows increases in fMREIT active voxels within contralateral cortical masks compared to baseline MREIT contralateral activations during *continuous* (φ_d) and *interleaved with positive* (φ_d) imaging currents under *air*.

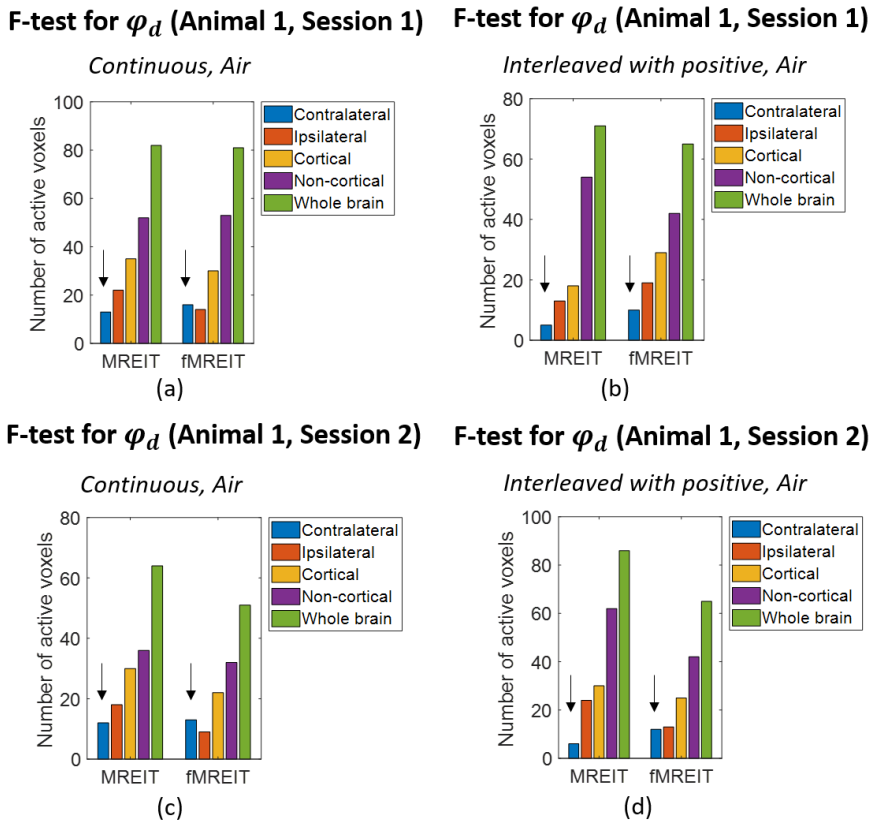

Figure 7.13: Active voxels in MREIT contralateral cortical regions from baseline MREIT activation maps and fMREIT contralateral cortical regions from fMREIT activation maps under *air*. Contralateral cortical (blue) and ipsilateral cortical (orange) regions are combined to form the cortical region (yellow). Cortical and non-cortical regions (purple) together form the whole brain (green) region. Black arrows indicate relative active voxel count

increases in fMREIT contralateral cortical regions compared to MREIT contralateral regions.

Under *carbogen, interleaved with positive* imaging currents showed increases in contralateral active voxel counts in fMREIT φ_d and $\nabla^2\varphi_d$ relative to MREIT counts as shown in **Figure 7.14**. Increases in contralateral fMREIT active voxels relative to corresponding contralateral MREIT active voxel counts indicated increases in differential neural activity coincident with forepaw stimulation. Non-cortical regions showed larger number of active voxels compared to cortical regions under *air* and *carbogen*.

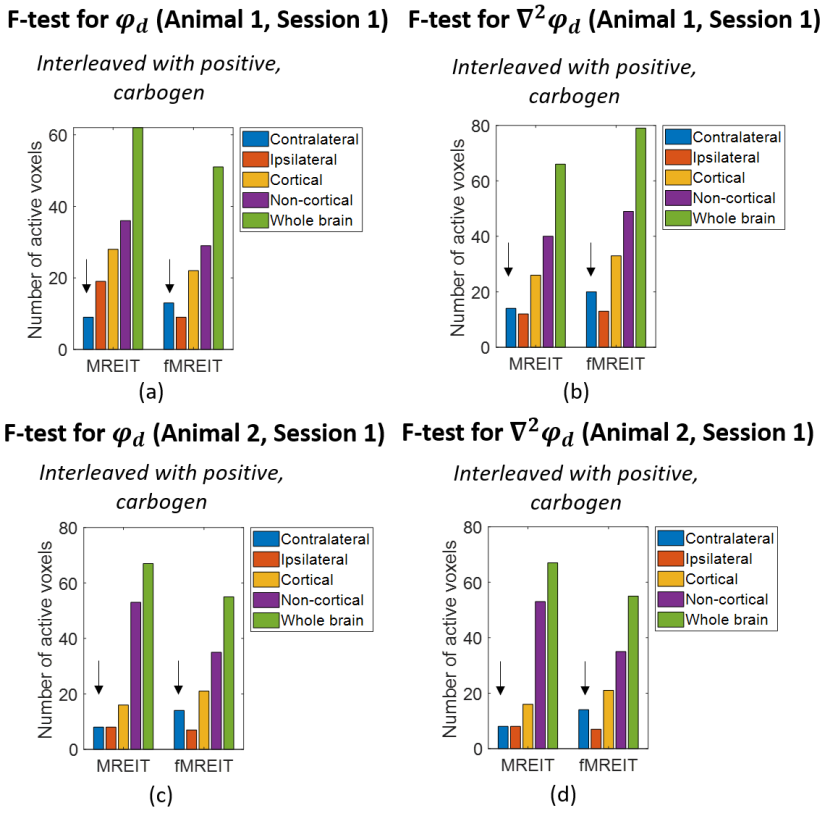

Figure 7.14: Active voxels in MREIT contralateral cortical regions from baseline MREIT activation maps and fMREIT contralateral cortical regions

from fMREIT activation maps under *carbogen*. Contralateral cortical (blue) and ipsilateral cortical (orange) regions are combined to form the cortical region (yellow). Cortical and non-cortical regions (purple) together form the whole brain (green) region. Black arrows indicate relative active voxel count increases in fMREIT contralateral cortical regions compared to MREIT contralateral regions.

Contralateral fMREIT activations were found to exceed corresponding ipsilateral fMREIT activations during *continuous* (φ_d) and *interleaved with positive* ($\nabla^2\varphi_d$) imaging currents under *air* as shown in **Figure 7.15**. Applying forepaw stimulation suppressed ipsilateral activations in all fMREIT ipsilateral masks except for **Figure 7.15(d)**. MREIT maps were not available for **Figure 7.15(c)** because MREIT data was not collected.

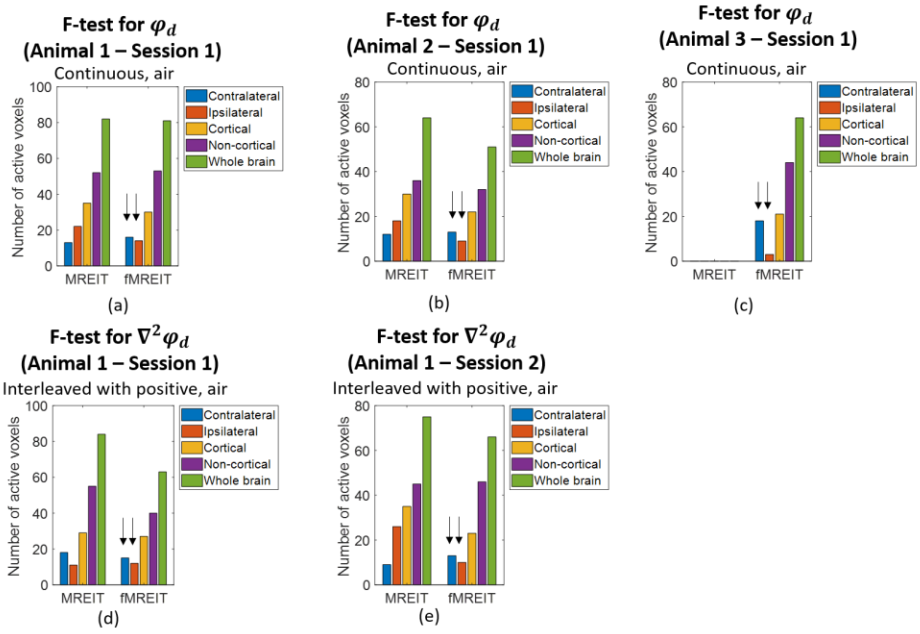

Figure 7.15: Active voxels in fMREIT contralateral and fMREIT ipsilateral cortical regions under *air*. Contralateral cortical (blue) and ipsilateral cortical (orange) regions are combined to form the cortical region (yellow). Cortical and non-cortical regions (purple) together form the whole brain (green) region. Black arrows indicate relative active voxel count increases in fMREIT contralateral cortical regions compared to fMREIT ipsilateral cortical regions.

fMREIT activations in contralateral cortical regions under *carbogen* exceeded corresponding ipsilateral regions during *continuous* (φ_d), *interleaved with rest* (φ_d , $\nabla^2\varphi_d$) and *interleaved with positive* (φ_d, $\nabla^2\varphi_d$) imaging currents under *carbogen* as shown in **Figure 7.16**. MREIT data in **Figures 7.16(e, i)** was not collected. **Figures 7.16(d,f,j)** showed larger or similar MREIT contralateral activations compared to corresponding ipsilateral activations before forepaw stimulation was applied. These MREIT contralateral activations were further increased compared to ipsilateral activations with the application of forepaw stimulation, as demonstrated in the corresponding fMREIT contralateral activations.

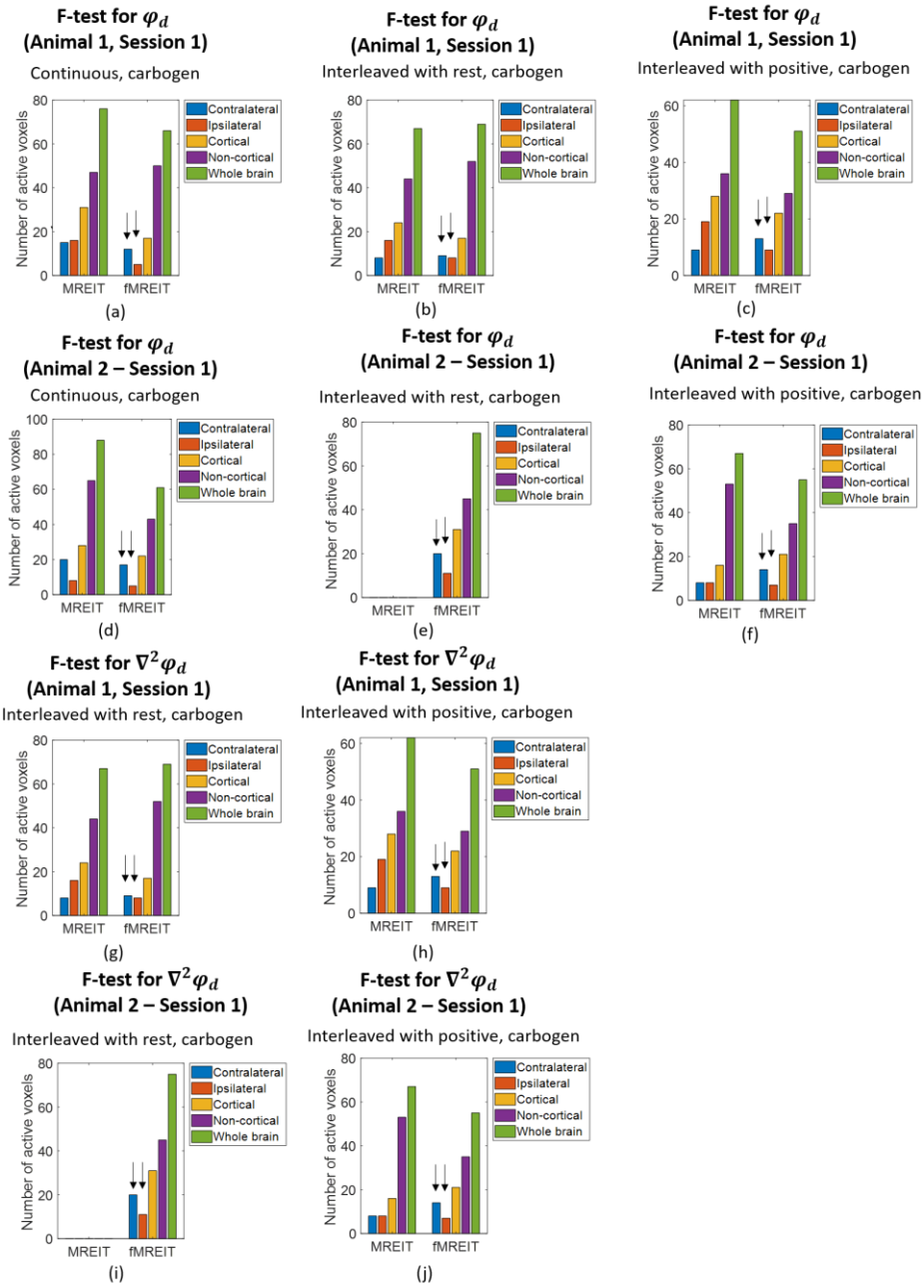

Figure 7.16: Active voxels in fMREIT contralateral and fMREIT ipsilateral cortical regions under *carbogen*. Contralateral cortical (blue) and ipsilateral cortical (orange) regions are combined to form the cortical region (yellow). Cortical and non-cortical regions (purple) together form the whole brain (green) region. Black arrows indicate relative active voxel count increases in fMREIT contralateral cortical regions compared to fMREIT ipsilateral cortical regions.

7.4 Discussion

fMRI and fMREIT datasets are analyzed across imaging current waveforms (c*ontinuous, interleaved with rest, interleaved with positive*) and hemodynamic conditions (*air, carbogen*) to produce fMRI and fMREIT activation maps. Similarities and dissimilarities between both maps were assessed across imaging current types and inhalation media.

fMREIT as a functional imaging technique needs the administration of imaging currents to encode conductivity changes in MR phase. Imaging currents were delivered directly into the hippocampus using carbon electrodes, as described in **Chapter 5**. The hippocampus was chosen as the carbon electrode implantation site due to its proximity to the somatosensory cortex. Electrical stimulation of a rat forepaw was used to induce neural activity in the contralateral somatosensory cortex. fMRI BOLD imaging was used to confirm the activation of somatosensory areas, and to assess the effect of imaging currents applied separately and simultaneously with forepaw stimulation on BOLD signals.

To validate neural activity induced by forepaw stimulation, functional imaging experiments were conducted without imaging currents to remove the influence of imaging currents on active neurons. BOLD maps in **Figure 7.2** show the classic somatosensory area I (SAI) and somatosensory area II (SAII) activation due to forepaw stimulation under *air*. These SAI and SAII activations are in agreement

with BOLD fMRI studies using forepaw stimulation of rodents [140, 141]. While maintaining all imaging conditions the same except for the medium, the somatosensory activations were not visible under *carbogen*. The absence of activity in the brain under *carbogen* contradicts those reported in other rodent fMRI studies [61]. The spatial extent of BOLD signals were smaller under *air* in **Figure 7.2** possibly due to the use of forepaw stimulation parameters - 2 mA amplitude, 0.3 ms pulse width and 3 Hz frequency - compared to 4 mA amplitude, 0.3 ms pulse width and 9 Hz frequency [61]. As an additional measure to ensure somatosensory activity was due to forepaw stimulation, functional imaging was performed without forepaw stimulation. As expected, neural activity was absent in the brain as shown in **Figure 7.3**. The absence of neural activity without forepaw stimulation further emphasizes the causal link between forepaw stimulation and somatosensory activation.

Interaction between imaging currents and forepaw electrical stimulation was assessed by delivering imaging currents during the entire scan whereas forepaw stimulation was administered using a block design with well-defined 'on' and 'off' periods. **Figure 7.4** demonstrates the influence of imaging current waveforms on BOLD signals. When *continuou*' imaging currents were applied, SAI activation was observed. The SAI activation could not be found under *carbogen* and *continuous* imaging current. During *interleaved with rest*, minor SAII activation was noted under *air* and *carbogen* conditions. During both *air* and *carbogen*

media, BOLD activation was not found during *interleaved with positive* imaging current delivery. False positive activations noted in regions outside the brain in BOLD maps are commonly observed in fMRI studies due to random noise, statistical issues related to thresholding, clustering and improper estimation of *p*-values, physiological signals such as cardiac and respiratory signals [142]. BOLD signal magnitudes and BOLD activation areas are known to decrease under *carbogen* compared to *air* [61], and therefore increasing the spatial extent of somatosensory activations under *air* may aid in sustaining at least some of the active voxels under *carbogen*. Future *in vivo* experiments must focus on optimizing forepaw stimulation parameters for each imaging current waveform and inhalant. Overall, interaction between imaging currents, forepaw stimulation and medium may have influenced BOLD signals.

fMREIT experiments were conducted using three distinct imaging current waveforms - *continuous*, *interleaved with rest* and *interleaved with positive*. Expected magnitude of φ_d values were 0, $\gamma B_z T_C$ and $2\gamma B_z T_C$ for *continuous*, *interleaved with rest* and *interleaved with positive* imaging current waveforms. However, magnitudes of measured φ_d traces in a representative contralateral cortical 'brain' voxel showed similar range of φ_d and $\nabla^2\varphi_d$ values across current waveforms as shown in **Figure 7.5(c,f,i)**. φ_d and $\nabla^2\varphi_d$ traces were similar between *air* and *carbogen* media across imaging current waveforms, potentially

substantiating the minimal influence of medium and imaging current type on fMREIT φ_d signals generated by underlying tissues in the voxel.

Variations in φ_d and $\nabla^2\varphi_d$ within cortical regions that were contralateral and ipsilateral to forepaw stimulation were compared in **Figure 7.6**. Contralateral cortical regions were expected to show larger standard deviations in φ_d and $\nabla^2\varphi_d$ due to forepaw stimulation induced neural activity in somatosensory areas. As expected, larger contralateral standard deviations in φ_d and $\nabla^2\varphi_d$ were observed compared to ipsilateral cortical regions. As the imaging current delivery electrode was positioned closer to contralateral cortical regions and forepaw stimulation was targeted to activate contralateral somatosensory neurons, the observed larger φ_d and $\nabla^2\varphi_d$ variations in contralateral cortical regions are consistent with the site of forepaw stimulation.

Conductivity contributions from nearby vascular networks unrelated to neural activity were expected to obscure fMREIT φ_d signals. *Carbogen* was used as an inhalation medium to reduce BOLD signal sensitivity to vascular changes [61]. Using *air* or *carbogen* as inhalation medium seemed to minimally influence fMREIT φ_d signals as shown in **Figure 7.6**. Although previous studies have shown *carbogen* to minimize the contribution of vascular mechanisms on BOLD signals, there is a gap in the literature about the effect of *carbogen* on MR phase signals. Due to inherent differences in contrast mechanisms generating BOLD and

fMREIT signals, the influence of *carbogen* on fMREIT signals may be different from BOLD signals. Reduction in BOLD activations under *carbogen* is evident from **Figure 7.4**, thereby demonstrating the desensitization of BOLD signals to vascular changes under *carbogen*. However, the seemingly minimal impact of *carbogen* on fMREIT φ_d signals as shown in **Figure 7.5** and **Figure 7.6** suggest the influence of *carbogen*, if any, was insufficient at 7 T, and may need further investigation at higher field strengths.

Contemporaneous fMRI/fMREIT activation maps allow the simultaneous identification of active voxels from both fMRI and fMREIT. **Figure 7.7** and **Figure 7.8** show the fMRI and fMREIT activation maps of imaging performed under *air* and *carbogen* respectively. On the whole, fMREIT maps identified larger number of active voxels across the brain whereas fMRI maps showed a smaller number of active voxels localized in the contralateral somatosensory region. Therefore, fMREIT activation maps lacked the spatial specificity of fMRI maps, however, some instances of similarly active voxels were noted during $Rest_{1b}$ and $Rest_{2a}$ time-periods. As $Rest_{1b}$ and $Rest_{2a}$ time-periods were temporally adjacent to the period of forepaw stimulation, fMREIT maps comparing stimulation periods with $Rest_{1b}$ and $Rest_{2a}$ periods may yield useful comparisons. fMREIT maps for all combinations of inhalation medium – *air* and *carbogen* – and hippocampal imaging currents – *continuous*, *interleaved with rest* and *interleaved with positive* shown in **Figure 7.9** and **Figure 7.10** demonstrate

active voxels during $Rest_{1b}$ and $Rest_{2a}$ dispersed across the brain with some active voxels coincident with BOLD activations. Location-matched active voxels in fMREIT activation maps with BOLD activations may be purely coincidental as fMREIT maps showed active voxels in both stimulated and non-stimulated brain regions. Other rest periods – $Rest_{1a}$ and $Rest_{2b}$ – showed similar spatial distributions of active voxels, and could reflect differential changes in φ_d due to noise, physiological changes and conductivity changes unrelated to forepaw stimulation. On the whole, active voxels identified in fMREIT activation maps may reflect statistically significant regions of differential activity between *active* and *rest* periods related to physiological signal sources such as respiration and cardiac rhythms.

Cumulative statistical t-tests and F-tests of φ_d and $\nabla^2\varphi_d$ were conducted between *active* and *rest* periods in cortical and non-cortical regions of the brain. Voxels coincident with statistically significant differences ($p < 0.05$) between active and rest periods were identified as sites of neural activation. Statistically significant differences between the average of $\nabla^2\varphi_d$ during *active* and *rest* periods were not found, as noise levels in $\nabla^2\varphi_d$ were larger than neural activity related fMREIT φ_d signal changes. F-tests of φ_d and $\nabla^2\varphi_d$ ($p < 0.05$) were used to compare variance in fMREIT φ_d signals during *active* and *rest* periods. Owing to the relatively smaller size of cortical mask, the total number of voxels in the cortical mask was lesser than the non-cortical mask, as shown in **Figure 7.11** and **Figure 7.12**. As

expected, both masks showed larger number of active voxels under *air* compared to *carbogen* medium, thereby implying larger apparent activations in the neural tissue coincident with active voxels. Larger apparent activations under *air* indicate larger variability in φ_d and $\nabla^2\varphi_d$. Previous studies have shown *carbogen* to cause venous saturation, and therefore desensitize MR magnitude signals to the presence of blood [60, 61]. Due to the lack of studies assessing the impact of *carbogen* on MR phase signals, the reduced number of active voxels under *carbogen* in **Figure 7.11** and **Figure 7.12** may have occurred due to factors other than blood saturation due to *carbogen*. If *carbogen* is assumed to have a similar desensitizing influence on MR phase signals as with MR magnitude signals, then active voxels in fMREIT maps under *carbogen* indicate conductivity changes related to neural activity and potentially other non-vascular physiological signals.

Regions of differential neural activity during functional imaging experiments without forepaw stimulation could provide a baseline measure for the active voxels identified in fMREIT activation maps. fMREIT activation maps during functional experiments without forepaw stimulation, also known as MREIT activation maps, are summarized over distinct brain regions – contralateral cortical, ipsilateral cortical, cortical, non-cortical and whole brain regions as shown in **Figure 7.13 – Figure 7.16**. Overall, active voxel counts in non-cortical mask exceeded cortical mask potentially due to larger size of non-cortical mask and the presence of underlying tissue heterogeneity. To mitigate contributions to

conductivity changes from physiological mechanisms not related to forepaw stimulation and inherent conductivity differences due to tissue heterogeneity, the cortical region was divided into contralateral and ipsilateral cortical regions. Forepaw stimulation was found to boost contralateral fMREIT activations over corresponding contralateral MREIT activations during *continuous* (φ_d) and *interleaved with positive* (φ_d) imaging currents under *air* as shown in **Figure 7.13**. Similar contralateral fMREIT activation increases were only found during *interleaved with positive* ($\varphi_d, \nabla^2\varphi_d$) imaging currents under *carbogen* as shown in **Figure 7.14**. fMREIT active voxel count increases in cortical masks contralateral to the site of forepaw stimulation above baseline MREIT active voxel counts were consistent with expected increases in standard deviations of φ_d during forepaw stimulation. Therefore, the effect of forepaw stimulation on contralateral somatosensory neurons was evident as larger activations in contralateral fMREIT cortical regions compared to baseline contralateral MREIT activations during *continuous* and *interleaved with positive* imaging currents.

Somatosensory neurons in the contralateral cortical mask were activated during forepaw stimulation as demonstrated by BOLD maps in **Figure 7.4**. Similar contralateral cortical regions showed larger fMREIT activations compared to corresponding ipsilateral cortical regions during *continuous* (φ_d) and *interleaved with positive* ($\nabla^2\varphi_d$) imaging currents under *air* as shown in **Figure 7.15**. Under *carbogen*, all three imaging current types – *continuous* (φ_d), *interleaved with rest*

($\varphi_d, \nabla^2\varphi_d$) and *interleaved with positive* ($\varphi_d, \nabla^2\varphi_d$) showed increased fMREIT contralateral cortical activity relative to ipsilateral regions as demonstrated in **Figure 7.16**. Larger differential neural activity in contralateral cortical regions compared to ipsilateral regions were consistent with the site of forepaw stimulation, and substantiates the possibility of detecting neural activity in *in vivo* settings using fMREIT.

Preliminary findings of *in vivo* functional imaging experiments using fMREIT demonstrated the potential of fMREIT to detect neural activity under *air* or *carbogen* as inhalation medium. Under *air*, *continuous* and *interleaved with positive* imaging currents showed larger fMREIT activations compared to baseline MREIT activations in cortical regions contralateral to the site of forepaw stimulation. Furthermore, *continuous* and *interleaved with positive* imaging currents showed increased contralateral fMREIT activations compared to ipsilateral cortical regions. Under *carbogen*, *interleaved with positive* imaging currents showed larger contralateral fMREIT activations compared to baseline MREIT and corresponding ipsilateral cortical regions. In conclusion, the choice of medium will influence the hippocampal imaging current type best suited to yield the detection of differential neural activity induced by forepaw stimulation as fMREIT activations above baseline.

To overcome the limitations of the preliminary *in vivo* functional imaging study, future *in vivo* functional imaging experiments must include respiratory and cardiac gating to remove the influence of respiratory and cardiac cycles on MR phase. Blood flow imaging under *air* and *carbogen* may be useful to model blood flow effects on fMREIT φ_d and confirm BOLD signal saturation under *carbogen*. Electrophysiological recording of stimulated neural tissue during fMREIT imaging acquisitions may be useful to correlate MR phase signals with real-time neural signals. In addition to these experimental design improvements, the use of larger sample sizes and higher-order statistical analyses may improve the spatial specificity of fMREIT activation maps, and provide a rigorous framework to establish the *in vivo* detection of neural activity using fMREIT.

7.5 Conclusion

Contralateral somatosensory cortical activations due to forepaw stimulation were confirmed by BOLD activation maps. fMREIT activation maps detected active voxels (F-tests of φ_d and $\nabla^2\varphi_d$, $p < 0.05$) throughout the brain including the stimulated contralateral cortical region. Preliminary findings in small sample sizes demonstrate the potential of fMREIT to detect neural activity *in vivo* under air – during *continuous* and *interleaved with positive* imaging currents – and under carbogen – during *continuous*, *interleaved with positive* and *interleaved with rest* imaging currents. Although consistently larger contralateral cortical activations were noted, more rigorous experimentation across larger samples sizes and

higher-order statistical analyses of fMREIT φ_d signals are needed to establish the *in vivo* proof of concept of neural activity detection using fMREIT.

8. CONCLUSIONS AND FUTURE DIRECTIONS

Technological gaps in the use of fMREIT for neurological applications, and preclinical translation of fMREIT from the most recent *in vitro* studies were addressed with the development of carbon electrodes for imaging current delivery. The MR properties of the newly developed carbon electrodes were compared with gold standard Pt-Ir neural stimulation electrodes, for use at high MR fields. Smaller MR artifacts and lesser heating of carbon electrodes compared to Pt-Ir counterparts rendered carbon suitable for MR-compatible imaging and current delivery. These electrodes were later implanted in rodent hippocampi for fMREIT-based imaging of neural activity.

An *in vivo* model comprising of carbon electrodes implanted into rodent hippocampi at 50^{o} dorsoventral inclination for the delivery of MREIT imaging currents along with subcutaneous forepaw electrical stimulation was proposed for the preclinical translation of fMREIT. Magnetic field perturbations in cortical regions, particularly the somatosensory cortex, under forepaw electrical stimulation was mapped based on stimulation-induced membrane conductance changes that ultimately led to changes in MREIT imaging current pathways. A detailed fMREIT analysis pipeline was developed to compute fMREIT activation maps to identify active brain regions. These fMREIT activation maps were compared with fMRI activation maps to distinguish primary conductivity-related activations from secondary hemodynamic contributions. fMRI

activation maps consistently showed somatosensory activation, thereby substantiating the activation of somatosensory neurons due to forepaw stimulation. Consistent somatosensory activations were observed in fMREIT maps, however, larger number of significantly active voxels were found in non-cortical regions. Conductivity changes induced by forepaw stimulation could have been obscured by other physiological signals, thereby compromising the spatial specificity of fMREIT activation maps.

Preliminary findings of *in vivo* functional imaging experiments using fMREIT demonstrated the potential of fMREIT to detect neural activity. Choice of inhalation medium, *air* or *carbogen*, influenced the imaging current waveform best suited to detect neural activity induced by forepaw stimulation. Under *air*, contralateral somatosensory activations were noted during *continuous* and *interleaved with positive* imaging currents, whereas *carbogen* medium showed contralateral somatosensory activations during all three current imaging types – *continuous, interleaved with rest* and *interleaved with positive*. These preliminary findings demonstrate the potential of fMREIT to detect neural activity *in vivo*, however further experimentation is needed to confirm these observations across larger sample sizes.

The research work presented here is a preliminary *in vivo* study investigating the feasibility of *in vivo* neural activity detection using fMREIT. Several technological challenges such as the development of carbon electrodes for internal imaging current delivery and an *in vivo* animal model for functional imaging as well as the design and

analysis of contemporaneous fMRI/fMREIT experiments were addressed through the course of the doctoral research work. Future *in vivo* work will benefit from implementing strategies that perform electrophysiological recording of neural activity, monitor physiological signals, and improve SNR of fMREIT phase signals. Additional preliminary experiments, including cerebral blood flow mapping, must be conducted to assess the impact of *carbogen* on fMREIT phase measurements compared to *air* delivered as an inhalation medium. These studies may inform the optimization of forepaw stimulation parameters to ensure somatosensory cortical activations under both *air* and *carbogen* media. To improve the possibility of detecting neural activity using fMREIT, strategies such as using higher B_0 field strengths, improving magnetic field homogeneity using shimming and larger voxel size must be undertaken. The time-resolution of fMREIT experiments was ~6 seconds, which was 2× longer than fMRI under similar imaging parameters demonstrates the necessity for faster imaging sequences to map neural activity. Clinical translation of research findings from *in vivo* fMREIT rodent studies must be used carefully considered to scale for neuroanatomical and neurophysiological differences between human and rodent brains, and may require validation in primates, or may potentially involve direct testing in humans.

REFERENCES

[1] R. Brette, A. Destexhe. Handbook of Neural Activity Measurement. United Kingdom: Cambridge University Press, 2012.

[2] S. Ogawa, T. M. Lee, A. R. Kay, D. W. Tank. Brain magnetic resonance imaging with contrast dependent on blood oxygenation. Proc Natl Acad Sci U S A 1990;87: 9868-72.

[3] R. J. Sadleir, S. C. Grant, E. J. Woo. Can high-field MREIT be used to directly detect neural activity? Theoretical considerations. Neuroimage 2010;52:205-16.

[4] R. J. Sadleir, F. Fu, C. Falgas, S. Holland, M. Boggess, S. C. Grant*, et al.* Direct detection of neural activity in vitro using magnetic resonance electrical impedance tomography (MREIT). Neuroimage 2017;161:104-119.

[5] R. J. Sadleir, F. Fu, M. Chauhan. Functional magnetic resonance electrical impedance tomography (fMREIT) sensitivity analysis using an active bidomain finite-element model of neural tissue. Magn Reson Med 2019; 81(1):602-14.

[6] F. Fu. Ultrahigh Field Functional Magnetic Resonance Electrical Impedance Tomography (fMREIT) in Neural Activity Imaging. Arizona State University, Arizona, 2019.

[7] E. R. Kandel, W. A. Spencer, F. J. Brinley, Jr. Electrophysiology of hippocampal neurons. I. Sequential invasion and synaptic organization. J Neurophysiol 1961;24:225-42.

[8] J. G. Bernstein, E. S. Boyden. Optogenetic tools for analyzing the neural circuits of behavior. Trends Cogn Sci 2011;15:592-600.

[9] B.A. MacVicar, T.W.Watson, F.E. LeBlanc, S.G.Borg,P.Federico. Mapping of Neural Activity Patterns Using Intrinsic Optical Signals: From Isolated Brain Preparations to the Intact Human Brain. Adv Exp Med Biol 1993; 333:71-9.

[10] E. M. C. Hillman. Optical brain imaging in vivo: techniques and applications from animal to man. J Biomed Opt 2007;12(5):051402.

[11] M. Hamalainen, R. Hari, R. J. Ilmoniemi, J. Knuutila, O. V. Lounasmaa. Magnetoencephalography---theory, instrumentation, and applications to noninvasive studies of the working human brain. Rev Mod Phys 1993;65(2):413-97.

[12] W. J. Freeman, R. Kozma. Local-global interactions and the role of mesoscopic (intermediate-range) elements in brain dynamics. Behav Brain Sci 2000;23(3):401-401.

[13] T. Nara, J. Oohama, M. Hashimoto, T. Takeda, S. Ando. Direct reconstruction algorithm of current dipoles for vector magnetoencephalography and electroencephalography. Phys Med Biol 2007;52:3859-79.

[14] K. Y. Aristovich, B. C. Packham, H. Koo, G. S. D. Santos, A. McEvoy, D. S. Holder. Imaging fast electrical activity in the brain with electrical impedance tomography. Neuroimage 2016;124:204-13.

[15] T. Tidswell, A. Gibson, R. Bayford, D. Holder. Three-Dimensional Electrical Impedance Tomography of Human Brain Activity. NeuroImage 2001;13:283-94.

[16] A. T. Tidswell, A. Gibson, R. H. Bayford, D. S. Holder. Electrical impedance tomography of human brain activity with a two-dimensional ring of scalp electrodes. Physiol Meas 2001;22:167-75.

[17] D. G. Nair. About being BOLD. Brain Res Rev 2005;50:229-43.

[18] E. M. Hillman. Coupling mechanism and significance of the BOLD signal: a status report. Annu Rev Neurosci 2014;37:161-81.

[19] B. B. Bartelle, A. Barandov, A. Jasanoff. Molecular fMRI. J Neurosci 2016;36:4139-48.

[20] J. Bodurka, P. A. Bandettini. Toward direct mapping of neuronal activity: MRI detection of ultraweak, transient magnetic field changes. Magn Reson Med 2002;47:1052-58.

[21] Q. Luo, H. Lu, H. Lu, D. Senseman, K. Worsley, Y. Yang, et al. Physiologically evoked neuronal current MRI in a bloodless turtle brain: detectable or not? Neuroimage 2009;47:1268-76.

[22] Q. Luo, X. Jiang, J.H. Gao. Detection of neuronal current MRI in human without BOLD contamination. Magn Reson Med 2011;66:492-7.

[23] N. Petridou, D. Plenz, A. C. Silva, M. Loew, J. Bodurka, P. A. Bandettini. Direct magnetic resonance detection of neuronal electrical activity. Proc Natl Acad Sci U S A 2006;103:16015-20.

[24] Y. Xue, X. Chen, T. Grabowski, J. Xiong. Direct MRI mapping of neuronal activity evoked by electrical stimulation of the median nerve at the right wrist. Magn Reson Med 2009;61:1073-82.

[25] B. J. Roth, A. Luterek, S. Puwal. The movement of a nerve in a magnetic field: application to MRI Lorentz effect imaging. Med Biol Eng Comput 2014;52(5):491-8.

[26] R. H. Kraus, P. Volegov, A. Matlachov, M. Espy. Toward direct neural current imaging by resonant mechanisms at ultra-low field. NeuroImage 2008;39:310-7.

[27] M. Joy, G. Scott, M. Henkelman.In vivo detection of applied electric currents by magnetic resonance imaging. Magn Reson Imaging 1989;7:89-94.

[28] A. K. Kasinadhuni, A. Indahlastari, M. Chauhan, M. Schär, T. H. Mareci, R. J. Sadleir. Imaging of current flow in the human head during transcranial electrical therapy. Brain Stimul 2017;10(4):764-772.

[29] E. Woo, J. Seo. Magnetic resonance electrical impedance tomography (MREIT) for high-resolution conductivity imaging. Physiol Meas 2008;29(10):R1-R26.

[30] C. Gabriel, A. Peyman, E. H. Grant. Electrical conductivity of tissue at frequencies below 1 MHz. Phys Med Biol 2009;54:4863-78.

[31] R. Sadleir, S. Grant, S. U. Zhang, B. Lee, H. Pyo, S. Oh, et al. Noise analysis in magnetic resonance electrical impedance tomography at 3 and 11 T field strengths. Physiol Meas 2005;26:875-84.

[32] A. M. H. Seelke, J. C. Dooley, L. A. Krubitzer. The emergence of somatotopic maps of the body in S1 in rats: the correspondence between functional and anatomical organization. PLoS One 2012;7(2):e32322.

[33] S. D. Keilholz, A. C. Silva, M. Raman, H. Merkle, A. P. Koretsky. Functional MRI of the rodent somatosensory pathway using multislice echo planar imaging. Magn Reson Med 2004;52:89-99.

[34] G. M. Shepherd. Nerve Cells and Nervous Systems: An Introduction to Neuroscience. Trends in Neurosciences 1992;15:33.

[35] P. E. Tibbetts. Principles of Neural Science. New York: The University of Chicago Press, 2013.

[36] S. Jacobson, E. M. Marcus, and S. Pugsley. Neuroanatomy for the neuroscientist. 2018.

[37] P. E. Tibbetts. Principles of Neural Science. The Quarterly Review of Biology 2013;88:139-40.

[38] A. Verkhratsky. A. Butt, Glial Neurobiology: A Textbook. UK: John Wiley & Sons, 2007.

[39] C. Watson, M. Kirkcaldie, G. Paxinos. The Brain: An Introduction to Functional Neuroanatomy. Elsevier Science Publishing Co Inc, 2010.

[40] D. Purves, G. Augusting, D. Fitzpatrick. Neuroscience. Sunderland (MA): Sinauer Associates, 2001.

[41] J. Malmivuo, R. Plonsey, Bioelectromagnetism: Principles and Applications of Bioelectric and Biomagnetic Fields. New York: Oxford University Press, 1995.

[42] A. Liston, R. Bayford, D. Holder. A cable theory based biophysical model of resistance change in crab peripheral nerve and human cerebral cortex during neuronal depolarisation: implications for electrical impedance tomography of fast neural activity in the brain. Med Biol Eng Comput 2012;50:425-37.

[43] D. S. Holder. Electrical Impedance Tomography. London: Institute of Physics, 2005.

[44] R. Pethig. Dielectric properties of body tissues. Clin Phys Physiol Meas 1987;8(A):5-12.

[45] C. Gabriel, S. Gabriel, E. Corthout. The dielectric properties of biological tissues: I. Literature survey. Phys Med Biol 1996;41:2231-49.

[46] S. Gabriel, R. W. Lau, C. Gabriel. The dielectric properties of biological tissues: II. Measurements in the frequency range 10 Hz to 20 GHz. Phys Med Biol 1996;41:2251-69.

[47] S. Gabriel, R. W. Lau, C. Gabriel.The dielectric properties of biological tissues: III. Parametric models for the dielectric spectrum of tissues. Phys Med Biol 1996;41:2271-93.

[48] D. Miklavcic, N. Pavselj, F. Hart. Electric Properties of Tissues. 2006.

[49] E. Degirmenci, B. M. Eyuboglu. Anisotropic conductivity imaging with MREIT using equipotential projection algorithm. Phys Med Biol 2007;52:7229-42.

[50] A. Indahlastari. Validation of Transcranial Electrical Stimulation (TES) Finite Element Modeling Against MREIT Current Density Imaging in Human Subjects. Arizona State University, Arizona, 2017.

[51] D. Holder. Electrical impedance tomography (EIT) of brain function. Brain Topogr 1992;5:87-93.

[52] N. P. Zhang. Electrical impedance tomography based on current density imaging. University of Toronto, Toronto, 1992.

[53] E. Woo, S. Y. Lee, and C. W. Mun. Impedance tomography using internal current density distribution measured by nuclear magnetic resonance. US: SPIE's 1994 International Symposium on Optics, Imaging and Instrumentation 1994; 2299.

[54] Y. Z. Ider, O. Birgul. Use of the magnetic field generated by the internal distribution of injected currents for Electrical Impedance Tomography (MR-EIT). Elektrik 1998;6:215-225.

[55] S. H. Oh, B. I. Lee, E. J. Woo, S. Y. Lee, M. H. Cho, O. Kwon, et al. Conductivity and current density image reconstruction using harmonic Bz algorithm in magnetic resonance electrical impedance tomography. Phys Med Biol 2003;48:3101-16.

[56] E. Woo, J. Seo. Magnetic resonance electrical impedance tomography (MREIT) for high-resolution conductivity imaging. Physiol Meas 2008;29:R1-26.

[57] H. J. Kim, T. I. Oh, Y. T. Kim, B. I. Lee, E. J. Woo, J. K. Seo, et al. In vivo electrical conductivity imaging of a canine brain using a 3T MREIT system. Physiol Meas 2008;29:1145-55.

[58] A. C. Scott, Neuroscience : A Mathematical Primer. United States: Springer, 2002.

[59] L. A. Geddes, L. E. Baker. The specific resistance of biological material--a compendium of data for the biomedical engineer and physiologist. Med Biol Eng 1967;5:271-93.

[60] C. J. Gauthier, C. Madjar, F. B. Tancredi, B. Stefanovic, R. D. Hoge. Elimination of visually evoked BOLD responses during carbogen inhalation: implications for calibrated MRI. Neuroimage 2011;54:1001-11.

[61] F. A. Nasrallah, L. Y. Yeow, B. Biswal, K. H. Chuang. Dependence of BOLD signal fluctuation on arterial blood CO2 and O2: Implication for resting-state functional connectivity. Neuroimage 2015;117:29-39.

[62] F. C. Moreton, K. A. Dani, C. Goutcher, K. O'Hare, K. W. Muir. Respiratory challenge MRI: Practical aspects. Neuroimage Clin 2016;11:667-677.

[63] J. F. Schenck. The role of magnetic susceptibility in magnetic resonance imaging: MRI magnetic compatibility of the first and second kinds. Med Phys 1996;23:815-50.

[64] S. Hecht, W. H. Adams, J. Narak, W. B. Thomas. Magnetic resonance imaging susceptibility artifacts due to metallic foreign bodies. Vet Radiol Ultrasound. 2011;52:409-14.

[65] K. Krupa, M. Bekiesinska-Figatowska. Artifacts in magnetic resonance imaging. Pol J Radiol 2015;80:93-106.

[66] H. Graf, G. Steidle, P. Martirosian, U. A. Lauer, F. Schick. Metal artifacts caused by gradient switching. Magn Reson Med 2005;54:231-4.

[67] O. Dietrich, M. F. Reiser, S. O. Schoenberg. Artifacts in 3-T MRI: Physical background and reduction strategies. Eur J Radiol. 2008;65:29-35.

[68] H. Graf, G. Steidle, F. Schick. Heating of metallic implants and instruments induced by gradient switching in a 1.5-Tesla whole-body unit. J Magn Reson Imaging. 2007;26:1328-33.

[69] E. Mattei, M. Triventi, G. Calcagnini, F. Censi, W. Kainz, G. Mendoza, et al. Complexity of MRI induced heating on metallic leads: Experimental measurements of 374 configurations. BioMed Eng Online 2008;7:1-16.

[70] D. Shrivastava, A. Abosch, T. Hanson, J. Tian, A. Gupte, P. A. Iaizzo, et al. Effect of the extracranial deep brain stimulation lead on radiofrequency heating at 9.4 Tesla (400.2 MHz). J Magn Reson Imaging 2010;32:600-7.

[71] D. Shrivastava, A. Abosch, J. Hughes, U. Goerke, L. DelaBarre, R. Visaria, et al. Heating induced near deep brain stimulation lead electrodes during magnetic resonance imaging with a 3 T transceive volume head coil. Phys Med Biol. 2012;57:5651-65.

[72] M. Ladd, H. Quick. Reduction of resonant RF heating in intravascular catheters using coaxial chokes. Magn Reson Med 2000;43:615-9.

[73] M. M. Elwassif, A. Datta, A. Rahman, M. Bikson. Temperature control at DBS electrodes using a heat sink: experimentally validated FEM model of DBS lead architecture. J Neural Eng 2012;9:046009.

[74] K. B. Baker, J. Tkach, J. D. Hall, J. A. Nyenhuis, F. G. Shellock, A. R. Rezai. Reduction of magnetic resonance imaging-related heating in deep brain stimulation leads using a lead management device. Neurosurgery 2005;57:392-7.

[75] P. Serano, L. M. Angelone, H. Katnani, E. Eskandar, G. Bonmassar. A Novel Brain Stimulation Technology Provides Compatibility with MRI. Scientific Reports 2015;5:9805.

[76] D. A. Finelli, A. R. Rezai, P. M. Ruggieri, J. A. Tkach, F. G. Shellock. MR Imaging-Related Heating of Deep Brain Stimulation Electrodes: In Vitro Study. AJNR Am J of Neuroradiol. 2002;23:1795-1802.

[77] A. R. Rezai, D. Finelli, J. A. Nyenhuis, G. Hrdlicka, J. Tkach, A. Sharan, et al. Neurostimulation systems for deep brain stimulation: in vitro evaluation of magnetic resonance imaging-related heating at 1.5 tesla. J Magn Reson Imaging 2002;15:241-50.

[78] J. H. Duyn. The future of ultra-high field MRI and fMRI for study of the human brain. Neuroimage 2012;62:1241-1248.

[79] H. van Genderingen, M. Sprenger, J. W. de Ridder, A. van Rossum. Carbon-fiber electrodes and leads for electrocardiography during MR imaging. Radiology 1989;171(3):872.

[80] J. F. Dunn, U. I. Tuor, J. Kmech, N. A. Young, A. K. Henderson, J. C. Jackson, et al. Functional Brain Mapping at 9.4T using a new MRI compatible electrode chronically implanted in rats. Magn Reson Med 2009;61:222-228.

[81] J. Van Audekerkea, R. Peeters, M. Verhoye, J. Sijbers, A. Van der Linden. Special designed RF-antenna with integrated non-invasive carbon electrodes for simultaneous magnetic resonance imaging and electroencephalography acquisition at 7T. Magn Reson Imaging 2000;18(7):887-91.

[82] M. Negishi, M. Abildgaard, I. Laufer, T. Nixon, R. T. Constable. An EEG (electroencephalogram) recording system with carbon wire electrodes for simultaneous EEG-fMRI (functional magnetic resonance imaging) recording. J Neurosci Methods 2008;173(1):99-107.

[83] Y. Guo, W. Duan, C. Ma, C. Jiang, Y. Xie, H. Hao, et al. Biocompatibility and magnetic resonance imaging characteristics of carbon nanotube yarn neural electrodes in a rat model. Biomed Eng Online. 2015, 14:118.

[84] C. Q. Jiang, H. W. Hao, L. M. Li. Artifact properties of carbon nanotube yarn electrode in magnetic resonance imaging. J. Neural Eng. 2013;10(2):026013.

[85] Medtronic. Lead kit for Deep Brain Stimulation: Implant Manual. Minnesota, 2010.

[86] S. Breit, J. B. Schulz, A. L. Benabid. Deep brain stimulation. Cell Tissue Res 2004;318:275-88.

[87] J. S. Perlmutter, J. W. Mink. Deep brain stimulation. Annu Rev Neurosci. 2006;29:229-57.

[88] C. C. McIntyre, P. J. Hahn. Network perspectives on the mechanisms of deep brain stimulation. Neurobiol Dis. 2010;38(3):329-37.

[89] C. Schmidt, U. van Rienen. Modeling the field distribution in deep brain stimulation: the influence of anisotropy of brain tissue. IEEE Trans Biomed Eng. 2012;59(6):1583-92.

[90] C. C. McIntyre, T. J. Foutz. Computational modeling of deep brain stimulation. Handb Clin Neurol. 2013;116:55-61.

[91] M. Chauhan, R. Vidya Shankar, N. Ashok Kumar, V. D. Kodibagkar, R.J. Sadleir. Multishot echo-planar MREIT for fast imaging of conductivity, current density, and electric field distributions. Magn Reson Med 2018;79:71-82.

[92] A. K. Kasinadhuni, A. Indahlastari, M. Chauhan, M. Schär, T. H. Mareci, and R. J. Sadleir. Imaging of current flow in the human head during transcranial electrical therapy. Brain Stimul 2017;10:764-72.

[93] G. J. Gage, D. R. Kipke, W. Shain. Whole animal perfusion fixation for rodents. J Vis Exp. 2012;65:3564.

[94] T.-I. Oh, C. Young, E. J. Woo, H. Yeon-Kyung, O. Suk-Hoon, L. Soo-Yeol. Improved Current Source Design to Measure Induced Magnetic Flux Density Distributions in MREIT. J Biomed Eng. 2006;27:30-7.

[95] C. Park, B. I. Lee, O. Kwon, E. J. Woo. Measurement of induced magnetic flux density using injection current nonlinear encoding (ICNE) in MREIT. Physiol Meas 2007;28:117-27.

[96] K. S. Nayak, D. G. Nishimura. Automatic field map generation and off-resonance correction for projection reconstruction imaging. Magn Reson Med 2000;43(1):151-4.

[97] C. H. Cunningham, J. M. Pauly, K. S. Nayak. Saturated double-angle method for rapid B1+ mapping. Magn Reson Med 2006; 55(6):1326-33.

[98] C. Park, O. I. Kwon. Current density imaging using directly measured harmonic Bz data in MREIT. Comput Math Methods Med. 2013;2013:381507.

[99] O. Kwon, H. Pyo, J. Seo, E. Woo. Mathematical framework for Bz-based MREIT model in electrical impedance imaging. Comput Math Appl 2006;51(5):817-28.

[100] H. S. Nam, C. Park, O. I. Kwon. Non-iterative conductivity reconstruction algorithm using projected current density in MREIT. Phys Med Biol. 2008(23);53:6947-61.

[101] H. J. Kim, S. Z. K. Sajib, J. C. Woo, M. N. Kim, O. I. Kwon, E. J. Woo. Analysis of local projected current density from one component of magnetic flux density in MREIT. Inv. Prob. 2013;29(7):1-17.

[102] C. O. Oluigbo, A. R. Rezai. Magnetic resonance imaging safety of deep brain stimulator devices. Handb Clin Neurol 2013;116:73-6.

[103] D. D. L. Chung. Carbon Fiber Composites. Massachusetts: Butterworth-Heinemann, 1994.

[104] J. F. Shackelford, W. Alexander, The CRC materials science and engineering handbook. Florida: CRC Press LLC, 2000.

[105] L. A. Geddes. Electrodes and the measurement of bioelectric events. New York: John Wiley and Sons, 1972.

[106] W. G. Ondo, C. Meilak, K. D. Vuong. Predictors of battery life for the Activa Soletra 7426 Neurostimulator. Parkinsonism Relat Disord 2007;13:240-2.

[107] M. Bin-Mahfoodh, C. Hamani, E. Sime, A. M. Lozano. Longevity of batteries in internal pulse generators used for deep brain stimulation. Stereotact Funct Neurosurg. 2003;80:56-60.

[108] A. M. Lozano, N. Lipsman, H. Bergman, P. Brown, S. Chabardes, J. W. Chang, et al. Deep brain stimulation: current challenges and future directions. Nat Rev Neurol 2019;15:148-60.

[109] S. D. Israeli-Korn, T. Fay-Karmon, S. Tessler, G. Yahalom, S. Benizri, H. Strauss, et al. Decreasing battery life in subthalamic deep brain stimulation for

Parkinson's disease with repeated replacements: Just a matter of energy delivered?. Brain Stimul 2019;12:845-50.

[110] O. Waln, J. Jimenez-Shahed. Rechargeable deep brain stimulation implantable pulse generators in movement disorders: patient satisfaction and conversion parameters. Neuromodulation 2014;17:425-30.

[111] L. Pycroft, J. Stein, T. Aziz. Deep brain stimulation: An overview of history, methods, and future developments. Brain Neurosci Adv 2018;2:2398212818816017.

[112] H. Graf, U. A. Lauer, A. Berger, F. Schick. RF artifacts caused by metallic implants or instruments which get more prominent at 3 T: an in vitro study. J Magn Reson Imaging. 2005;23:493-99.

[113] G. W. C. Kaye, T. H. Laby, N. P. Laboratory. Tables of physical and chemical constants. United States: John Wiley and Sons Inc., 2005.

[114] J. A. Nyenhuis, P. Sung-Min, R. Kamondetdacha, A. Amjad, F. G. Shellock, A. R. Rezai. MRI and implanted medical devices: basic interactions with an emphasis on heating. IEEE T DEVICE MAT RE 2005;5(3):467-80.

[115] A. Boutet, I. Hancu, U. Saha, A. Crawley, D. S. Xu, M. Ranjan, et al. 3-Tesla MRI of deep brain stimulation patients: safety assessment of coils and pulse sequences. J Neurosurg 2019;132(2):586-94.

[116] J. Kahan, A. Papadaki, M. White, L. Mancini, T. Yousry, L. Zrinzo, et al. The Safety of Using Body-Transmit MRI in Patients with Implanted Deep Brain Stimulation Devices. PLoS One 2015;10(6):e0129077.

[117] F. Sammartino, V. Krishna, T. Sankar, J. Fisico, S. K. Kalia, M. Hodaie, et al. 3-Tesla MRI in patients with fully implanted deep brain stimulation devices: a preliminary study in 10 patients. J Neurosurg 2017;127:892-98.

[118] N. Ashok Kumar. Anisotropy in diffusion and electrical conductivity distributions of TX-151 phantoms. Arizona State University, Arizona, 2015.

[119] R. A. Gibbs, G. M. Weinstock, M. L. Metzker, D. M. Muzny, E. J. Sodergren, S. Scherer, et al. Genome sequence of the Brown Norway rat yields insights into mammalian evolution. Nature 2004; 428:493-521.

[120] G. Paxinos, C. Watson. The rat brain in stereotaxic coordinates. Sydney: Academic Press, 1986.

[121] B. G. Sanganahalli, P. Herman, F. Hyder. Frequency-dependent tactile responses in rat brain measured by functional MRI. NMR Biomed 2008;21:410-16.

[122] D. Tracey. The Rat Nervous System. Burlington: Academic Press, 2004:797-815.

[123] L. Krubitzer, K. L. Campi, D. F. Cooke. All rodents are not the same: a modern synthesis of cortical organization. Brain Behav Evol 2011; 78:51-93.

[124] A. C. Silva, S. P. Lee, G. Yang, C. Iadecola, S. G. Kim. Simultaneous blood oxygenation level-dependent and cerebral blood flow functional magnetic resonance imaging during forepaw stimulation in the rat. J Cereb Blood Flow Metab 1999;19:871-79.

[125] S. Ogawa, T.-M. Lee, R. Stepnoski, W. Chen, X.-H. Zhu, K. Ugurbil. An approach to probe some neural systems interaction by functional MRI at neural time scale down to milliseconds. PNAS 2000;97(20):11026-11031.

[126] C. Spenger, A. Josephson, T. Klason, M. Hoehn, W. Schwindt, M. Ingvar*, et al.* Functional MRI at 4.7 tesla of the rat brain during electric stimulation of forepaw, hindpaw, or tail in single- and multislice experiments. *Exp Neurol 2000;* 166:246-253.

[127] X. Yang, F. Hyder, R. G. Shulman. Activation of single whisker barrel in rat brain localized by functional magnetic resonance imaging. Proc Natl Acad Sci U S A 1996;93:475-478.

[128] I. Kida, F. Xu, R. G. Shulman, F. Hyder. Mapping at glomerular resolution: fMRI of rat olfactory bulb. Magn Reson Med 2002; 48:570-76.

[129] T. Kim, K. Masamoto, M. Fukuda, A. Vazquez, S. G. Kim. Frequency-dependent neural activity, CBF, and BOLD fMRI to somatosensory stimuli in isoflurane-anesthetized rats. Neuroimage 2010;52,:224-33.

[130] S. Boussida, A. S. Traoré, F. Durif. Mapping of the brain hemodynamic responses to sensorimotor stimulation in a rodent model: A BOLD fMRI study. *PLoS One 2017;* 12(4):e0176512.

[131] K. Masamoto, T. Kim, M. Fukuda, P. Wang, S. G. Kim. Relationship between neural, vascular, and BOLD signals in isoflurane-anesthetized rat somatosensory cortex. Cereb Cortex 2007;17:942-950.

[132] T. Bliss. The hippocampus book. New York: Oxford University Press, 2007.

[133] D. R. Merrill, M. Bikson, J. G. Jefferys. Electrical stimulation of excitable tissue: design of efficacious and safe protocols. J Neurosci Methods 2005;141:171-98.

[134] C. B. Canto, F. G. Wouterlood, and M. P. Witter. What does the anatomical organization of the entorhinal cortex tell us?. Neural Plast 2008; 2008:381243.

[135] J. J. Knierim. The hippocampus. Curr Biol 2015;25:R1116-1121.

[136] G. Buzsáki, C. A. Anastassiou, C. Koch. The origin of extracellular fields and currents--EEG, ECoG, LFP and spikes. Nat Rev Neurosci 2012; 13: 407-420.

[137] S. D. Stoney, Jr., W. D. Thompson, H. Asanuma. Excitation of pyramidal tract cells by intracortical microstimulation: effective extent of stimulating current. J Neurophysiol 1968;31:659-69.

[138] E. J. Tehovnik. Electrical stimulation of neural tissue to evoke behavioral responses. J Neurosci Methods 1996;65:1-17.

[139] R. J. Sadleir, S. C. Grant, E. J. Woo. Can high-field MREIT be used to directly detect neural activity? Theoretical considerations. Neuroimage 2010;52:205-16.

[140] S. D. Keilholz, A. C. Silva, H. Merkle, A. P. Koretsky. Functional MRI of the rodent somatosensory pathway using multislice echo planar imaging. Magn Reson Med 2004; 52:89-99.

[141] S. D. Keilholz, A. C. Silva, M. Raman, H. Merkle, A. P. Koretsky. BOLD and CBV-weighted functional magnetic resonance imaging of the rat somatosensory system. Magn Reson Med 2006; 55(2):316-24.

[142] A. Eklund, T. E. Nichols, H. Knutsson. Cluster failure: Why fMRI inferences for spatial extent have inflated false-positive rates. Proc Natl Acad Sci U S A 2016;113:7900-5.

APPENDIX A

ASCEPTIC SURGICAL PROCEDURE FOR THE BILATERAL IMPLANTATION OF CARBON ELECTRODES IN RODENT HIPPOCAMPUS

Pre-surgical Steps

1. Anesthetize the rat through intraperitoneal injection of ketamine-xylazine cocktail.
2. Perform foot-pinch test to assess anesthetic depth.
3. Apply eye lubricant and shave head to prepare surgical area.
4. Apply chlorhexidine using gauze (non-sterile) on shaved region.
5. Place rat on stereotax with heat warmer and towels. Secure ear bars into the ear canal and teeth on bite bar. Ensure ear bars measure equal length on both sides.
6. Sterilize shaved region of the head by alternating the application of chlorhexidine and ethanol using a gauze with three linear strokes.
7. Cover sterilized portion with Press'n Seal Wrap. Using a scissor, cut a hole (small) in the wrap.

Intra-operative Steps

Phase 1: Preparation

1. Using the scalpel (#15 blade), make a midline incision over the calvarium. Ensure the scalpel is flat and cut in a single stroke. Let the incision extend from between the eyes to end of the skull. Use scissor for all other manipulations.
2. Keep the incision open by pinching off skin and wrap using towel clamps.
3. Push connective tissue away from the incision using cotton swabs. Use scissors and forceps if necessary. Apply sufficient pressure to stimulate cranial nerves and

initiate vasoconstriction. Bleeding (minor) is expected. Apply pressure using a gauze.

Phase 2: Skull-flat position

1. Visually locate skull landmarks (Bregma and Lambda).
2. Using the pen marker, mark Bregma.
3. Mount stereotactic arm with 18G needle at 0^{o} (to vertical) on the DV drive.
4. Position the tip of needle just above Bregma using AP, DV and ML drives.
5. Navigate posteriorly to Lambda. Using the pen marker, mark Lambda.
6. Using DV drive, lower tip of the needle to slightly depress the skull at Bregma. Record the coordinates of Bregma (DV). Navigate to Lambda and record DV coordinate of Lambda (DV).
7. Re-position the bite bar to minimize DV distance between Bregma and Lambda. Repeat step 6 until the distance is <0.3 mm.
8. Once skull-flat is confirmed, record other coordinates of Bregma and Lambda (AP, ML).

Phase 3: Determine entry points on skull

1. Calculate the anteroposterior distance between bregma (B) and lambda (L). Using the distance between both landmarks, determine coordinates superior to the target on skull surface (with respect to L). Mark these coordinates as entry points on the skull.

2. Incline stereotaxic arm 50^{o} to the dorsoventral axis. Record these inclined coordinates to determine distance traversed in steps described below.

Phase 4: Drill and Implant cannulas

1. Using a 16G needle make a small groove over both entry points to anchor the tip of the drill bit.
2. Tilt the rat head down by 20^{o} and stereotaxic arm by 30^{o}.
3. Introduce few drops of water before and during drilling the right entry point to cool the surface. Drill at medium-high speed through 2 mm. Record dorsoventral coordinate at the end of the drilling.
4. Similarly, drill a hole on the left side.
5. Tap each hole (~3 threads) through the guide to create threads to secure the cannula.
6. Introduce cannula holder with a cannula through the same guide. Screw each cannula (~3 threads) using the cannula holder. Carefully unscrew the assembly holding the cannula in place by a forcep. Repeat for other side.

Phase 5: Implant electrodes

1. Using weigh boats, mix the desired consistency of dental cement. Make head cap (avoid muscle) leaving 3-4 threads to screw in the cap of cannulas.
2. Measure and cut carbon electrodes of length matching distance of hippocampal target from skull surface.

3. Introduce carbon electrodes through cannulas until the insulated length is just at the top.
4. Check if the cement is strong enough to hold cannulas in place. Then, screw in the dummy cannula. Suture skin behind head cap.

APPENDIX B

PREPARING RODENTS FOR fMREIT/fMRI IMAGING EXPERIMENTS

Preparation of Animals for Use in Imaging Experiments

I. Prepare procedure room for animal knock down and animal preparation

a. Knockdown:

i. Turn on heat warmer (warm) at the procedure table

ii. Connect waste gases at the procedure table

iii. Turn on 3-5% isoflurane with 1.5% air in chamber

iv. Transfer animal to chamber

v. When animal response is absent for foot-pinch test, transfer to bed on procedure table

1. Switch isoflurane + air to nose cone

2. Stop isoflurane to chamber

vi. Apply ophthalmic ointment over eyes

b. Animal preparation:

i. Lower isoflurane to 1-2% and deliver through nose cone

ii. Check animal's breathing (i.e. deep abdominal breathing is optimal)

iii. Shave target area for 'ground' electrode

iv. Using saline(sterile)-dipped cotton tip applicators, clean the recently shaved area

v. Unscrew dummy caps using plier

vi. Clean surrounding areas with saline(sterile)-dipped cotton tip applicators

vii. Replace new sterile-carbon (1C) electrodes, if needed

viii. Once electrodes are in place, screw on wired-caps

ix. Place sterile-needle electrodes for forepaw stimulation subcutaneously in the lower surface of the paw between the second and fourth digits

1. Ensure no direct contact between electrode tips
2. Check impedance between both fore-paw electrodes (~500 kΩ)

x. Apply electrode gel over surface 'ground' electrode for improved contact

xi. Slide surface electrode over shaved region under the neck

xii. Check impedance between both MREIT 1C-ground pairs (~500 kΩ)

c. Animal ready for transport

II. Prepare to transport animal from procedure room to magnet room

a. Survey magnet room to check whether connections are in-place and ready for animal transport

i. Turn on isoflurane and air supply to magnet room

1. 3-4% isoflurane and 1.5% air

III. Transporting animal to the magnet:

a. Increase the isoflurane in procedure room to 3-4% isoflurane and 1.5% air.

b. Move the animal to magnet

ii. Place animal on the mounted rat bed

iii. Place teeth into the bite bar and secure the nose with nose cone

iv. Check pinch test response

v. Slowly lower anesthesia to 2.5 – 3% isoflurane + air

vi. Place forelimbs on either side of the body (fingers pointing to feet)

vii. Place respiration probe under the animal

viii. Check respiration rate (~40 – 60 breaths per minute)

c. Place ear bars

d. Check response to pinch test. If response absent, continue with next steps

e. Ensure all screws are in-place and tight

f. Secure animal to bed through tape (use gauze between tape and animal)

IV. Slowly advance bed to position in the center of magnet (ensure no obstruction in anesthesia pipes)

V. Run imaging experiments

a. Check respiration monitor. Adjust anesthesia to bring respiratory rate within 50-60 breaths per minute. Look for normal respiration pattern.

b. If >80 breaths per minute, then increase isoflurane.

c. If <50 breaths per minute, then decrease isoflurane.

d. In general, maintain same level of isoflurane during functional experiments.

VI. After imaging, prepare to transfer the animal back to procedure room

a. Increase isoflurane and bring animal to 40-60 breaths per minute

b. Once respiration has settled, gently pull the bed out

c. Remove ear bars and tape securing animal to bed

d. Check animal response to pinch test. If responds, increase isoflurane by 0.5% - 1% and wait for ~1 minute. Otherwise, survey procedure room:

    i. Ensure 2-3% isoflurane + 1.5% air; ensure supply to bed

    ii. Check waste gases connection

    iii. Check bed temperature

e. Check animal response to pinch test. If no response, transport animal to procedure room (hold behind limbs and support neck with a finger from underneath)

f. Place nose into nose cone

g. Check animal's response to pinch test. If no response, then slowly reduce isoflurane to 1-2%.

h. Replace wired-caps with dummy caps

i. Remove ground and fore-paw needle electrodes

j. After waking, transfer rat to cage

APPENDIX C

FABRICATION AND CHARACTERIZATION OF CARBON ELECTRODES

Procedures for the Fabrication and Testing of Carbon Electrodes

1. One-contact (1C) and Two-contact (2C) Carbon Electrodes

Carbon electrodes were constructed by dip-coating carbon bundles in insulative solutions. The exact composition of insulative solutions are summarized in Table C1.1. Schematics showing the fabrication and electrical characterization of carbon electrodes are shown in Figures C1.1 and Figure C1.2.

Electrode preparation	**Chemicals**	**Concentration**		**Purpose**
		Diameter = 250 μm	**Diameter = 500 μm**	
Stage I	Nafion and Isopropanol	50% V/V	50% V/V	Mechanical strength (stiffness)
Stage II	PVDF in Acetone	12% W/V	15% W/V	First round of plastic insulation
Stage III	PVDF in Acetone	15% W/V	18% W/V	Second round of plastic insulation

Table C1.1: Stages and composition of insulative solutions used in preparation of one-contact (1C) carbon electrodes.

1.1 Fabrication of 1C Carbon Electrodes

Step 1. Twist damp carbon fiber bundles and fix onto a holder. Coat these carbon bundles with insulative solutions in three stages, described below.

Step 2. Stage I: Dip-coat carbon bundles with three insulative coats of Nafion (CAS: 31175-20-9, Sigma Aldrich) and Isopropanol (70% in H_2O, CAS: 67-63-0, Sigma Aldrich). After every coat, heat the Nafion-coated bundles for approximately 30 seconds using a heat gun. Allow drying periods of several minutes between coats, and subsequently dry the carbon bundles for approximately 6 hours.

Step 3. Visually inspect electrodes under an optical microscope for deformities such as insulation breaks and stray fibers. Ensure stray fibers (especially loops) are cut with a pair of micro-tip scissors.

Step 4. Stage II: Immerse carbon bundles in low-viscosity solutions of Polyvinylidene Fluoride (Kynar PVDF, Arkema) in Acetone. Dip each electrode in 15% PVDF and allow to dry for ~5 minutes. Perform multiple dips to ensure good insulation throughout each electrode. Let electrodes rest for 8 hours.

Step 5. Stage III: The rigid-and-smooth carbon electrodes may finally be coated with a relatively high-viscosity PVDF solution (such as 18% PVDF) to ensure complete plastic insulation around the carbon fibers. Finally, dry the newly-formed 1C carbon electrodes for about 6 hours.

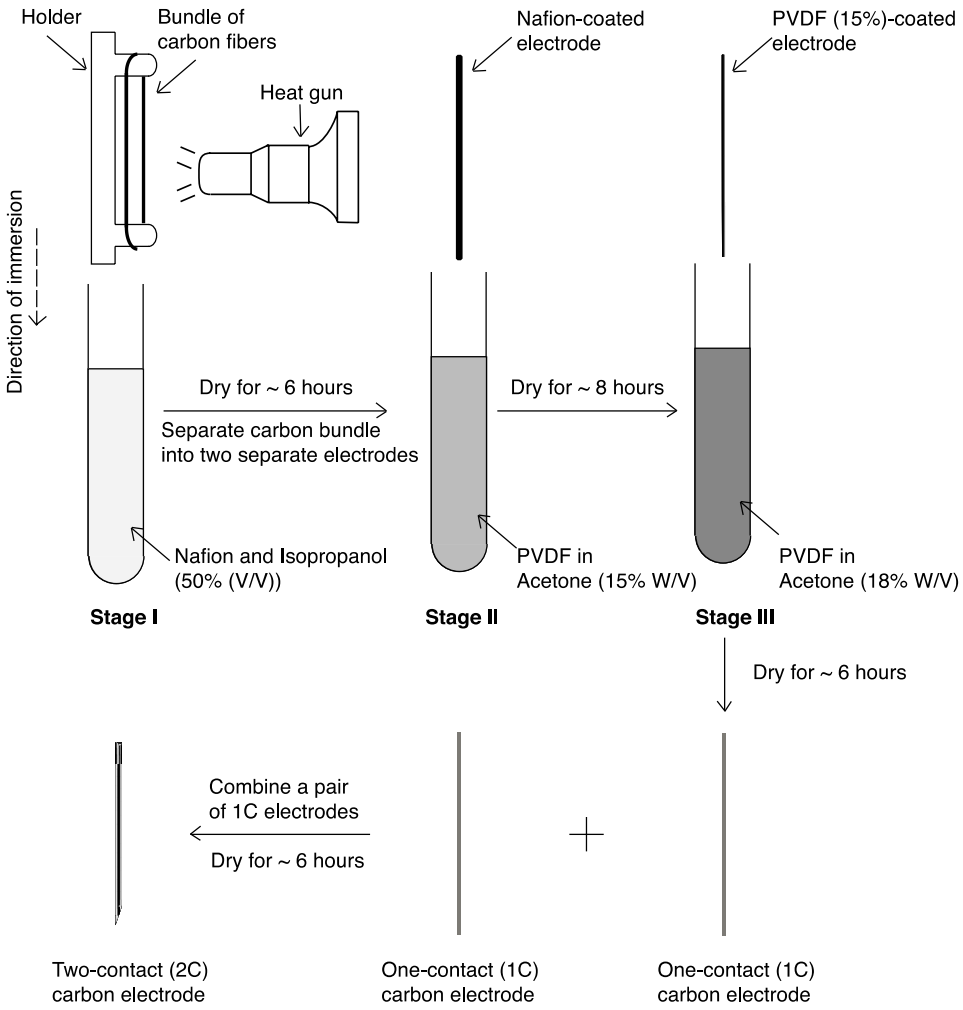

Figure C1.1: Fabrication process for one- and two-contact (1C, 2C) carbon electrodes. The concentration of Polyvinylidene Fluoride (PVDF) solutions was suitable for 500-μm diameter one-contact (1C) and 1000 x 500 μm^2-cross-sectional area two-contact (2C) carbon electrodes.

1.2 Fabrication of 2C Carbon Electrodes

Step 1. Choose a pair of 1C electrodes as prepared in Section C1.1. Verify the insulative quality of each carbon electrode as described in Section C1.3.

Step 2. Secure the pair of 1C carbon electrodes by co-immersion in a solution of PVDF in Acetone (20% W/V). Allow the newly-formed 2C carbon electrodes to dry for about 6 hours.

1.3 Electrical characterization of 1C carbon electrodes

Carbon (1C, 2C) and platinum-iridium (DBS 3389 lead) electrodes were characterized using a two-terminal test as shown in Figure C1.2. The two-terminal test measured electrical impedance between the test carbon, DBS or platinum-iridium electrode and a reference copper electrode immersed in saline solution.

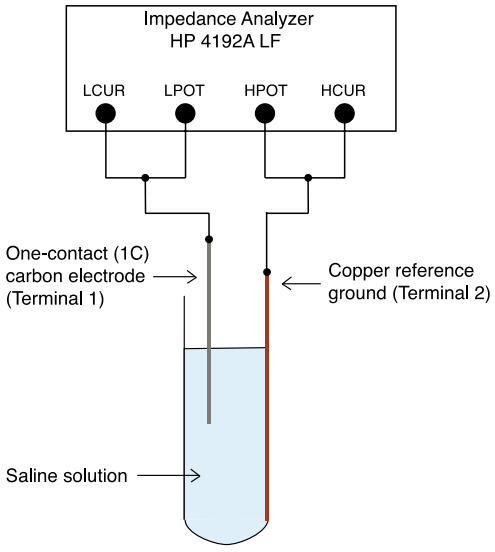

Figure C1.2: Two-terminal test configuration used for electrical characterization of carbon and platinum-iridium (Pt-Ir) electrodes in 17% saline solution. One-contact (1C), two-contact (2C) carbon and platinum-iridium (DBS 3389 lead) electrodes were tested with electrode connected to LCUR and LPOT terminals of

HP4192A Impedance Analyzer and copper reference connected to HPOT and HCUR terminals.

2. RF-induced heating in size-matched carbon and platinum-iridium (Pt-Ir) electrodes

Two-contact (2C) carbon and platinum-iridium (DBS 3389 lead) electrodes were placed in a bench-top RF energy deposition system for the measurement of RF-heating related temperature changes. Each electrode type was secured to a fiber optic temperature sensor with gallium-arsenide (TS3, Optocon, Germany) tips. An agar gel phantom was prepared by combining 20 g Agar, 3 g NaCl, 0.5 g $CuSO_4$ and 1000 ml distilled water into a uniform consistency. The solution was heated in a microwave until bubbles rose towards the top layer of the solution. After cooling the solution to room-temperature, the carbon and Pt-Ir electrode-sensor ensembles were deployed until the tips coincided with the mid-plane of the cylindrical phantom. A third temperature sensor ('Central') was placed in the center of the phantom to measure native temperature changes in the agar gel phantom without the presence of electrodes. Temperature measurements from all three sensors were relayed to a temperature signal conditioner (FOTEMP-OEM-PLUS, Optocon, Germany). Temperature values were recorded for every two seconds over a 30-minute period.

The gel phantom implanted with electrodes and temperature sensors, as described above, was placed within a copper-coated RF-shield tube. Sinusoidal RF signals

(amplitude = 0.13 mW, frequency = 298 MHz) were amplified using a RF power amplifier (gain = 30 dBm). The two-element RF surface coil was driven continuously by the amplified RF sinusoidal signals and deposited RF energy into the phantom. The maximum power (amplitude = 10 mW) was deposited in the center of the phantom, which is coincident with the third temperature sensor ("Central"). Temperature measurements from each sensor were adjusted for their initial readings.

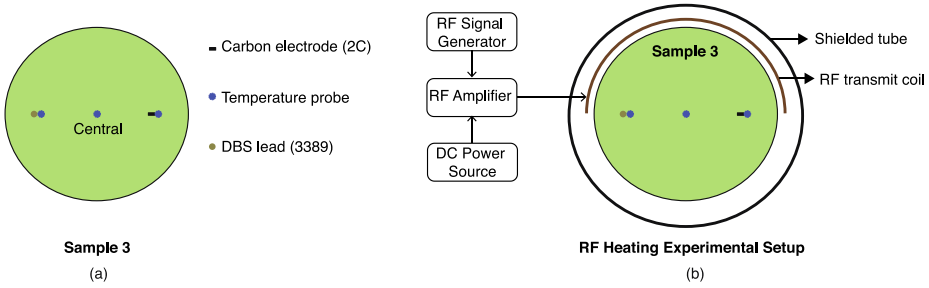

Figure C1.3: Bench-top RF energy deposition system designed for monitoring local temperature changes near carbon (2C) and platinum-iridium (Pt-Ir) electrodes in agar gel phantom. Two-contact (2C) carbon and platinum-iridium (DBS 3389 lead) electrodes were placed in an agar gel phantom (1 S/m). Each electrode was secured to a temperature sensor to record temperatures nearby. A centrally placed temperature sensor ("Central") recorded temperature changes away from electrodes. An RF amplifier was used to continuously drive an RF surface coil placed above the phantom. The MRI bore was simulated with a copper tube (dia. 15 cm).

APPENDIX D

ARIZONA STATE UNIVERSITY INSTITUTIONAL ANIMAL CARE AND USE COMMITTEE (IACUC) APPROVAL FOR RODENT USE IN FUNCTIONAL IMAGING EXPERIMENTS

IACUC Approval for the Appropriate Use of Animals

Institutional Animal Care and Use Committee (IACUC)
Office of Research Integrity and Assurance
Arizona State University
660 South Mill Avenue, Suite 312
Tempe, Arizona 85287-6111
Phone: (480) 965-6788 *FAX:* (480) 965-7772

Animal Protocol Review

ASU Protocol Number:	**19-1728R**
Protocol Title:	**Direct Functional Imaging of Electrical Brain Stimulation**
Principal Investigator:	**Rosalind Sadleir**
Date of Action:	**8/19/2019**

The animal protocol review was considered by the Committee and the following decisions were made:

If you have not already done so, documentation of Level III Training (i.e., procedure-specific training) will need to be provided to the IACUC office before participants can perform procedures independently. For more information on Level III requirements see https://researchintegrity.asu.edu/animals/training.

Total # of Animals:	**85**	
Species:	**Rats**	**Unalleviated Pain/Distress: No-60**
Species:	**Salamander**	**Unalleviated Pain/Distress: No-25**

Protocol Approval Period: **8/19/2019 – 8/18/2022**

Sponsor:	**N/A**
ASU Proposal/Award #:	**N/A**
Title:	**N/A**

Signature: _____ for C. Shalley Date: 8/20/2019
IACUC Chair or ***Designee***

Cc: IACUC Office
IACUC Chair